THE SPIRO-HELICAL ANTENNA

by
Idine Ghoreishian

Thesis submitted to the faculty of the Virginia
Polytechnic Institute and State
University in partial fulfillment of the requirements for
the degree of
MASTER OF SCIENCE
In
Electrical Engineering

Approved by:
Ahmad Safaai-Jazi, Chair
Gary S. Brown
William Davis

August, 1999
Blacksburg, Virginia Tech
Keywords:Helical, Antenna, Spiral, Novel Design

The Spiro-Helical Antenna

By
Idine Ghoreishian
Ahmad Safaai-Jazi, chairman
Electrical and Computer Engineering

(ABSTRACT)

A novel antenna made of a spiral wire wrapped into a larger helical shape is introduced. The geometry of this antenna, which is a doubly helical structure, is fully described by five independent parameters, including two radial dimensions, two pitch angles, and the number of turns. Radiation properties of this antenna are examined both theoretically and experimentally. The Numerical Electromagnetic Code (NEC-2) is used to obtain simulation results. A large number of cases with different radii, pitch angles, and number of turns are investigated. Results for far-field patterns, gain, axial ratio, and bandwidth are presented. The influence of parameters on radiation properties are examined. Several prototypes of the antenna were constructed and tested using an outdoor antenna range. Measured far-field patterns are presented over a wide range of frequencies. The measured and computed radiation patterns are in good agreement.

The results of this study indicate that the proposed antenna provides circular polarization and high gain over a wide frequency range. For example, when the number of turns is 10, a gain of 11-14 dB, a boresight axial ratio of less than 3 dB, and a half-power beamwidth of about 40 degrees are achieved over a 30% bandwidth. The side-lobe level for most cases examined is better than 10 dB below the main beam. A unique advantage of this antenna is its much smaller size compared with a conventional helical antenna made of straight wire shaped into a helix. Having about the same radiation characteristics, including gain, circular polarization, bandwidth, and side-lobe level, this new antenna occupies a volume more than 2.5 to 3 times smaller than the conventional helix. This reduction in size, which in turn may imply smaller weight and lower packaging and manufacturing costs, makes the proposed antenna very appealing to many communications and aerospace applications.

Acknowledgements

I would like to express my sincerest thanks and gratitude to Dr. Ahmad Safaai-Jazi for being my mentor on this journey. His guidance, patience, and support throughout this time has been a blessing. I would also like to thank the members of my committee, Dr. Gary S. Brown, and Dr. William A. Davis for all their help.

A special thanks to Randall Nealy and Mike Barts during the measurement campaign. Also, thanks to Eric Holmberg and Jeremy Harker for their helpful suggestions during the coding period of this work.

I could not have done this without the ever continuing support of my family and friends. This work is dedicated to all my family and friends, both here and abroad, as a reminder of my years here at Virginia Tech.

Table of Contents

List of Figures

List of Tables

1. Introduction

Antenna designers are always searching for ways to improve existing designs or introduce novel designs in order to achieve desirable radiation characteristics, reduce the size and weight, and thus make antennas more cost efficient. Axial ratio, gain, and bandwidth are some of the important properties which they concentrate on improving. The antenna structure and size is another issue of considerable interest. Smaller size and weight may be a mandatory requirement for antennas used in spacecraft, aircraft, and satellite communication systems.

In this thesis, attention is focused on helical antennas which find important applications in communication systems, primarily because of their circular polarization and wide bandwidth. The helical antenna, first introduced by Kraus in 1946, [1], has been subject of extensive investigations during the past five decades. Many modifications to the basic helix geometry have been proposed with the aim of improving the gain, bandwidth, axial ratio, and VSWR [2]-[6]. More recently, the possibility of size reduction, while maintaining the radiation characteristics, has been explored [7]. In this thesis, a novel antenna with a doubly helical geometry is introduced, which provides wide bandwidth and circular polarization but occupies a volume 2.5 to 3 times smaller than a conventional helix having about the same radiation characteristics. This antenna, referred to as *Spiro-Helical Antenna* is made of a primary helix wound on a cylinder of larger diameter. An important advantage of this antenna is that it can be conveniently constructed.

The spiro-helical antenna is analyzed both theoretically and experimentally. Radiation properties, including far-field patterns, gain, axial ratio, and input impedance, are computed over wide frequency ranges. All theoretical studies of spiro-helical antenna are carried out using NEC-2 (Numerical Electromagnetic Code, Version 2.0) software, which is a numerical code based on the method of moments. The spiro-helical antenna can be fully described by five parameters. The influence of these parameters on radiation properties are examined in order to find their optimum values. Experimental evaluation of a few prototype spiro-helical antennas are also presented. Far-field patterns and axial ratio were measured using the outdoor antenna range in the Virginia Tech Antenna Laboratory. Computed and measured results are in good agreement.

The simulation and measurement results indicate that the spiro-helical antenna indeed provides high gain and circular polarization over a wide bandwidth. A gain-bandwidth ratio (upper to lower frequency) of about 40% and an axial ratio-bandwidth of about 33% can be achieved. Gain values of 11 to 14 dB are obtained when the number of turns is 10.

Chapter 2 presents a brief literature review of the conventional helix and some modifications that have been developed in the past few decades. The geometry of the spiro-helical antenna is discussed in Chapter 3. The parametric equations describing the geometry are derived in this chapter. These equations are used in Chapter 4 to carry out a comprehensive numerical analysis of the spiro-helical antenna using the NEC-2 software. Simulation results and a comparison to the conventional helix are presented in this chapter. This comparison demonstrates similar radiation characteristics for the smaller volume size of spiro-helical antennas. Chapter 5 discusses the fabrication and measurements of spiro-helical antennas. Comparisons are also made to the theoretical results found in Chapter 4. Chapter 6 summarizes the findings of this research work and points out further developments of the spiro-helical antenna. Finally, the appendices contain the computer code used to generate the input data files for NEC as well as numerical and experimental results for an additional case not presented in Chapter 4 and Chapter 5.

2. Conventional Helical Antennas

In this thesis attention is focused on helical antennas which find important applications in communication systems, primarily because of their wide bandwidth and circular polarization. In satellite communication systems, propagation of radio waves through the ionosphere suffers Faraday rotation at some frequencies; thus circularly polarized waves would be desirable in order to maintain reliable data and information signal transmission. The wide bandwidth of helical antennas lies in the fact that they are of the traveling-wave type, while their circular polarization property may be attributed to their effective loop-dipole geometry.

Since the inception of helical antennas by Kraus in 1946 [1], extensive studies have been made by many researchers around the world with the aim of more accurately predicting the radiation characteristics, improving the properties such as gain, axial ratio, and bandwidth, reducing the size, and optimizing the designs for desired applications. A brief survey of these studies is presented in this chapter. Analytical solutions of helical antennas, except for certain simple cases, are difficult to obtain. As a result, researchers have largely employed experimental and numerical techniques to analyze helices. In the remaining sections of this chapter, radiation characteristics of the conventional cylindrical helix are reviewed. This review proves particularly useful in comparing the properties of a proposed novel helical antenna with those of the conventional helix. Then, several modifications to the cylindrical helix, proposed by researchers during the past few decades, are addressed.

2.1 Radiation Characteristics of a Cylindrical Helix

A conventional helix is formed by winding a wire on a cylindrical surface while maintaining a constant spacing between the turns. The geometry of a helix, shown in Figure 2.1, can be described using the following parameters:

D = diameter of helix
C = circumference of helix = πD
S = spacing between turns (center to center)
α = pitch angle = $\tan^{-1}$ (S/πD)
L_0 = length of 1 turn = $\sqrt{C^2 + S^2}$
n = number of turns
L = axial length = nS
a = radius of helix wire conductor

Electromagnetic properties of a helix may be studied in two different modes of operation, known as the transmission mode and the radiation mode. The transmission mode corresponds to the propagation of an electromagnetic wave through an infinite helix. This can be viewed as a helix being a transmission line or waveguide [1]. The radiation mode, on the other hand, corresponds to the function of a helix as an antenna. Many different radiation modes are possible, but the focus is mainly on two specific kinds; namely normal mode and axial mode. In a normal-mode helix, radiation is maximum perpendicular to its axis, while the axial-mode helix provides a main beam along the axis. The axial mode can exist over a wide range of frequencies and is also circularly polarized. Because of its broad bandwidth and circular polarization, the axial-mode helix is a widely used antenna. Figure 2.2 describes these two modes graphically.

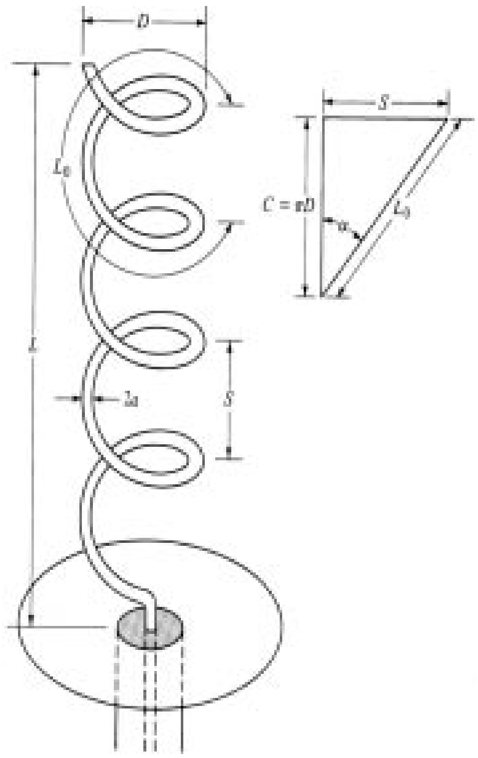

Figure 2.1 Geometry of a conventional helix [8].

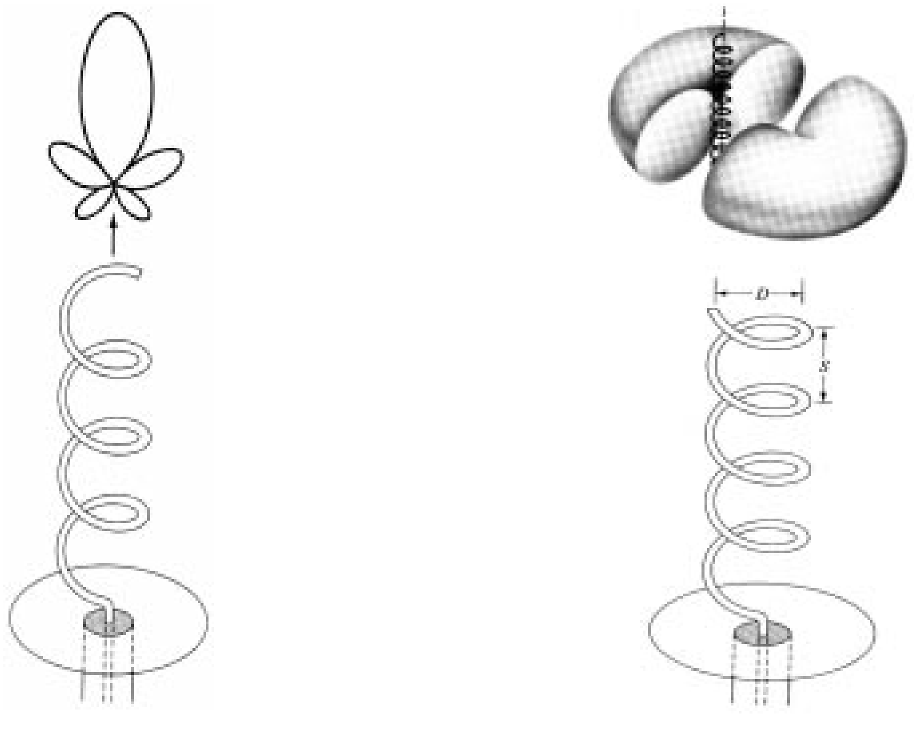

(a)

(b)

Figure 2.2 Radiation pattern for (a) axial-mode helix ,(b) normal-mode helix [8].

2.1.1 Normal-Mode Cylindrical Helix

In this mode of operation, the radiated field is maximum in directions normal to the helix axis. This mode is supported if the length of the helix is small compared to the wavelength of operation [9]. The radiation fields of a normal-mode helix may be approximated as the sum of the fields for a short dipole and a small loop [10]. In this model, each loop has a diameter equal to that of the helix, D, while each short dipole has a length equal to the spacing between the turns, S. For an ideal short dipole, the far field in a spherical coordinate system (r, θ, ϕ) is expressed as

$$E_\theta = \frac{jA_o e^{-jkr}}{r}\left(\frac{S}{\lambda}\right)\sin\theta, \qquad (2.1)$$

where A_o is a constant, $k = \frac{2\pi}{\lambda}$ is the propagation constant, and λ denotes the wavelength. For a small loop, the electric field in the far-field region is written as

$$E_\phi = \frac{A_o e^{-jkr}}{2r}\left(\frac{\pi D}{\lambda}\right)^2 \sin\theta\ . \qquad (2.2)$$

It is clear that E_θ and E_ϕ are 90° out of phase. But since $|E_\phi| \neq |E_\theta|$, in general the far-field of a normal-mode helix is elliptically polarized. However, a normal-mode helix, may be designed to provide circular polarization. A measure of how close to circular polarization the radiated field of an antenna may be, is described by the axial ratio (AR). This ratio for the normal-mode helix may be defined as

$$\mathrm{AR} = \frac{|E_\theta|}{|E_\phi|} \qquad (2.3a)$$

$$= \frac{2S\lambda}{\pi^2 D^2}\ . \qquad (2.3b)$$

A more general definition of axial ratio is the ratio of the major axis over the minor axis of the polarization ellipse [11]. It is evident from (2.3a) that the helix is circularly polarized when the axial ratio is unity. Hence, from (2.3b), the condition for circular polarization in a normal-mode helix is obtained as

$$\pi D = \sqrt{2S\lambda}\ . \tag{2.4}$$

The normal-mode helix is a narrow bandwidth antenna suitable for low capacity applications. The radiation pattern of this antenna is described by F(θ) = sin (θ) which is the same as that of a short dipole.

2.1.2 Axial-Mode Cylindrical Helix

The axial mode of operation occurs when the circumference of helix is on the order of one wavelength. Analyzing the current distribution on each turn of an axial-mode helix shows that the phase changes by 180° over one-half turn. Furthermore, the current direction is reversed over half a turn by the geometry; that is, another 180° phase shift. Thus, the current at opposite points on each turn will be in phase. This leads to constructive interference of waves radiated along the axis of the helix from opposite points, hence the characteristic directive beam along the axis for the axial-mode helix.

A helix operating in this mode is a traveling-wave antenna and is regarded as a wideband antenna. Antennas whose radiation properties do not change significantly over a bandwidth ratio of upper to lower frequency about 2 are classified as wideband. It has been shown that the axial-mode is sustained over a range given by [9]

$$\frac{3}{4}\lambda < C < \frac{4}{3}\lambda\ . \tag{2.5}$$

With these limits, a bandwidth ratio of $\frac{f_u}{f_l} = \frac{16}{9} = 1.78$ is obtained.

A unique property of the axial-mode helix is circular polarization of radiation along its axis. This is because the phase of the current changes by 90° over a quarter turn, which in turn leads to the orthogonal far-field components also differing in phase by 90°. The sense of circular polarization is dependent on the sense of the winding of the helix. When wound in the right-hand sense, a right-hand polarization exists, while winding in the left-hand sense results in a left-hand polarization [12]. Figure 2.3 illustrates the difference between these two windings.

An approximate analysis of the axial-mode helix may be performed using the endfire array concept. Assuming that the helix is an array of n equally-spaced and uniformly-excited elements, with a single turn representing the element, the array factor, AF, is obtained as

$$AF(\theta) = A_o \frac{\sin\left(\frac{n\psi}{2}\right)}{n\sin\left(\frac{\psi}{2}\right)}, \qquad (2.6)$$

where $\psi = \beta s \cos\theta + \alpha_o$, A_o is a constant, and α_o is the inter-element phase shift.

To find the total far-field pattern, the array factor is multiplied by the element pattern. Since the axial-mode helix behaves like a Hansen-Woodyard endfire array and accounting for a phase shift of 2π due to traveling of current wave along one turn, $\alpha_o = -\beta s - 2\pi - \frac{\pi}{n}$ is considered. The pattern of a circular loop element can be approximated as cos θ [9], thus the total pattern is expressed as

$$F(\theta) = A_o \cos\theta \frac{\sin\left(\frac{n\psi}{2}\right)}{n\sin\left(\frac{\psi}{2}\right)}. \qquad (2.7)$$

2.1.3 Optimum Parameters

The effects of the helix parameters on radiation characteristics such as gain, input impedance, axial ratio, and bandwidth have been studied extensively. A brief discussion of optimum parameters is presented below.

Figure 2.4 shows the effect of circumference on gain. It is noted that at different pitch angles, peak gain can be achieved when the circumference is about 1.135λ [10]. Figure 2.5 shows the influence of pitch angle on gain at different frequencies. Clearly, a pitch angle of 12.5° provides the maximum gain [10].

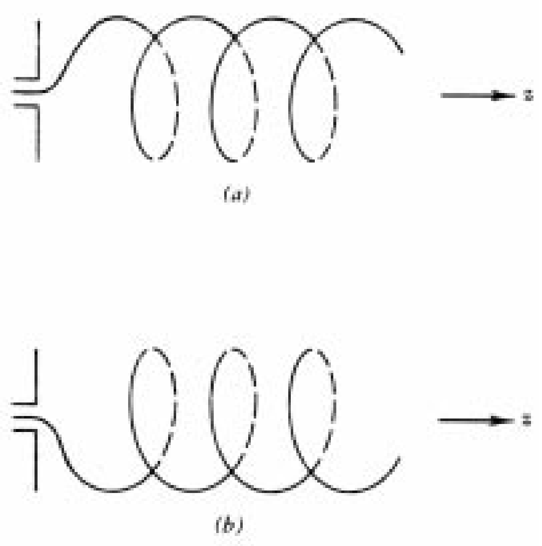

Figure 2.3 (a) Right hand sense, (b) left hand sense [1].

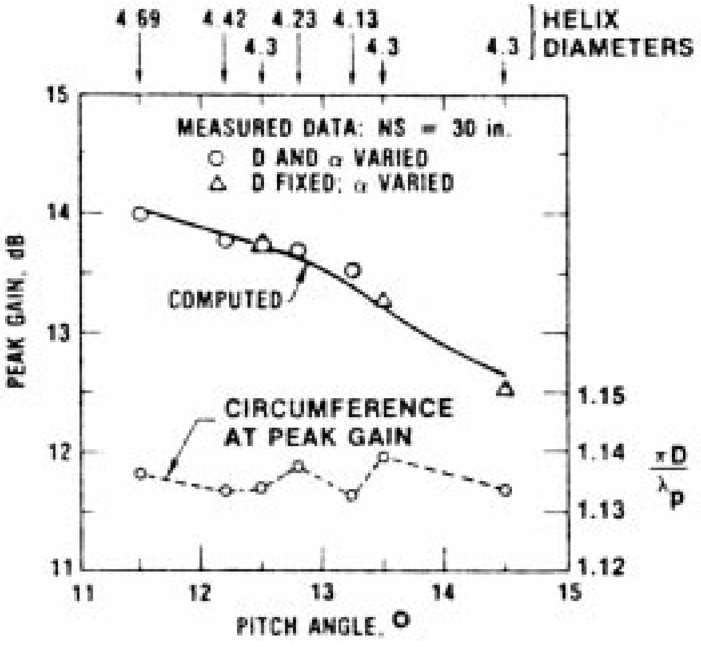

Figure 2.4 Peak computed gain (solid) and circumference at peak gain (dashed) [10].

Figure 2.6 illustrates variations of gain versus number of turns. It is observed that peak gain increases with number of turns. This is in accordance with the behavior of an equally spaced array whose directivity increases with the number of elements.

While circumference, pitch angle, and number of turns significantly affect the gain and bandwidth, other aspects of the helical antenna structure cause little change in the radiation properties. Two of these are the diameter of the conductor and the ground plane. Experimental studies have shown that ground planes with dimensions (radius for circular and side for square ground planes) larger than $\frac{\lambda}{2}$ has little effect on radiation properties [4]. The conductor size has negligible effect on the radiation pattern, but has a noticeable influence on the input impedance.

2.1.4 Empirical Results

For axial-mode helical antennas satisfying the conditions $12° < \alpha < 15°$, $n > 3$, and $\frac{3}{4} < C_\lambda < \frac{4}{3}$, Kraus has developed empirical formulae for gain, input impedance, axial ratio, and half power beamwidth [1]. The empirical gain formula is given as

$$G = 15 C_\lambda^2 n S_\lambda \ , \qquad (2.8)$$

where $C_\lambda = \frac{C}{\lambda}$ and $S_\lambda = \frac{S}{\lambda}$ are normalized circumference and spacing between turns, respectively. Using a larger experimental database, King and Wong [5] developed a more accurate expression for the gain given as

$$G = 8.3 \left(\frac{\pi D}{\lambda_p} \right)^{\sqrt{n+2}-1} \left(\frac{nS}{\lambda_p} \right)^{0.8} \left[\frac{\tan 12.5°}{\tan \alpha} \right]^{\frac{\sqrt{n}}{2}}, \qquad (2.9)$$

where λ_p is wavelength at peak gain.

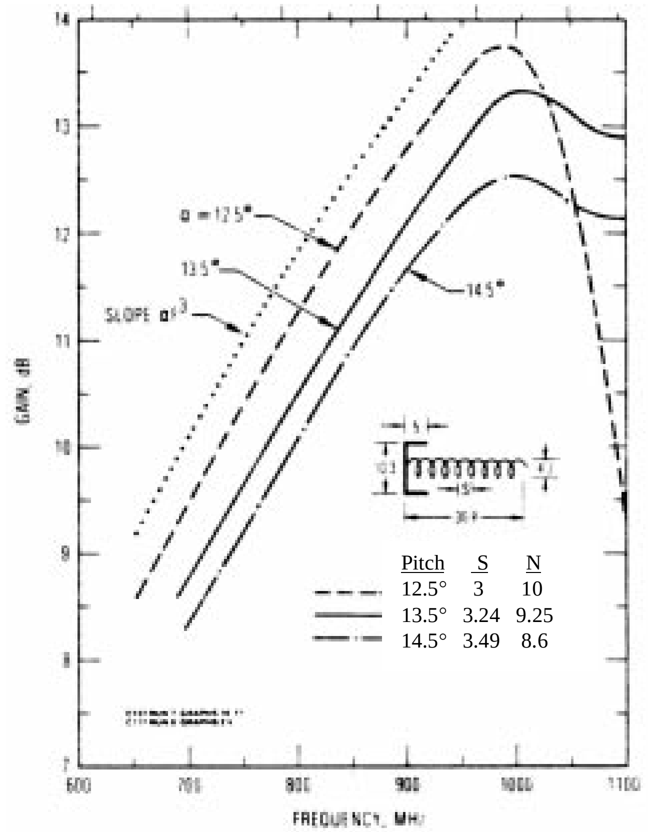

Figure 2.5 Measured gain for pitch angles of 12.5°, 13.5°, and 14.5° [10].

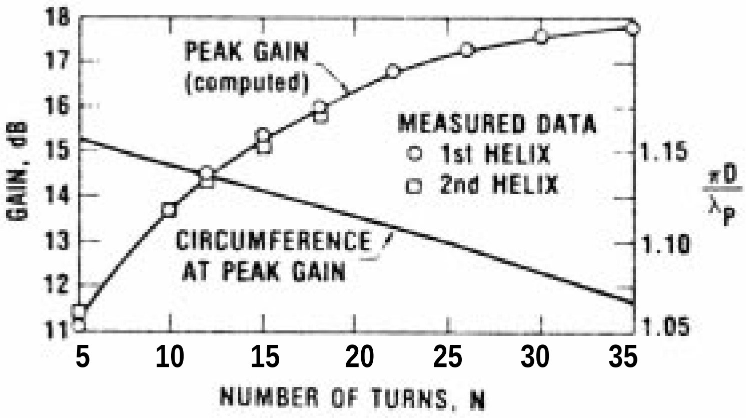

Figure 2.6 Peak gain and circumference at peak gain versus number of turns [10].

For the half-power beamwidth, an earlier empirical expression by Kraus and, a few decades later, a more accurate formula by King and Wong were developed. The results are

$$HPBW = \frac{52}{C_\lambda \sqrt{nS_\lambda}} \text{ degrees} \qquad (2.10)$$

by Kraus and

$$HPBW = \frac{K_B \left(\frac{2n}{n+5} \right)^{0.6}}{\left(\frac{\pi D}{\lambda} \right)^{\frac{\sqrt{n}}{4}} \left(\frac{nS}{\lambda} \right)^{0.7}} \left(\frac{\tan\alpha}{\tan 12.5^\circ} \right)^{\frac{\sqrt{n}}{4}} \text{ degrees} \qquad (2.11)$$

by Wong and King [6].

The input impedance of an axial-mode helix is largely resistive and insensitive to frequency changes over the bandwidth of the antenna. A nearly pure resistive input impedance is attributed to the traveling-wave nature of the axial-mode helix [13]. Kraus's empirical formula for input impedance is

$$R = 140 \frac{C}{\lambda} \ \Omega\,. \qquad (2.12)$$

Examining the axial ratio, it has been found that the finite helix does not provide perfect circular polarization. The deviation from circular polarization is described in terms of an axial ratio defined as the ratio of the major axis over the minor axis of the polarization ellipse. The axial ratio for perfect circular polarization is 1, while for linear polarization it is infinity. The equation for the axial ratio developed by Kraus is [1]

$$AR = \frac{2n+1}{2n} \quad . \tag{2.13}$$

It is noted that the axial ratio approaches unity as the number of turns is increased.

The bandwidth, as a frequency ratio, for the conventional helix is defined as

$$\frac{f_u}{f_l} \approx (2.93)^{\frac{4}{3\sqrt{n}}}, \tag{2.14}$$

where f_u and f_l are the upper and lower frequencies, respectively, at which the gain is 3 dB below the peak gain.[8]

2.2 Modifications to Cylindrical Helix

Many modifications have been made to the original helical antenna proposed by Kraus in order to improve its radiation characteristics. These modifications have varied from geometric manipulations to changes in ground plane and feed.

Reflectors are referred to as the metal sections at the base of a single helix. A helix is backed by a reflector in order to improve gain and reduce back radiation [14]. Reflectors of various shapes, including planar, cylindrical, and conical, have been used. A helix with a conical reflector is referred to as the “helicone”.

The end of the helix can also be tapered in order to improve Voltage Standing Wave Ratio (VSWR), bandwidth, and axial ratio. The taper angle can be made the same as the pitch angle. Studies have shown that tapering leads to a more gradual helix-to-free-space transition and a reduction of reflected energy [15]. In addition to tapered ends, tapered feeds are also helpful in lowering axial ratio as well as VSWR.

By using two different pitch angles within a single winding, a double-pitch helix is capable of improving gain, axial ratio and bandwidth. Two helices with different pitch angles are combined, end to end , to form a double-pitch helix. Helices designed with specific gain-frequency characteristics in mind utilize this design [12].

2.3 Spherical Helical Antenna

A novel helical geometry, referred to as spherical helix, was recently investigated at Virginia Tech [16]-[18]. Through numerical investigation and experimentation, it was found that the spherical helix produces radiation characteristics which are considerably different than those of the conventional helix.

A unique property of the spherical helix is circular polarization over a very broad beamwidth. This property makes the spherical helix attractive for some communications systems with low channel capacity, such as global positioning systems. The small volume of the spherical helix, when compared to the conventional helix, is another advantage which can be very useful in situations where size and weight limitations need to be strictly observed.

2.4 Conical Helical Antenna

There are certain similarities between the conventional helix and the conical helical antenna. It has been shown [8] that the conical helical antenna is able to provide unidirectional radiation (single lobe) toward the apex of the cone with the maximum occurring along the axis. A constant impedance and circular polarization are maintained over a large bandwidth, much like the conventional helix.

A unique feature of the conical helical antenna is the control of bandwidth. If the conical helix is mounted on a ground plane, a reduction in bandwidth will occur.[19] By varying the cone angle θ_0 and the wrap angle δ, the beamwidth can also be controlled.

2.5 Stub-Loaded Helix

The stub-loaded helix is a new design which was also recently developed at Virginia Tech [7]. The winding used for this antenna includes periodically placed loading stubs on the circumference of each turn. Each loading stub is directed along a radial path from the center axis to the helical winding. The stubs allow the helix to be electrically longer than the physical circumference. This design is expected to provide radiation properties comparable to an equivalent conventional helix, because the radiation from the stubs are is minimal.

The stub-loaded helix (SLH) design produces a maximum gain when the pitch angle is about 8°. When compared to a conventional axial-mode helix with a pitch angle of 11° to 15°, the shallower pitch angle of the SLH results in a shortening of the antenna length by approximately one-half for the same number of turns. However, unlike the conventional helix, the SLH exhibits a complex input impedance which varies with frequency [7].

Accounting for the reduction in the radius and height of the SLH, the volume is one-fourth of an equivalent conventional helix. The measured gain of both the 10-turn conventional helix and the 10-turn SLH are approximately 1 to 1.5 dB below the computed results from NEC-4. The axial ratio measurements of the SLH are in agreement with the computed data. Using a common polarization bandwidth of a 3 dB axial ratio or lower, the SLH exhibits an operating bandwidth which exceeds 20% of the center frequency [7].

3. Spiro-Helical Antenna

3.1 Introduction

In this chapter, a novel antenna made of a helix wound around a cylindrical surface is introduced. This antenna, as illustrated in Figure 3.1, is a doubly helical structure and is referred to as *Spiro-Helical Antenna.* The primary helix has a radius a' and pitch angle α'. Once wrapped around a cylindrical surface of radius a, the axis of the primary helix is transformed from a straight line into a helical curve of radius $a + a'$ and pitch angle α. It is now clear that a spiro-helical antenna can be fully described by five parameters—two radii(a and a'), two pitch angles (α and α'), and the number of larger turns (N) on the cylinder of radius a. The spiro-helical antenna is fed by means of a coaxial cable, with the inner conductor of the cable connected to the helix and the outer conductor becoming the ground plane; see Figure 3.1.

The idea of the spiro-helical antenna was conceived to reduce the size of the conventional helical antenna, while maintaining the useful radiation characteristics such as circular polarization and wide bandwidth. The conjecture that this geometry

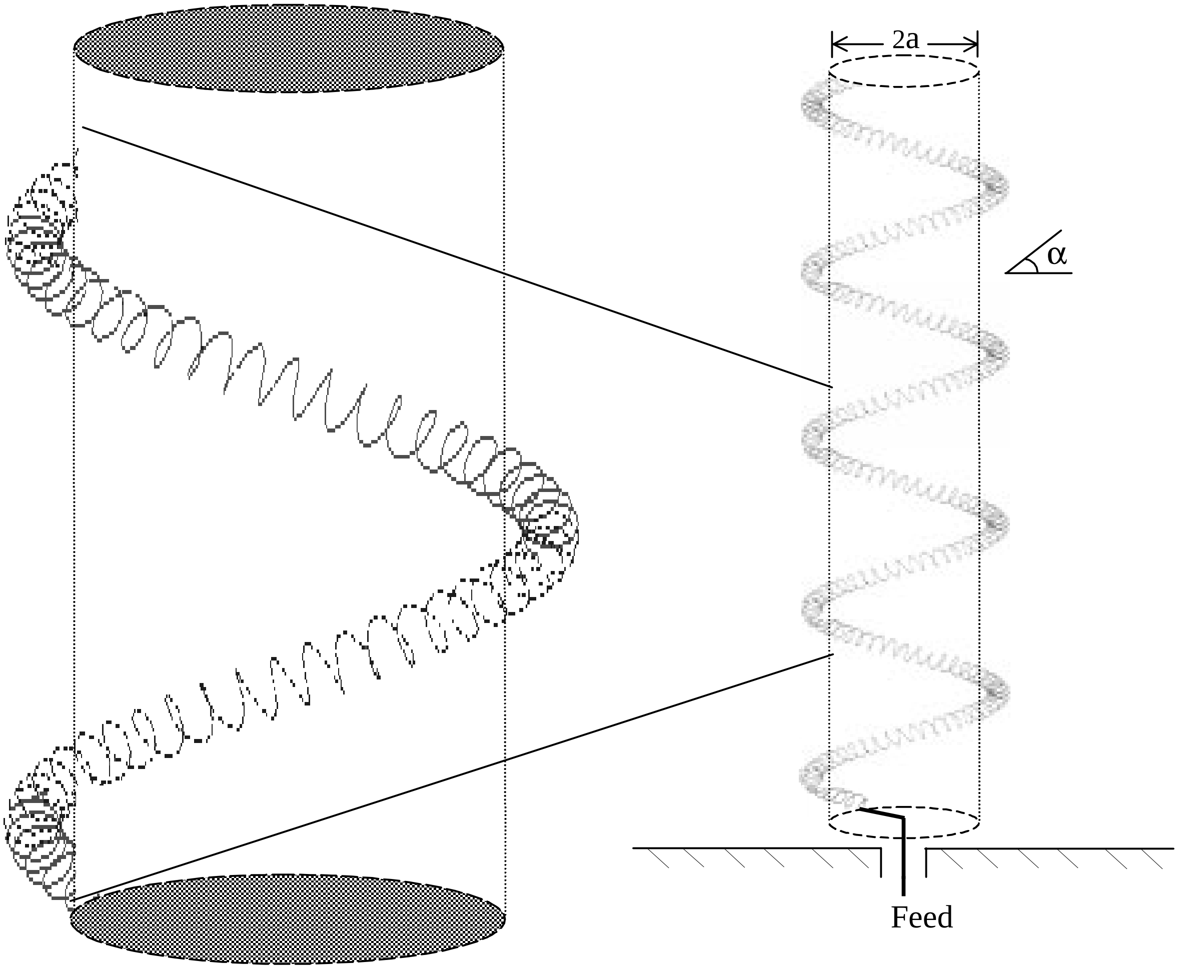

Figure 3.1 Spiro-helical antenna over a ground plane fed by a coaxial cable

might result in size reduction originated from the fact that helical structures, such as those used in microwave tube amplifiers, exhibit slow wave properties. However, a slower propagation velocity corresponds to a smaller wavelength as implied from the relationship $\lambda=\upsilon/f$, where f is the frequency. Thus, intuitively, a helical antenna made of a spiral instead of a straight wire would allow smaller physical dimensions. An important purpose of the research work presented in this thesis was to verify this conjecture by examining radiation properties of the proposed doubly helical structure and comparing them with those of a conventional helix. Following the initial validation of expected properties of the spiro-helical antenna, a comprehensive investigation of the radiation characteristics was performed using both experimental and theoretical analyses. The remaining sections of this chapter describe the derivation of parametric equations of spiro-helical antenna.

3.2 Parametric Equations of the Spiro-Helical Antenna

In order to facilitate the numerical analysis of the spiro-helical antenna, a set of equations describing its geometry are needed. With the availability of these equations, the coordinates of an arbitrary point on the spiro-helical structure are readily determined in terms of the parameters a, a', α, α', and an axial dimension z_A. Before embarking upon the derivation of equations for the spiro-helical geometry, we first examine the parametric equations for a simple cylindrical helix, such as the primary helix with radius a' and pitch angle α' shown in Figure 3.2a. Furthermore, we use two sets of coordinates; namely the primed Cartesian coordinates (x', y', z') and cylindrical coordinates $(\rho' = a', \varphi', z')$ for the geometry of the primary helix, and the unprimed coordinates (x, y, z) and (ρ, φ, z) for describing the geometry of the doubly helical structure.

The parametric equations of the primary helix are expressed as

$$x' = a' \cos\varphi' \tag{3.1a}$$

$$y' = a' \sin\varphi' \tag{3.1b}$$

$$z' = (a' \tan\alpha') \cdot \varphi'. \tag{3.1c}$$

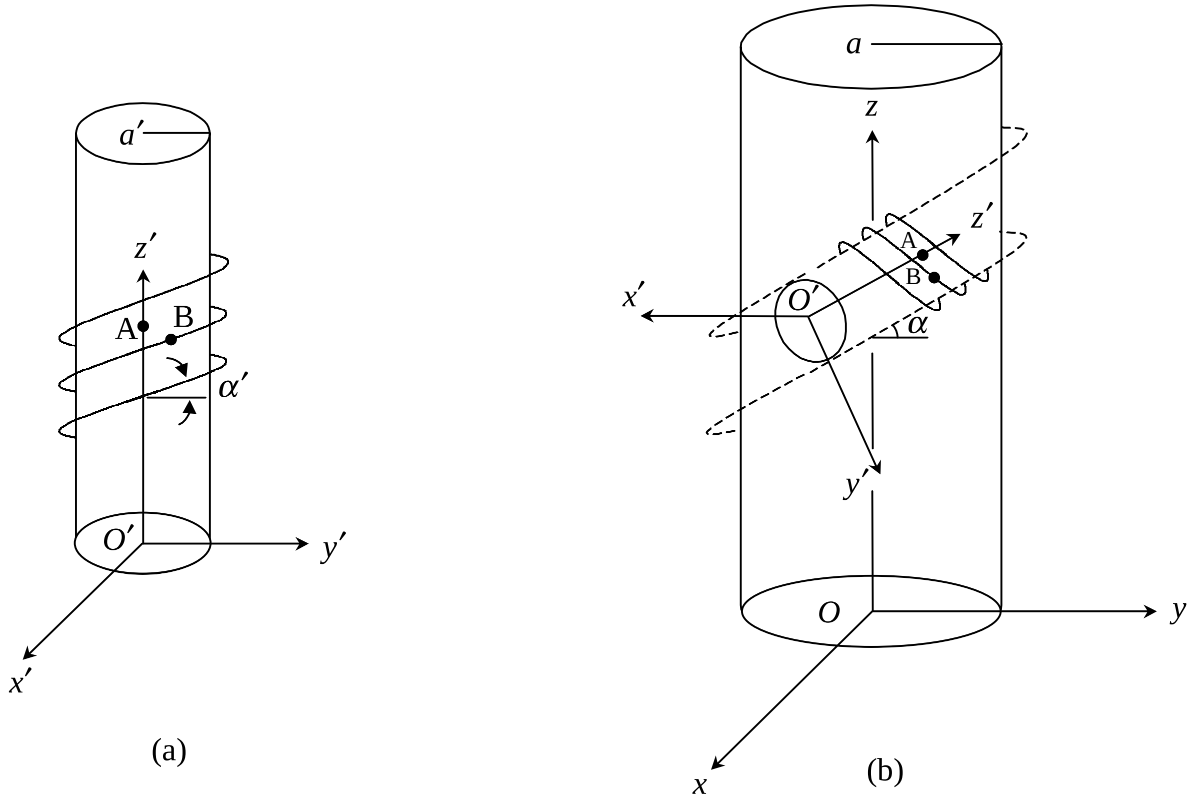

(a)

(b)

Figure 3.2 Geometry and coordinates for the derivation of parametric equations of the spiro-helical antenna. (a) primary helix, (b) spiro-helical geometry

Once the primary helix is wound on a cylinder of radius a with a pitch angle α as in Figure 3.2b, the z'-axis assumes a helical shape of radius $(a+a')$. The parametric equations of the helically-shaped z'-axis, in analogy with (3.1), are expressed as

$$x = (a + a')\cos\varphi \tag{3.2a}$$

$$y = (a + a')\sin\varphi \tag{3.2b}$$

$$z = [(a + a')\tan\alpha]\cdot\varphi. \tag{3.2c}$$

Next, let us consider an arbitrary point A on the z'-axis in both primary helix (Figure 3.2a) and the spiro-helical geometry (Figure 3.2b). The coordinates of this point are $x' = 0, y' = 0,$ and $z' = z_A$ and in the spiro-helical geometry are denoted as x_A, y_A, z_A. The coordinates x_A, y_A, and z_A are related to each other through (3.2). z'_A can be determined in terms of z_A using the integral expression for length. That is,

$$\begin{aligned} z'_A &= \int_{z=0}^{z_A} \left[(dx)^2 + (dy)^2 + (dz)^2\right]^{\frac{1}{2}} \\ &= \int_0^{z_A} \left[\left(\frac{dx}{dz}\right)^2 + \left(\frac{dy}{dz}\right)^2 + 1\right]^{\frac{1}{2}} dz\ . \end{aligned} \tag{3.3}$$

Using chain-rule differentiation,

$$\frac{dx}{dz} = \frac{dx}{d\varphi}\frac{d\varphi}{dz} = -\frac{(a+a')\sin\varphi}{(a+a')\tan\alpha} = -\frac{\sin\varphi}{\tan\alpha}$$

$$\frac{dy}{dz} = \frac{dy}{d\varphi}\frac{d\varphi}{dz} = \frac{(a+a')\cos\varphi}{(a+a')\tan\alpha} = \frac{\cos\varphi}{\tan\alpha}$$

and substituting in (3.3), yields

$$z'_A = \int_0^{z_A} \left[\frac{1}{\tan^2\alpha} + 1\right]^{\frac{1}{2}} dz$$

or

$$z'_A = \frac{z_A}{\sin\alpha}. \tag{3.4}$$

Now, consider a point B on the primary helix such that $z'_B = z'_A$. The other coordinates of B; namely, x'_B and y'_B are related to z'_B through equations (3.1). We assume that the relations among primed coordinates remain locally valid after z'-axis is transformed into a helix. This assumption is valid if the shape of a single turn in the primary helix and in the spiro-helical structure remains essentially the same. Then, introducing vectors $\overrightarrow{AB}, \overrightarrow{OA},$ and $\overrightarrow{OB}$, we have

$$\overrightarrow{AB} = x'_B \hat{x}' + y'_B \hat{y}' \tag{3.5}$$

$$\overrightarrow{OA} = x_A \hat{x} + y_A \hat{y} + z_A \hat{z} \tag{3.6}$$

$$\overrightarrow{OB} = x_B \hat{x} + y_B \hat{y} + z_B \hat{z} \; . \tag{3.7}$$

However,

$$\overrightarrow{OB} = \overrightarrow{OA} + \overrightarrow{AB} \tag{3.8}$$

and it can be shown, by inspection, that (without loss of generality it is assumed that the local x'-axis is perpendicular to the z-axis),

$$\hat{x}' = \cos\varphi \, \hat{x} + \sin\varphi \, \hat{y} \tag{3.9a}$$

$$\hat{y}' = -\cos\alpha \, \hat{z} - \sin\alpha \sin\varphi \, \hat{x} + \sin\alpha \cos\varphi \, \hat{y} \tag{3.9b}$$

$$\hat{z}' = \sin\alpha \, \hat{z} - \cos\alpha \sin\varphi \, \hat{x} + \cos\alpha \cos\varphi \, \hat{y}. \tag{3.9c}$$

Combining (3.5) through (3.9c), yields

$$\begin{aligned} \overrightarrow{OB} &= x_B \hat{x} + y_B \hat{y} + z_B \hat{z} \\ &= \left(x_A + x'_B \cos\varphi - y'_B \sin\alpha \sin\varphi\right)\hat{x} + \\ &\quad \left(y_A + x'_B \sin\varphi + y'_B \sin\alpha \cos\varphi\right)\hat{y} + \\ &\quad \left(z_A - y'_B \cos\alpha\right)\hat{z}. \end{aligned} \tag{3.10}$$

Equating the like components in (3.10), substituting for x_A, y_A, and z_A with the right-hand side expressions in (3.2), and replacing x'_B and y'_B with the right-hand side expressions in (3.1), we finally obtain

$$x = x_B = (a + a')\cos\varphi + a'\cos\varphi\cos\varphi' - a'\sin\varphi\sin\varphi'\sin\alpha \tag{3.11a}$$

$$y = y_B = (a + a')\sin\varphi + a'\sin\varphi\cos\varphi' + a'\cos\varphi\sin\varphi'\sin\alpha \tag{3.11b}$$

$$z = z_B = [(a + a')\tan\alpha]\cdot\varphi - a'\sin\varphi'\cos\alpha \tag{3.11c}$$

where, from (3.2c)

$$\varphi = \frac{z_A}{(a + a')\tan\alpha} \tag{3.12}$$

and from (3.4) and (3.1c)

$$\varphi' = \frac{z_A}{a'\tan\alpha'\sin\alpha} \tag{3.13}$$

z_A varies in the range $0 \le z_A \le z_{A_{\max}}$, where $z_{A\ \max}$ is the height of the spiro-helical antenna. It is related to the number of turns N (turns with the mean radius $a+a'$) according to the following relationship.

$$z_{A_{\max}} = 2\pi N(a + a')\tan\alpha \tag{3.14}$$

Equations (3.11) to (3.14) fully describe the geometry of spiro-helical antennas. These equations are used to generate coordinates of discrete points on the antenna which are then used as part of the input data to the NEC-2 software. The spiro-helical antenna shown in Figure 3.1 has been obtained using (3.11) to (3.14).

4. Numerical Analysis of the Spiro-Helical Antenna

4.1 Introduction

The complex geometry of the spiro-helical antenna defies simple analytical solutions for its radiation properties. Thus, the theoretical analysis of this antenna is carried out using numerical methods. In this work, the method of moments code NEC-2 is used to evaluate radiation characteristics, including far-field patterns, polarization, gain, half-power beamwidth, and input impedance. By varying several parameters, a large amount of simulation results are obtained. These results indicate how each parameter influences the radiation characteristics of spiro-helical antennas. The wire geometry applicable to the NEC-2 software is explained here. The Matlab® code used to create the data files is given in Appendix A.

The unique geometry of the spiro-helical antenna presents a wide selection of variables which can be adjusted for each simulation. These include pitch angles, radii, and number of turns for both large- and small-diameter helices. The frequency is varied over the range 1.4 GHz to 3.5 GHz. This is the actual frequency range used in measurements of several prototype spiro-helical antennas. In the majority of the simulations, the diameters of the larger helix and the spiral were not changed as frequently as the other parameters. Table 4.1 summarizes the range of variables used in numerical evaluation of radiation characteristics of spiro-helical antennas.

Table 4.1 Range of Variables for the Investigation of Spiro-helical Antenna

Parameter	Value Range
Number of turns, N	$3 \leq N \leq 15$
Frequency, f	1.4 GHz $\leq f \leq$ 3.5 GHz
Helix pitch angle, α	$7° \leq \alpha \leq 16°$
Spiral pitch angle,α'	$5° \leq \alpha' \leq 80°$
Helix radius, a	11 mm $\leq a \leq$ 21 mm
Spiral radius, a'	1.5 mm $\leq a' \leq$ 3 mm
Conductor radius, r_o	0.2 mm $\leq r_o \leq$ 0.5 mm

Section 4.2 will further discuss the software NEC-2 and presents the results for a typical conventional helix. This example, for which the results are also available in the literature presented in chapter 2, ensures the correct use of NEC-2. Section 4.3 will discuss one representative set of the simulations in detail which will later be used to construct prototype models for the experimental analysis of spiro-helical antenna. Finally, section 4.4 will present a comparison with a conventional helix of similar size.

4.2 NEC-2

The Numerical Electromagnetic Code (version 2.0) or NEC-2 is used to aide in the analysis of radiation properties of antennas. Computations are made based on the numerical solutions of integral equations for currents induced via incident fields or sources.

Using input data to specify the geometry, this code can determine various antenna characteristics [20]. Models developed in NEC-2 may include perfect or imperfect conductors, lumped element loading, and surface patches. A ground plane made up of a perfect or imperfect conductor may also be used in conjunction with the antenna. NEC-2 offers either voltage sources on the structure or an incident plane wave of linear or elliptical polarization as choices for the excitation of antennas. Output files created by NEC-2 provide results such as near electric or magnetic fields, radiated fields, gains, input impedance, and axial ratio.

Structures in NEC-2 are modeled on two basic elements: short and straight segments for modeling wires and flat patches for modeling surfaces. In order to obtain accurate results, the proper choice of the segments and dimensions for a model must be made. Accuracy of simulation results increases with the number of segments, however, the program running time increases rapidly as this number increases.

The definition of a wire segment is provided by the coordinates of its two end points and the wire radius. Both geometrical and electrical factors must be considered when modeling a wire structure. Using a piece-wise linear approximation for curves, the conductor path should be followed as closely as possible with each segment. Electrically, the segment length Δ relative to the wavelength λ must be considered. As a guideline, Δ should be less than $0.l\lambda$ at the desired frequency. Segments longer than that may be acceptable on long wires when there is no abrupt change in the geometry while shorter segments, 0.05λ or less, may be needed to model critical regions of an antenna. NEC-2 computes the current at the center of each segment, thus, the size of the segments determines the resolution in solving for the current. Segments less than about $10^{-3}\lambda$ should be avoided, since the similarity of the constant and cosine components of the current expansion leads to numerical inaccuracy [21].

In addition to segment modeling for antennas, NEC-2 offers several options for ground planes. When selecting a perfectly conducting ground plane, the code creates an image of the antenna structure. This generated image emulates a perfectly conducting ground producing a solution equivalent to a free-space model. A structure is permitted to be close to the ground or contacting it in this case. Using image theory and Fresnel plane-wave reflection coefficients, an imperfect ground can also be modeled in NEC. This is a fast method but will yield incorrect results for structures close to the ground. The reflection coefficient approximation for the near fields can yield reasonable accuracy if the structure is a least several tenths of a wavelength above the ground [21].

4.2.1 Verification of NEC-2

After learning about NEC-2, the simulation of a 10-turn conventional helix with a pitch angle of 12° and radius of 23.873mm is conducted. This geometry is chosen because its radiation characteristics can be readily estimated using the formulas presented in Chapter 2. The antenna is simulated over an infinite ground plane and is modeled using the equations describing the helix geometry [9]. Results for gain, axial ratio, and bandwidth are obtained and compared to corresponding values found using equations given in Chapter 2.

Using Equation (2.9), a peak gain of 14.3 dB is found at a circumference of 1.15λ. The NEC-2 results, shown in Figure 4.1(a), display a peak gain of 13.26 dB for a family of pointing angles. Previous work using Equation (2.9) has indicated that there can be a difference of 1 to 2 dB between the actual and predicted gains.

Figure 4.1(b) shows variations of the axial ratio versus frequency as found by NEC-2. It is noted that the axial ratio remains below 3 dB for the frequency range of 1.5 GHz to 2.5 GHz in directions with $\theta \le 10°$, indicating that the magnitudes of the electric field components are close to being equal and their phase difference is near ± 90°.

The bandwidth ratio can also be computed from an approximate formula and compared with simulation values. Using equation (2.14), a bandwidth ratio of 1.569 is found for the 10-turn conventional helix while simulation results indicated a ratio of 1.633 (1.5 GHz – 2.45 GHz).

This test case helped to ensure the proper utilization of NEC-2 and gain insight and experience into how to deal with the program once simulations are setup for the spiro-helical antenna.

4.3 Radiation Characteristics of Spiro-helical Antenna

Many simulations were performed to examine the radiation characteristics of the spiro-helical antenna. The values for the parameters used in the simulations were summarized in Table 4.2.

Table 4.2 Values of Parameters Used in Simulations

Number of turns, N:	7, 10, 13
Helical pitch angle, α:	7°, 8°, 9°, 10°, 12°, 14°, 16°
Spiral pitch angle, α':	5°, 10°, 15°, 20°, 25°, 30°, 35°, 40°, 60°, 80°
Helix radius, a:	11mm, 16mm, 21mm
Spiral radius, a':	1.5mm, 2mm, 3mm
Conductor radius, $r_{o:}$	0.2mm, 0.3mm, 0.4mm, 0.5mm

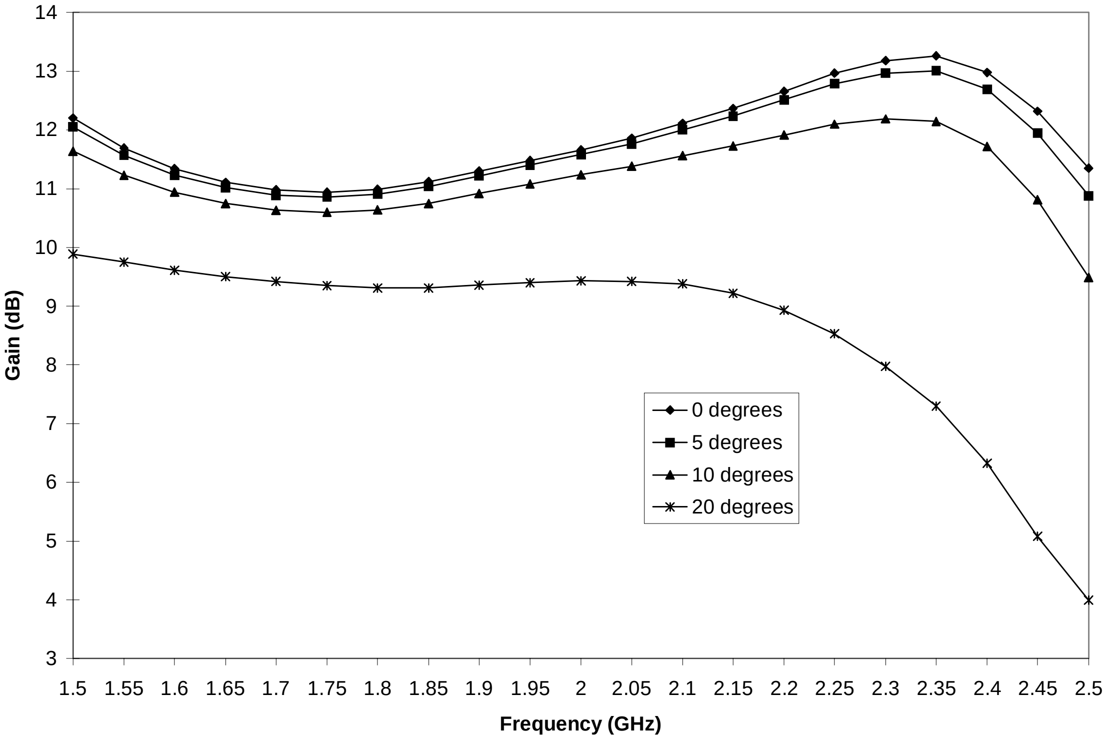

(a)

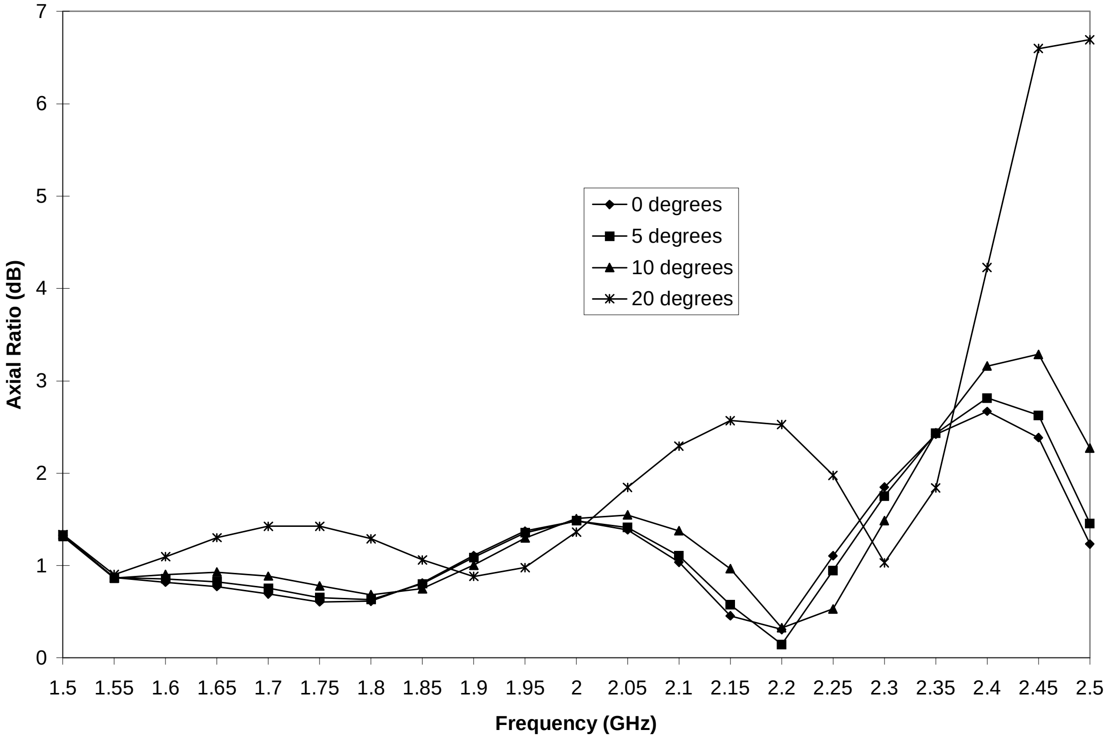

(b)

Figure 4.1 Variations of (a) gain and (b) axial ratio versus frequency for several angles θ off boresight for a 10-turn conventional helix with radius a = 23.873mm and pitch angle $\alpha = 12°$.

This section presents the numerical analysis of a 10 turn spiro-helical antenna with pitch angles α = 10° and α' = 30°, radii a = 16mm and a' = 2mm, and a conductor radius r_o = 0.2mm. The conductor radius for other cases is .5mm unless otherwise noted. This case is a representative example for which a prototype was also built and studied experimentally.

Using a Matlab® code, the input data for each simulation were created. Parameters within this code were varied for different geometries of the spiro-helical antenna. Most simulations were conducted in the frequency range 1.5 GHz to 2.5 GHz at 50 MHz intervals. Also, an infinite conducting plane was used as a ground plane throughout all simulations. With this choice of ground plane, radiated fields in the rear directions ($90° < \theta \le 180°$) do not exist, limiting the output data to the region$0° \le \theta \le 90°$.

Following the execution of NEC-2 code, the raw output data were filtered through a parsing program written in C++ and saved as a comma separate file (.csv). The data are presented in both tabular and graphical forms.

Once the output files were processed, a number of antenna characteristics, including gain, axial ratio, phase difference, input impedance, and far-field patterns could be readily examined.

4.3.1 Gain

Figure 4.2(a) shows variations of gain versus frequency for the representative spiro-helical antenna. A peak gain of 13.09 dB at 2.25 GHz and a minimum gain of 6.83 dB at 2.4 GHz is seen for $\theta = 0°$. Between 1.55 GHz and 2.3 GHz in Figure 4.2(a), the gain lies between the minimum and maximum values. It is clear that the bandwidth of this antenna for $\theta \le 20°$ is about 0.75 GHz for the gain. However, as will be seen later, the bandwidth for the axial-ratio is smaller and thus determines the overall bandwidth of the antenna. Gain results for the spiro-helical antenna with 7 and 13 turns were also produced and will be discussed in section 4.4.1. Comparison of these gain results indicates that gain increases with the number of turns as is the case with the conventional helix.

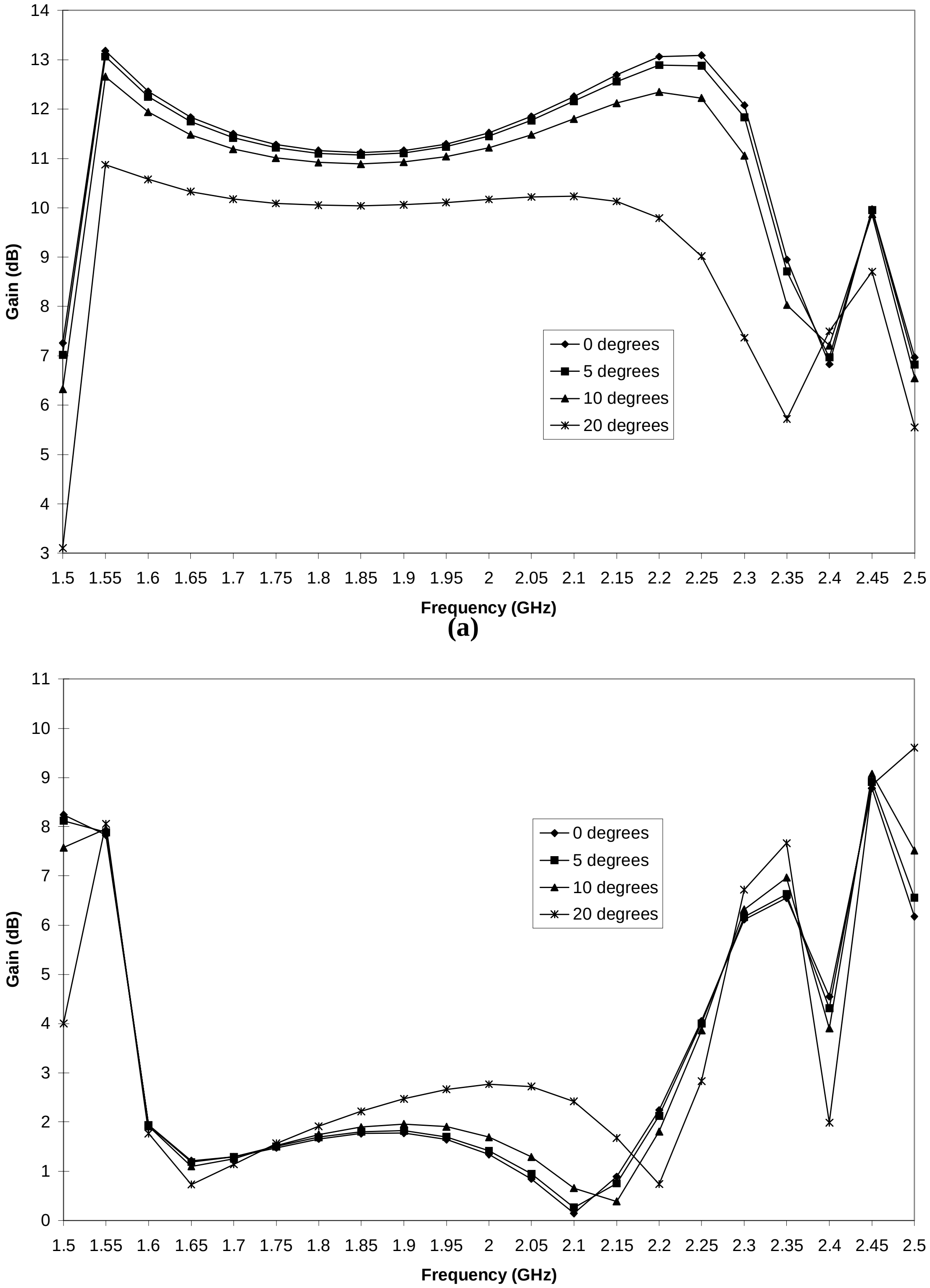

(a)

(b)

Figure 4.2 Variations of (a) gain and (b) axial ratio versus frequency for several values of θ for the representative 10-turn spiro-helical antenna with $\alpha = 10°$, $\alpha' = 30°$, a = 16mm, a' = 2mm, and r_o =0.2mm.

4.3.2 Axial Ratio

Figure 4.2(b) illustrates variations of axial ratio versus frequency. It is observed that for $\theta \leq 20°$, the axial ratio is less than 3 dB in the frequency range 1.6 GHz < f < 2.2 GHz. This range corresponds to a bandwidth of 600 MHz $\left(\frac{f_u}{f_l} = 1.375\right)$. This bandwidth is a measure of the overall bandwidth of the antenna, because it is smaller than the bandwidth for the gain (it is assumed that the antenna can be matched to the transmission line by means of a suitable matching network.)

4.3.3 Input Impedance

The real and imaginary parts of input impedance of the 10-turn representative spiro-helical antenna are shown in Figure 4.3. It should be noted however that the input impedance results are not reliable. Past experience with the NEC-2 software has indicated that the input impedance data do not agree well with the results obtained from measurement and other numerical methods. This is particularly true for the imaginary part of the input impedance. When considering the feed unit as well as the connection to the antenna, the results become very sensitive to even small changes in the geometry. Thus, these results are presented as a basic guide and should not be relied upon heavily. The input impedance characteristics of an antenna can be altered as desired by means of matching units. Therefore, the input impedance bandwidth, unlike the gain and axial-ratio bandwidths, can be controlled externally. A more in-depth investigation of the input impedance is necessary but is beyond the scope of this thesis. This study should be pursued in further research and development of the spiro-helical antenna.

4.3.4 Radiation Patterns

The far-field patterns for the representative spiro-helical antenna are displayed in Figures 4.4(a) through 4.4(t). These patterns show variations of normalized power density versus elevation angle θ in the $y = 0$ plane. Examination of the patterns indicate that the half power beamwidth varies between 40° and 60° for the majority of frequencies between 1.5 GHz and 2.5 GHz. As seen in these figures, there is an increasing trend in the HPBW beginning at 1.5 GHz. Starting at 44°, HPBW increases until 1.85 GHz where

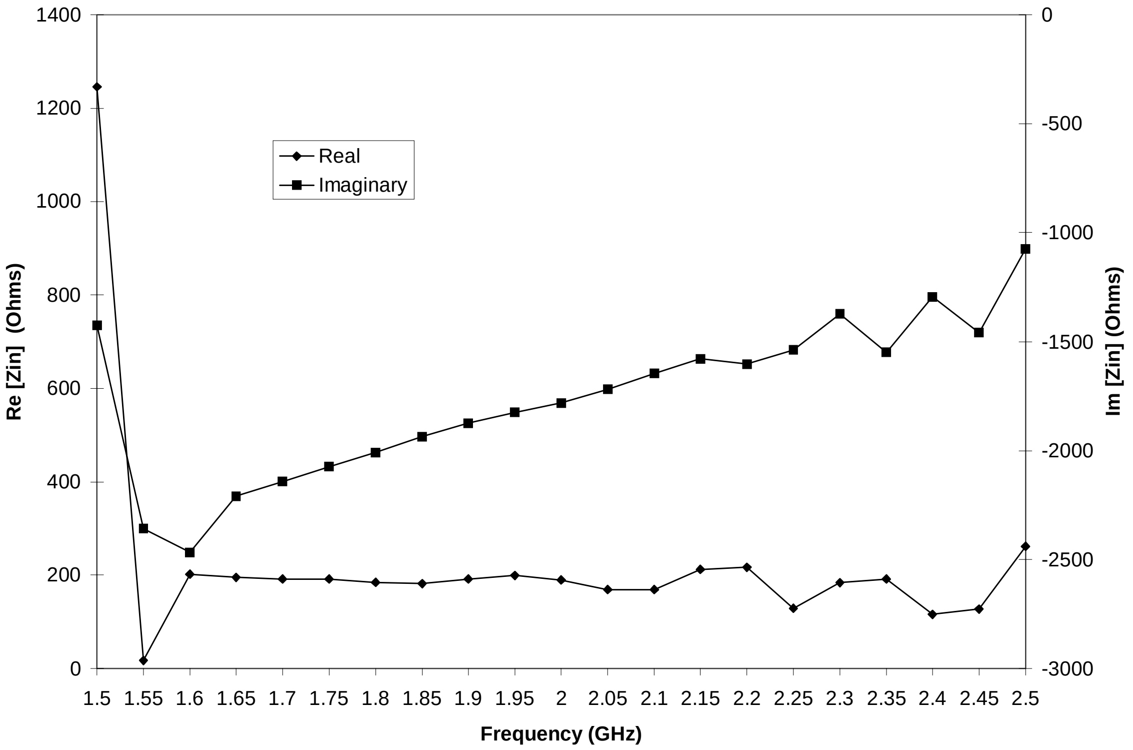

Figure 4.3 Input impedance versus frequency for the representative 10-turn spiro-helical antenna with $\alpha = 10°$, $\alpha' = 30°$, $a = 16$mm, $a' = 2$mm and $r_o = 0.2$mm.

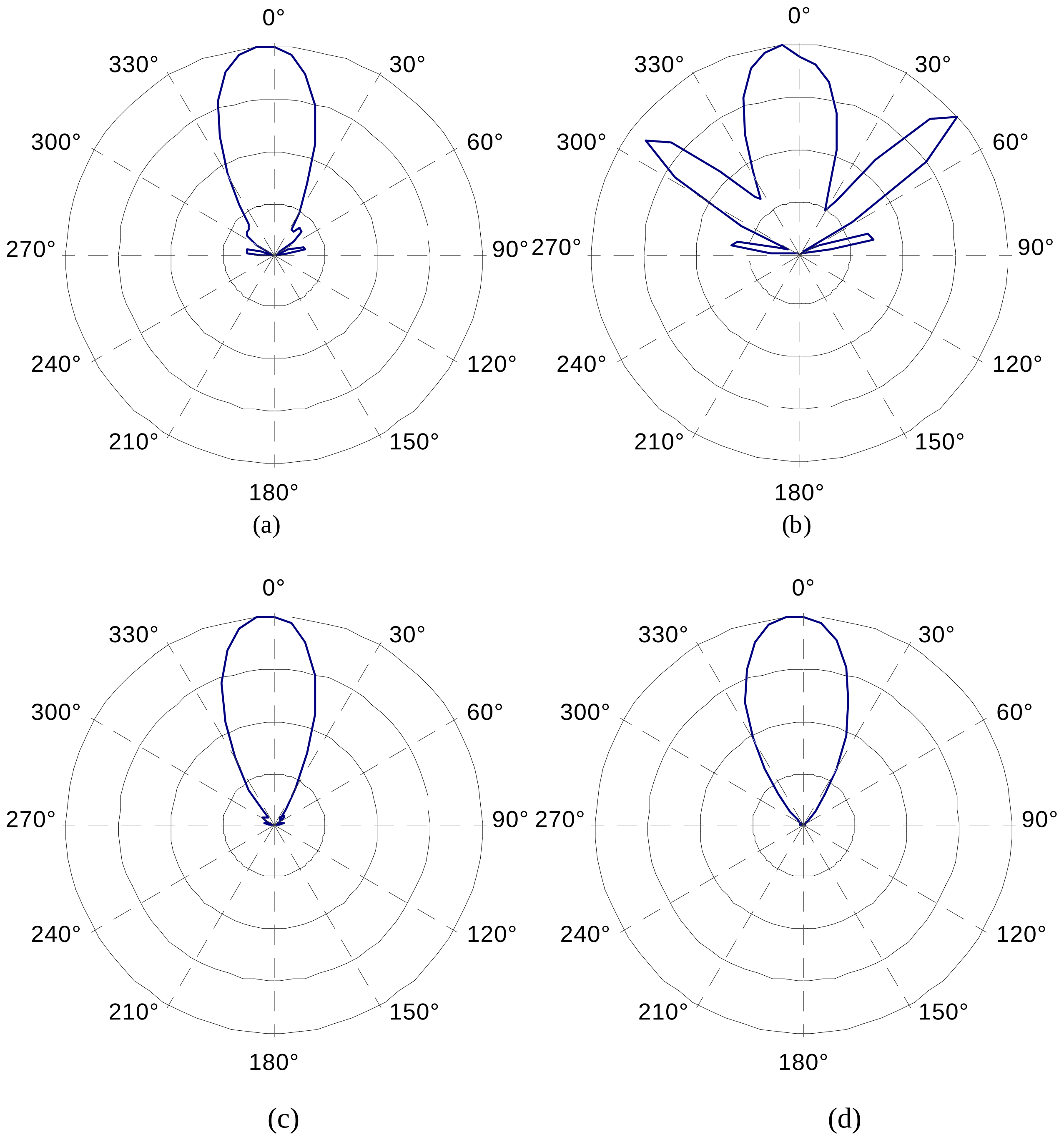

(a) (b)

(c) (d)

Figure 4.4 Computed power patterns for the representative case at (a) 1.5 GHz, (b) 1.55 GHz, (c) 1.6 GHz, and (d) 1.65 GHz.

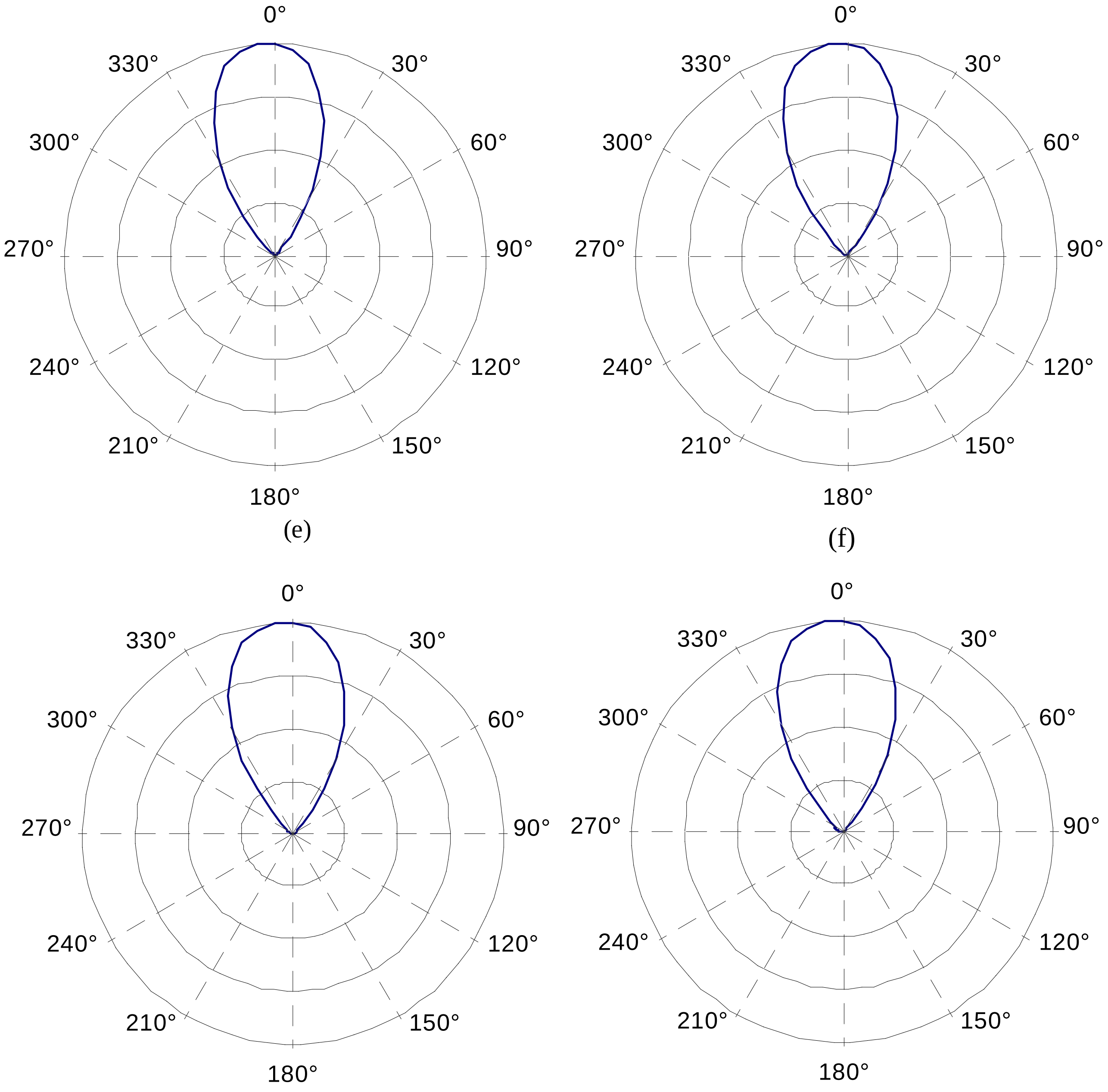

(e) (f)

(g) (h)

Figure 4.4 Computed power patterns for the representative case at (e) 1.7 GHz, (f) 1.75 GHz, (g) 1.8 GHz, and (h) 1.85 GHz.

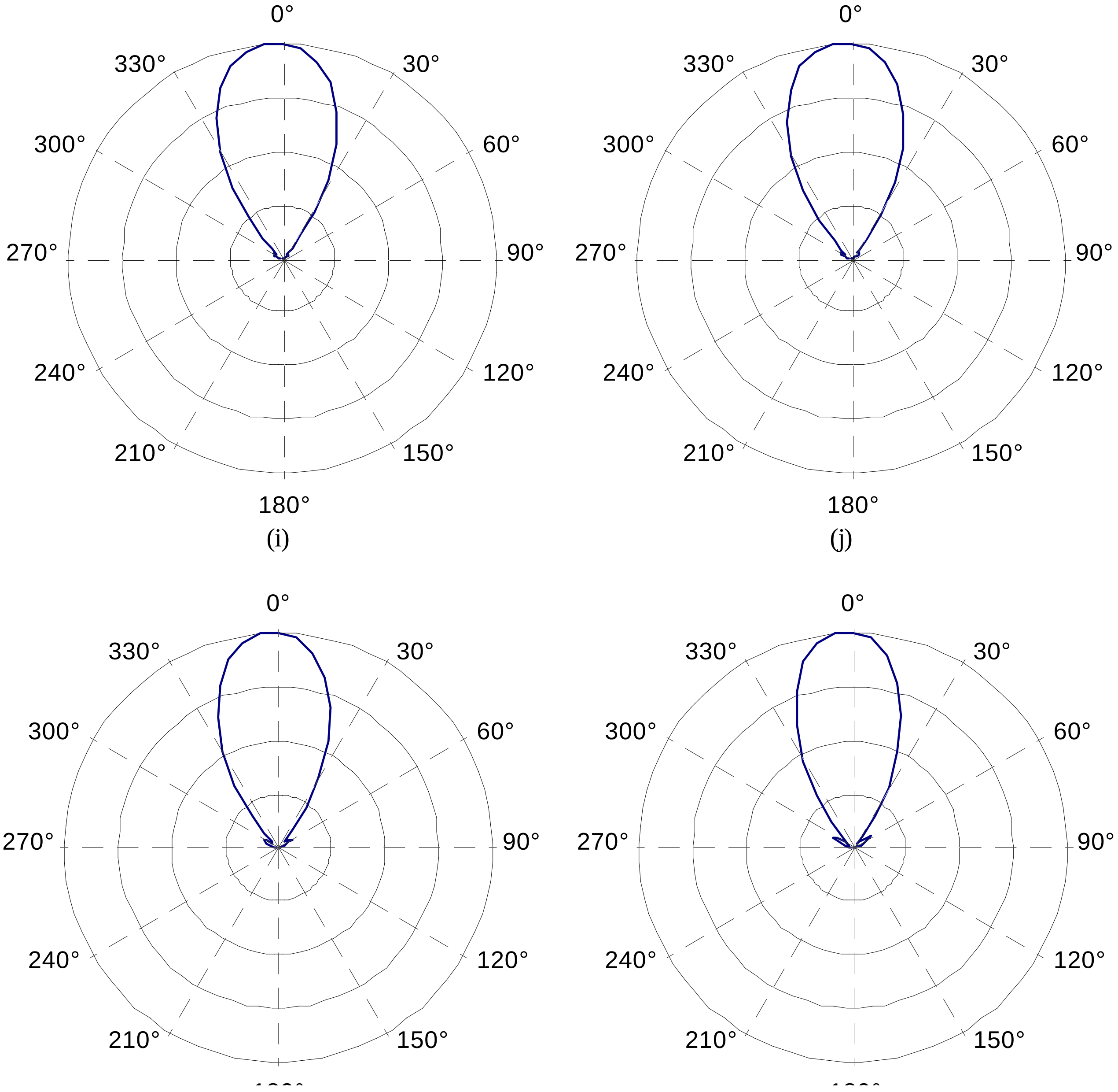

(i) (j)

(k) (l)

Figure 4.4 Computed power patterns for the representative case at (i) 1.9 GHz, (j) 1.95 GHz, (k) 2.0 GHz, and (l) 2.05 GHz.

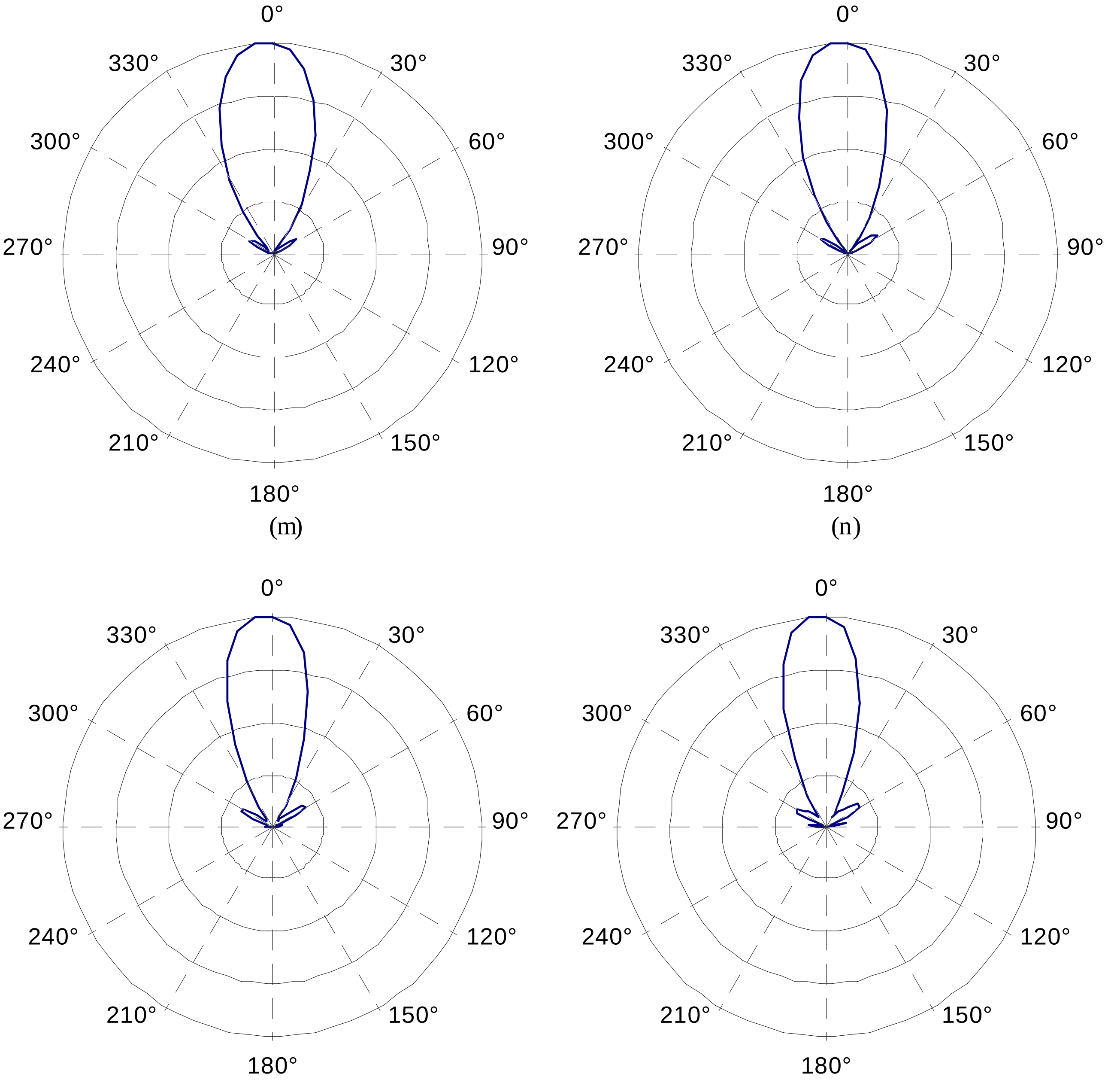

(m) (n)

(o) (p)

Figure 4.4 Computed power patterns for the representative case at (m) 2.1 GHz, (n) 2.15 GHz, (o) 2.2 GHz, and (p) 2.25 GHz.

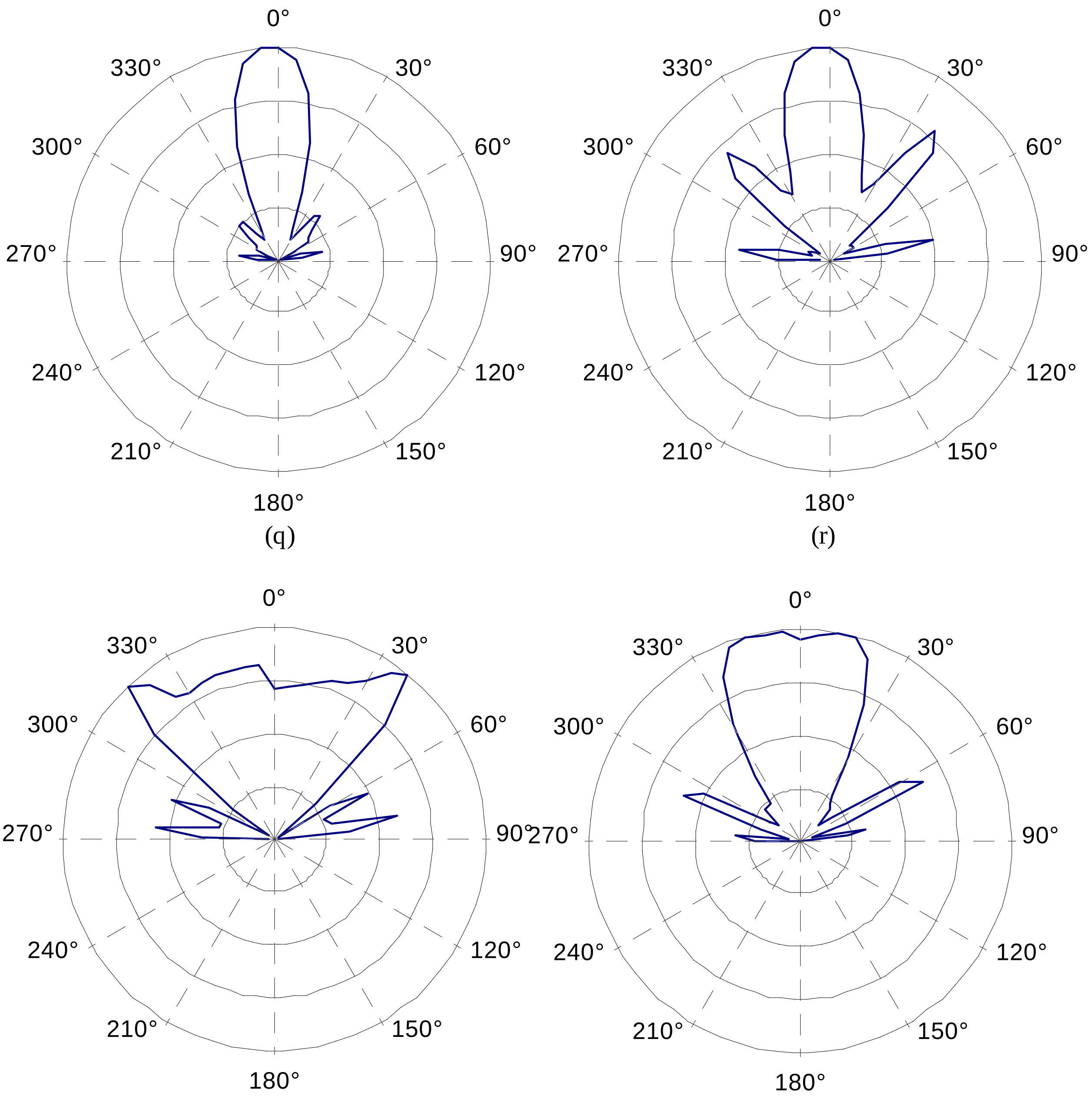

(q) (r)

(s) (t)

Figure 4.4 Computed power patterns for the representative case at (q) 2.3 GHz, (r) 2.35 GHz, (s) 2.4 GHz, and (t) 2.45 GHz.

it reaches a maximum of 57°. A decreasing trend is then seen starting at 1.9 GHz until 2.3 GHz. Due to the fact that an infinite ground plane was used for the simulations, there are no backlobes. Also, sidelobes with a level of about 10 dB exist for $f < 1.65$ GHz and $f > 2.1$ GHz. In the higher frequency range sidelobe levels increase with frequency as Figures 4.4(m) to 4.4(t) indicate.

4.4 Effects of Parameters on Radiation Characteristics

The geometry of the spiro-helical antenna involves five parameters including the number of turns N, pitch angles α and α' and radii a and a'. Each of these parameters influences the gain characteristics of the antenna and the overall bandwidth. With the exception of section 4.4.1, which describes the effect of number of turns, in all other sections the number of turns is assumed to be 10. For all results presented in sub-section 4.4.1 through 4.4.5, the radius of conductor wire is r_o= 0.5 mm.

4.4.1 Number of Turns, N

Three spiro-helical antennas with 7, 10, and 13 turns were examined. All other parameters of the antennas had the same values as the representative 10-turn antenna (a = 16mm, a' = 2mm, α = 10°, and α' = 30°). Figure 4.5(a) illustrates the gain characteristics of the three antennas while Figure 4.5(b) shows variations of their axial ratios. With a peak gain of 13.13 dB at 2.35 GHz, the 7 turn antenna has the lowest gain. This antenna provides a gain based bandwidth ratio of 1.516 (1.65 GHz – 2.5 GHz) and an axial-ratio based bandwidth of 1.25 (1.8 GHz – 2.25 GHz). The 10 turn spiro-helical antenna, as mentioned in the previous section, maintains a peak gain of 13.95 dB with a gain based bandwidth ratio of 1.441 (1.7 GHz – 2.45 GHz) and an axial-ratio based bandwidth of 1.286 (1.75 GHz – 2.25 GHz). As the number of turns increase to 13 turns, there is an increase in the peak gain to 14.47 dB and the gain based bandwidth ratio increases to 1.469 (1.6 GHz – 2.35 GHz). At the same time, the axial-ratio based bandwidth is maintained at 1.286 (1.75 GHz – 2.25 GHz). In summary, the gain increases with the number of turns but is expected to saturate if number of turns becomes very large. Also, at a larger number of turns, the gain based bandwidth is smaller and the peak gain occurs at a lower frequency. The axial ratio, however seems not to be affected significantly by the number of turns.

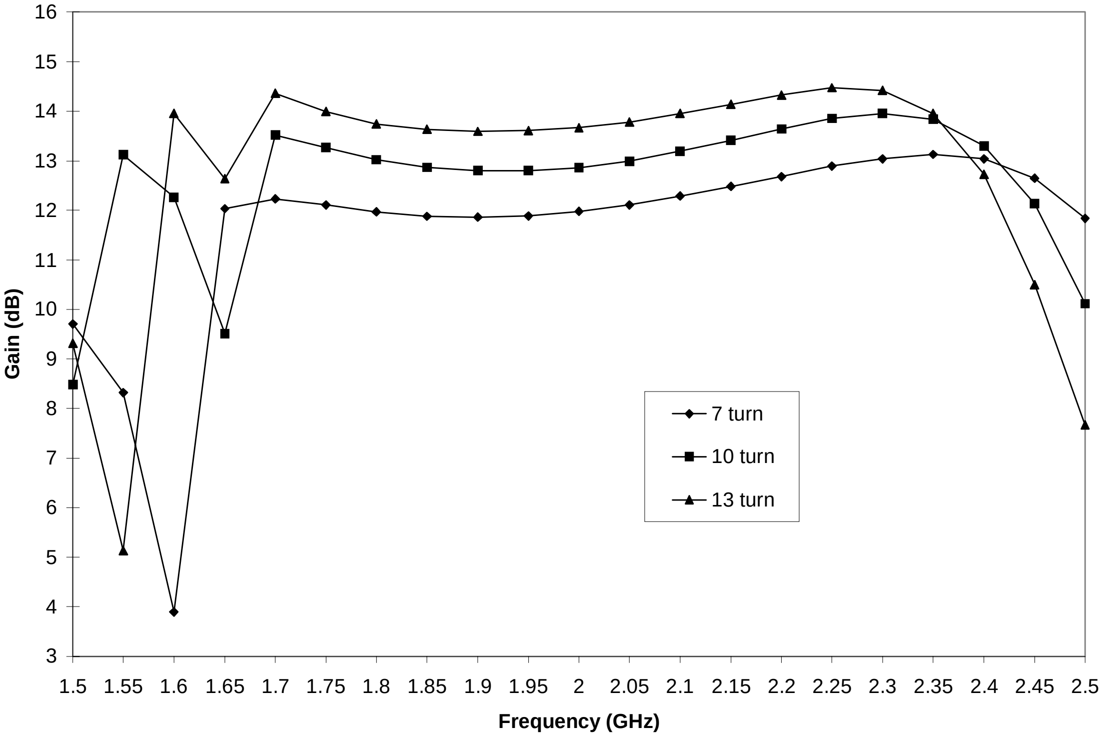

(a)

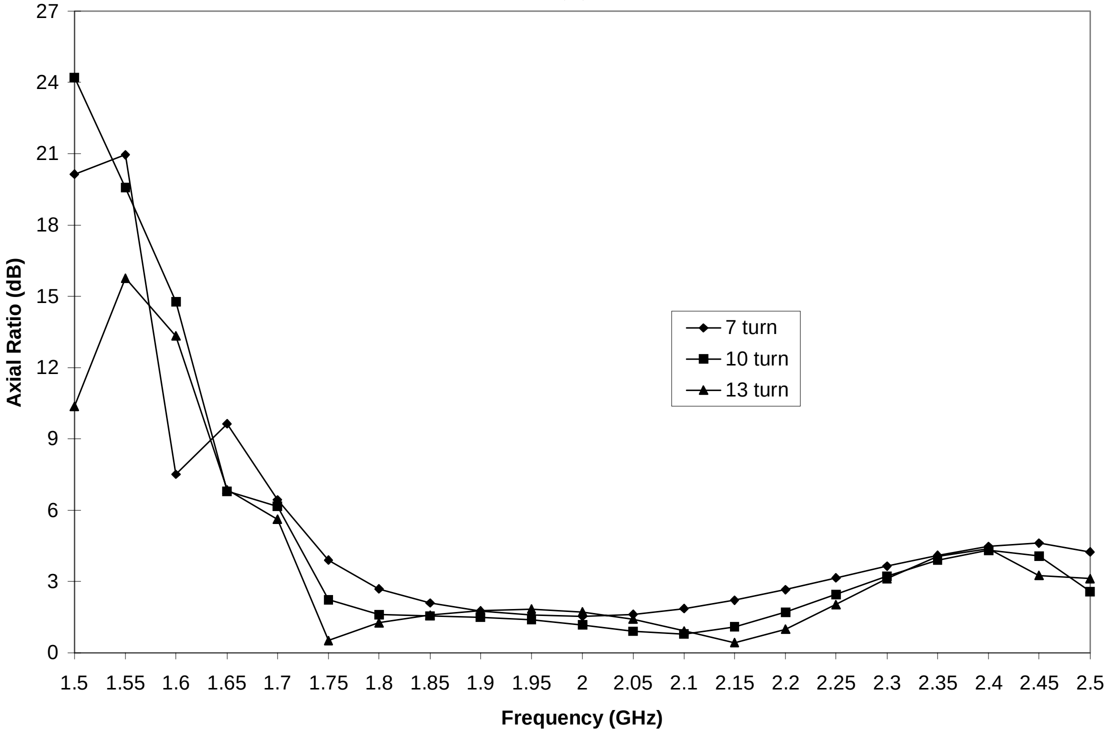

(b)

Figure 4.5 Variations of (a) gain and (b) axial ratio versus frequency for 7, 10, and 13-turn spiro-helical antennas with a = 16mm, a' = 2mm, α = 10°, and α' = 30°.

4.4.2 Pitch Angle, α

Figures 4.6(a) and 4.6(b) show the variations of gain and axial ratio of a 10-turn spiro-helical antenna versus pitch angle, α, at several frequencies. The parameters a, a', and α' for this helix are the same as those for the representative example discussed in section 4.3. Examination of Figure 4.6(a) indicates that the peak gain at frequencies above 1.6 GHz occurs at about $\alpha = 10°$. This is an interesting characteristic making the geometry with $\alpha = 10°$ a strong candidate in situations where higher gain is desired. There is a gradual decline in the gain as α increases beyond 10°. On the other hand, examination of Figure 4.6(b) indicates that when the pitch angle is in the range $13.5° \leq \alpha \leq 15°$, the axial ratio is below 3 dB at all frequencies. Thus, peak gain and maximum axial-ratio based bandwidth do not occur at the same pitch angles. The pitch angle $\alpha = 9°$ also seems desirable, because at this pitch angle relatively high gain and low axial ratio can be achieved and the antenna has a smaller size. Pitch angles larger than 15°, however, should be avoided in order to prevent a substantial drop in the gain as seen from Figure 4.6(a).

4.4.3 Pitch Angle, α'

Figure 4.7(a) displays the gain characteristics versus pitch angle α' for a 10 turn spiro-helical antenna. The parameters a, a', and α' for this helix are the same as the representative case discussed in section 4.3. Numerical results at $f = 1.95$ GHz and $\theta = 0°$ for several values of α show that the highest gain is achieved when $\alpha = 10°$ and $\alpha' = 30°$.

Figure 4.7(b) exhibits the axial ratio versus α' at 1.95 GHz for several values of α. It is noted that for all values of α, the axial ratio remains relatively constant and below 3dB. The closest values to 0 dB axial ratio are observed for $\alpha = 14°$. When comparing Figures 4.7(a) and 4.7(b), we can see that a tradeoff exists between gain and axial ratio. The antenna with $\alpha = 10°$ provides higher gain and higher axial ratio, while the antenna with $\alpha = 14°$ offers less gain but an axial ratio closer to 0 dB.

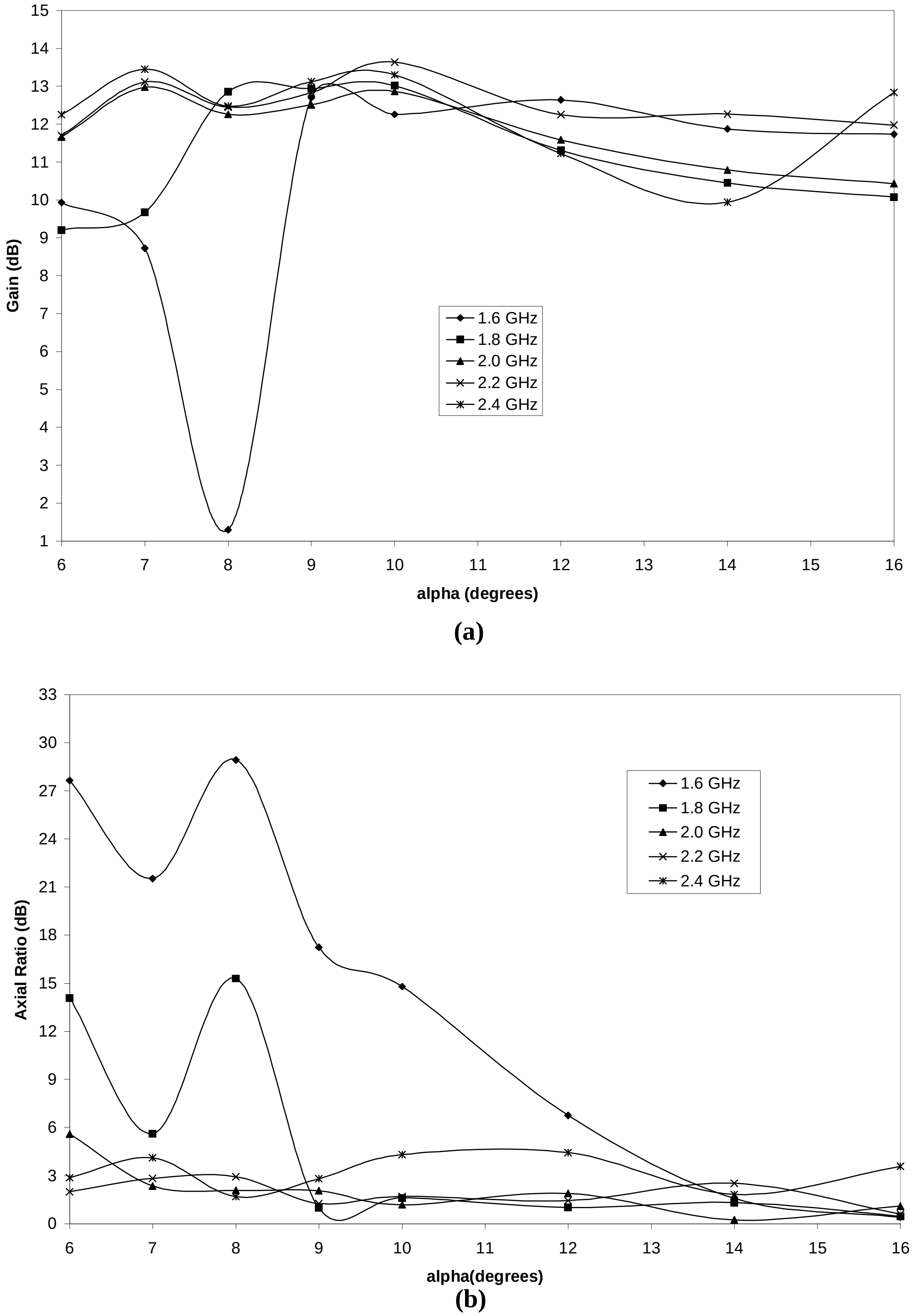

(a)

(b)

Figure 4.6 Variations of (a) gain and (b) axial ratio versus α at several frequencies for the representative 10-turn spiro-helical antenna with $\alpha' = 30°$, $a = 16$mm, and $a' = 2$mm.

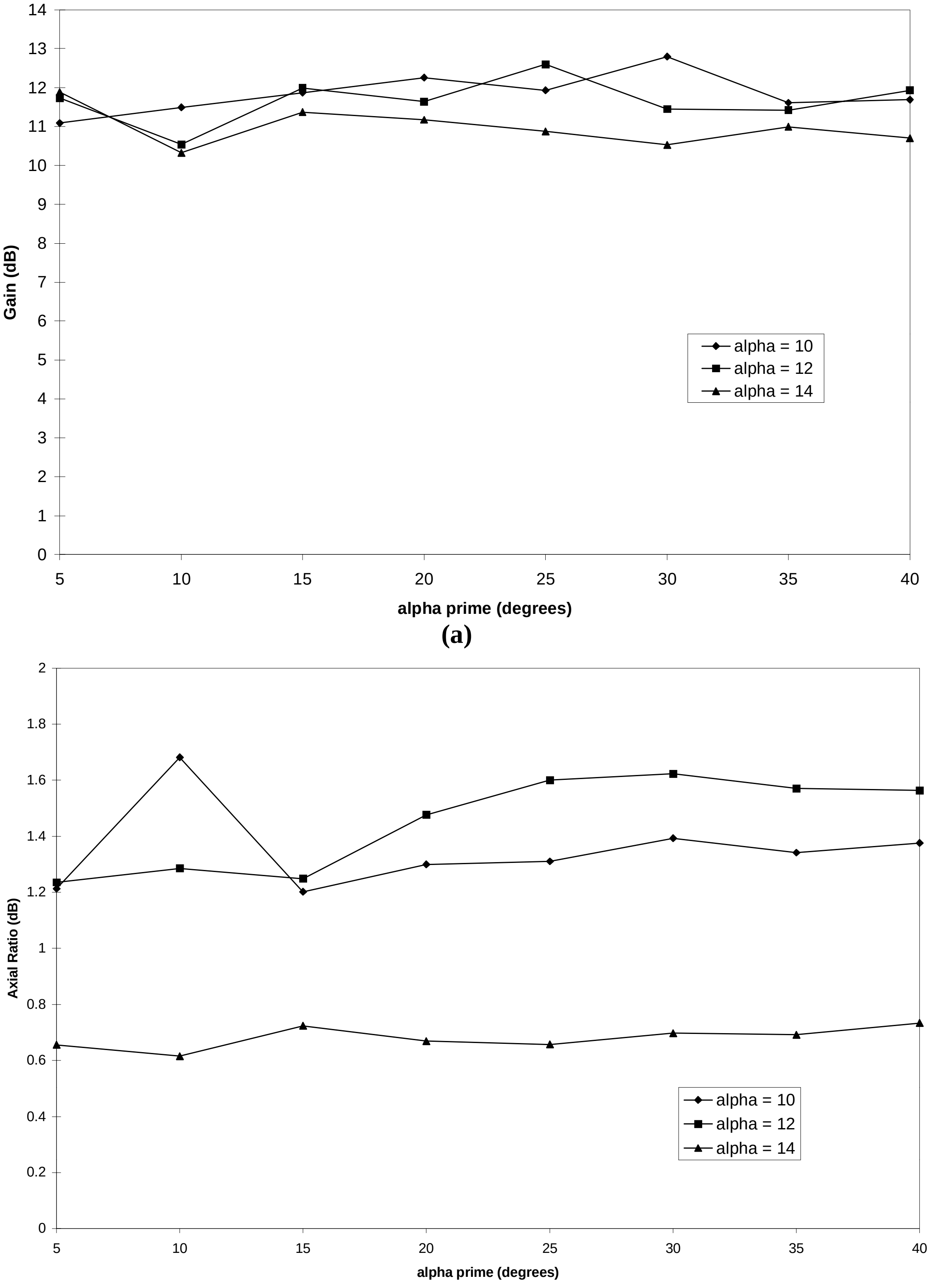

(a)

(b)

Figure 4.7 Variations of (a) gain and (b) axial ratio vs. α' for several values of α at 1.95 GHz for a 10-turn spiro-helical antenna with a = 16mm and a' = 2mm.

4.4.4 Radius, *a*

A large percentage of the simulations performed focused on the changes in the pitch angles while keeping the radii constant. Several simulations were conducted that kept the pitch angles constant while the radii changed. Keeping $\alpha = 10°$, $\alpha' = 30°$, $a' = 2$mm, and the number of turns equal to 10, the radius a is changed to 11mm, 16mm, and 21mm. Figures 4.8(a) and 4.8(b) show the gain and axial ratio characteristics for these three cases. Compared to the representative case (a = 16mm), the following observations are made.

For a = 11mm, there is a shift in the frequency range of operation. For the 10-turn representative case, the frequency range of 1.5 GHz to 2.5 GHz contains the peak gain and the lowest axial ratio. In this case, however, the frequency range extends to 3.5 GHz with a peak gain of 13.29 dB occurring at 3.05 GHz. The gain based bandwidth ratio is 1.675 (2.0 GHz – 3.35 GHz) while the bandwidth ratio for the axial-ratio is 1.271 (2.4 GHz – 3.05 GHz). The antenna with a = 21mm has a peak gain of 14.18 dB at 1.85 GHz and gain based bandwidth ratio of 1.286 (1.4 GHz – 1.8 GHz). The axial-ratio based bandwidth, which defines the overall bandwidth, is slightly smaller than that for the representative case at 1.375 (1.6 GHz – 2.2 GHz). Calculating the outer circumference $\overline{C} = 2\pi(a + 2a')$ for each case, it is found that $\overline{C} = 0.958\lambda, 0.963\lambda, \text{and}\, 0.969\lambda$ for a =11mm, 16mm, and 21mm respectively. Thus, it may be concluded that the peak gain occurs when the outer circumference of spiro-helical antenna is about 0.96 wavelength. The peak gain for a conventional helix occurs at a circumference of about 1.2λ.

4.4.5 Radius, *a′*

Now, the effect of spiral radius a' on radiation characteristics, while keeping all other parameters constant, is examined. Figures 4.9(a) and 4.9(b) show the gain and axial ratio characteristics for several values of a'. Three cases are examined. The first case is with $\alpha = 10°$, $\alpha' = 30°$, a = 16mm, and a' = 1.5mm. This geometry produced a peak gain of 13.12 dB at 2.55 GHz and a gain based bandwidth ratio of 1.541 (1.85 GHz – 2.85 GHz). The axial-ratio based bandwidth is found to be 1.436 (1.95 GHz – 2.8 GHz).

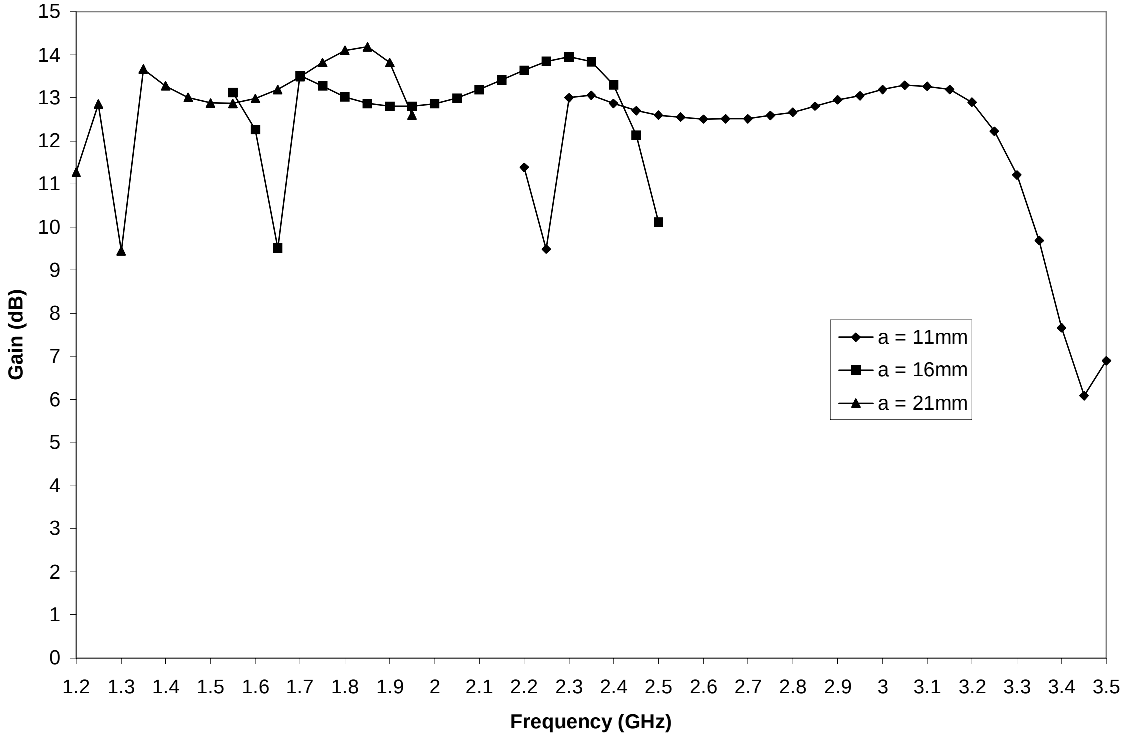

(a)

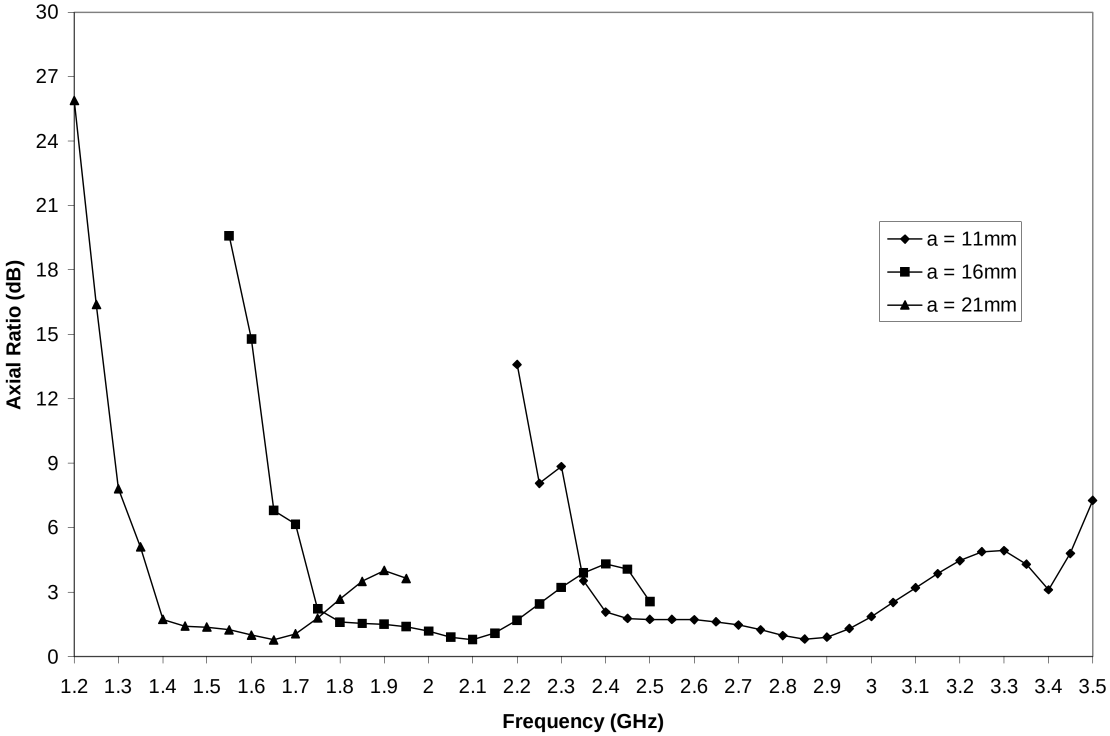

(b)

Figure 4.8 Variations in (a) gain and (b) axial ratio versus frequency for several values of *a* in a 10-turn spiro-helical antenna with $\alpha = 10°$, and $\alpha' = 30°$ $a' = 2\text{mm}$.

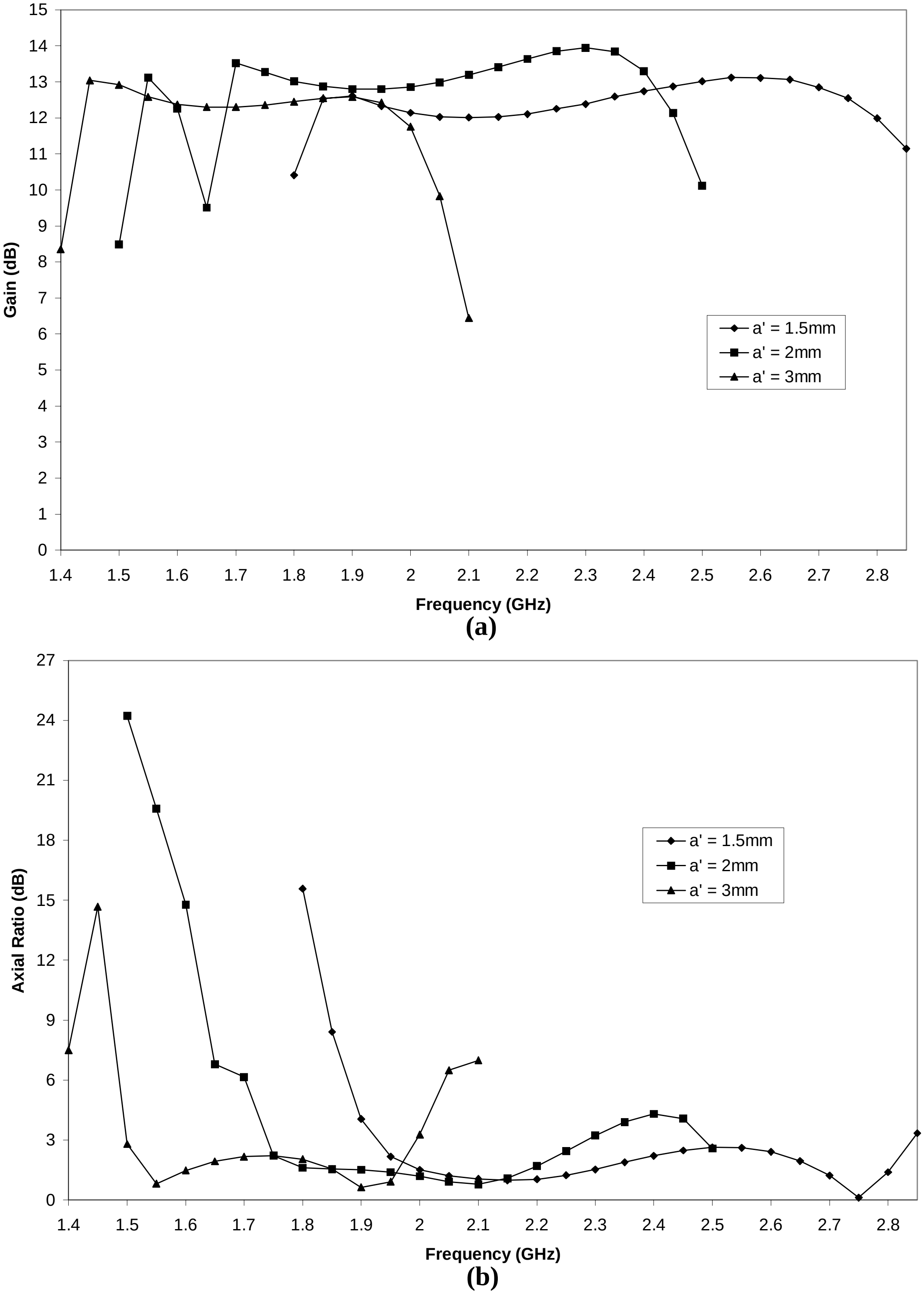

Figure 4.9 Variations in (a) gain and (b) axial ratio versus frequency for several values of a' in a 10-turn spiro-helical antenna with a = 16mm, $\alpha = 10°$, and $\alpha' = 30°$.

The second antenna has a radius a' = 2mm and maintains a peak gain of 13.95 dB with a gain based bandwidth ratio of 1.441 (1.7 GHz – 2.45 GHz) and an axial-ratio based bandwidth of 1.286 (1.75 GHz – 2.25 GHz). This case is, in fact, the representative case.

The third case is an antenna with the parameter a' = 3mm. This geometry leads to a gain based bandwidth of 1.379 (1.45 GHz – 2.0 GHz) and an axial-ratio based bandwidth of 1.3 (1.5 GHz – 1.95 GHz).

4.4.6 Conductor Radii, r_o

Figures 4.10(a) and 4.10(b) illustrate the effects of varying the wire radius on the gain and axial ratio properties respectively. The conductor wire radii of 0.2mm, 0.3mm, 0.4mm, and 0.5mm are examined. All other parameters in this investigation are the same as those in the representative case. It can be seen that there is little change in the values of gain and axial ratio among most of these cases. Perhaps the most significant effect is on the bandwidth.

It is noted that increasing the conductor radius the bandwidth ratio increases slightly and also shifts to higher frequencies. The gain based bandwidth ratio increases from 1.438 (1.6 GHz -2.3 GHz) for r_o = 0.2mm to 1.441 (1.7 GHz - 2.45 GHz) for r_o = 0.5mm conductor. On the other hand, the bandwidth ratios for the axial-ratio are 1.286 and 1.333 for r_o = 0.2mm and 0.5mm respectively. Thus, variations in the conductor wire radius, as long as the thin-wire approximation holds, do not make a huge impact on radiation properties of the spiro-helical antenna.

4.5 Comparison with Conventional Helix

A number of simulations for the conventional helix were run in order to find the one matching the radiation properties of the representative spiro-helical antenna most closely. A helix with a pitch angle of 12°, 15 turns, and a radius of 22.857 mm was found to have gain and axial ratio characteristics nearly matching those of the representative case spiro-helical antenna. Figures 4.11(a) and 4.11(b) compare the gain and axial ratio characteristics for “nearly equivalent” conventional helical and the proposed spiro-helical antennas. The 3-dB gain bandwidth for the spiro-helical antenna is about 0.7 GHz while that for the conventional helix is 1 GHz. The axial-ratio based bandwidth, on the other hand as noted from Figure 4.11(b), is

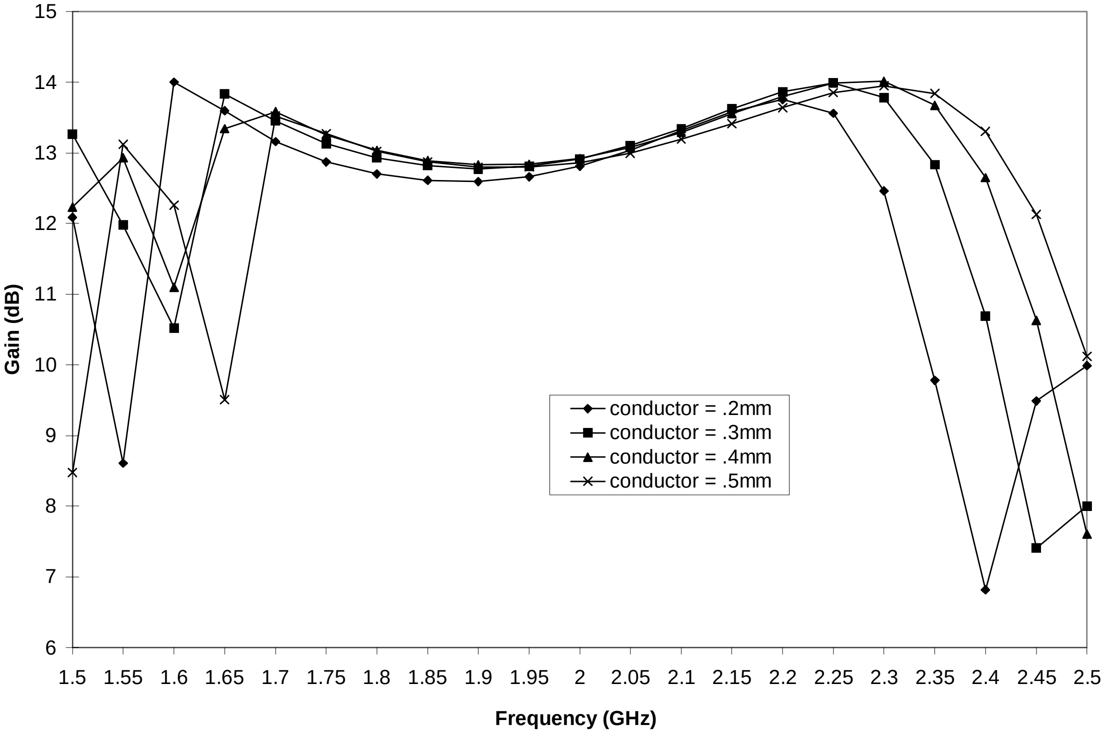

(a)

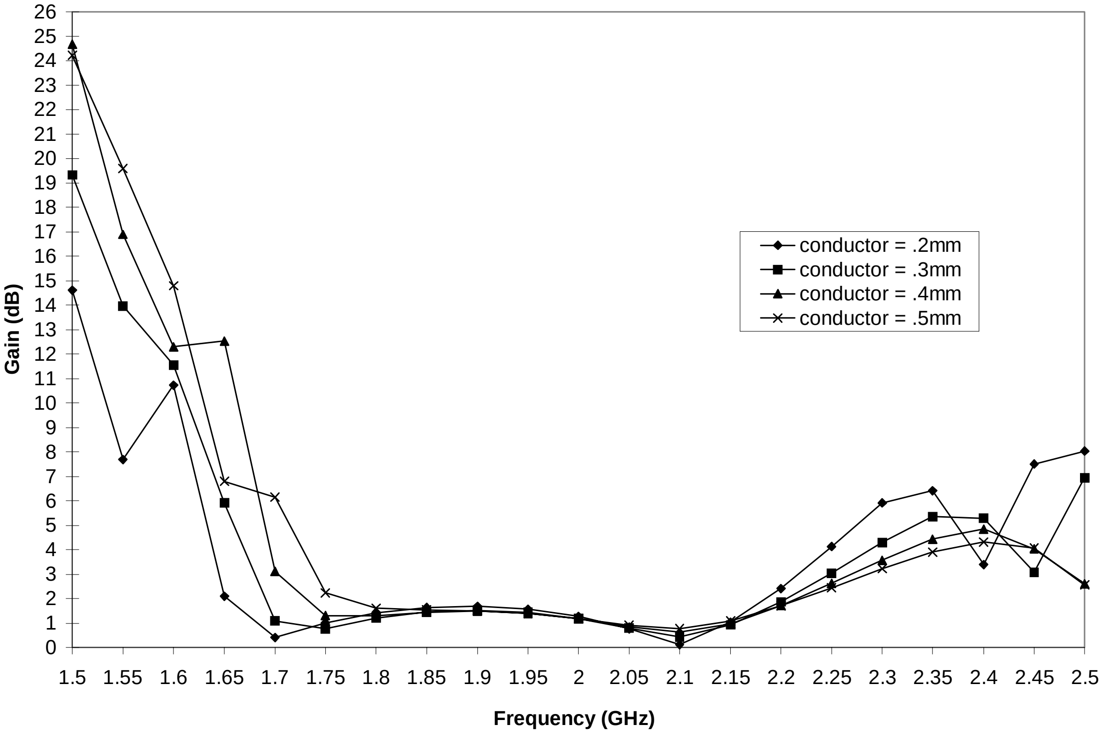

(b)

Figure 4.10 Variations in (a) gain and (b) axial ratio versus frequency for several conductor radii values in a 10- turn spiro-helical antenna with a = 16mm, α = 10°, α' = 30°, a' = 2mm.

wider for the conventional helix. The axial-ratio based bandwidth of this antenna is 1.64 (1.525 GHz- 2.5 GHz), whereas that of the spiro-helical antenna is about 1.2. Now let us compare the volumes of the two antennas. Using a radius of 22.857 mm and a height of 457.89mm $(=15\times2\pi\times22.87\times\tan12^{\circ})$ for the conventional helix, and a radius of 20mm (= a + 2a') and a height of 221.58mm $(=10\times2\pi\times20\times\tan10^{\circ})$ for the spiro-helical antenna, a volume ratio of 2.7 is obtained. In other words, this new antenna can provide radiation characteristics comparable to those of a conventional helix while occupying a volume 2.7 times smaller.

Further investigation of the volume reduction led to another comparison between a conventional helix and a smaller spiro-helical antenna. Figures 4.12(a) and 4.12(b) compare the gain and axial ratio characteristics for a 10-turn conventional helical and a 10-turn spiro-helical antenna different from the representative case. The 10-turn spiro-helical antenna used has the parameters $\alpha = 7°$, $\alpha' = 30°$, a = 16mm, and a' = 2mm while the 10-turn conventional helix has pitch angle $\alpha = 14°$ and radius a = 24.37mm. These dimensions give the spiro-helical antenna a height of 154.30mm $(=10\times2\pi\times20\times\tan7^{\circ})$ and the conventional helix a height of 381.77mm $(=10\times2\pi\times24.37\times\tan14^{\circ})$. The 3-dB gain based bandwidth of these two antennas is about 800 MHz. The spiro-helical antenna is able to maintain a larger and more uniform gain for this bandwidth, but the tradeoff comes with the axial ratio. The axial-ratio based bandwidth, illustrated in Figure 4.12(b), is once again wider for the conventional helix. The axial-ratio based bandwidth of this antenna is 1.67 (1.5 GHz- 2.5 GHz), whereas that of the spiro-helical antenna is 1.294 (1.7 GHz – 2.2 GHz). In this case, the spiro-helical antenna occupies a volume 3.67 times smaller than the conventional helix. In summary, it can be stated that the spiro-helical antenna occupies a volume 2.5 to 3.7 times smaller than a conventional helix with comparable radiation properties.

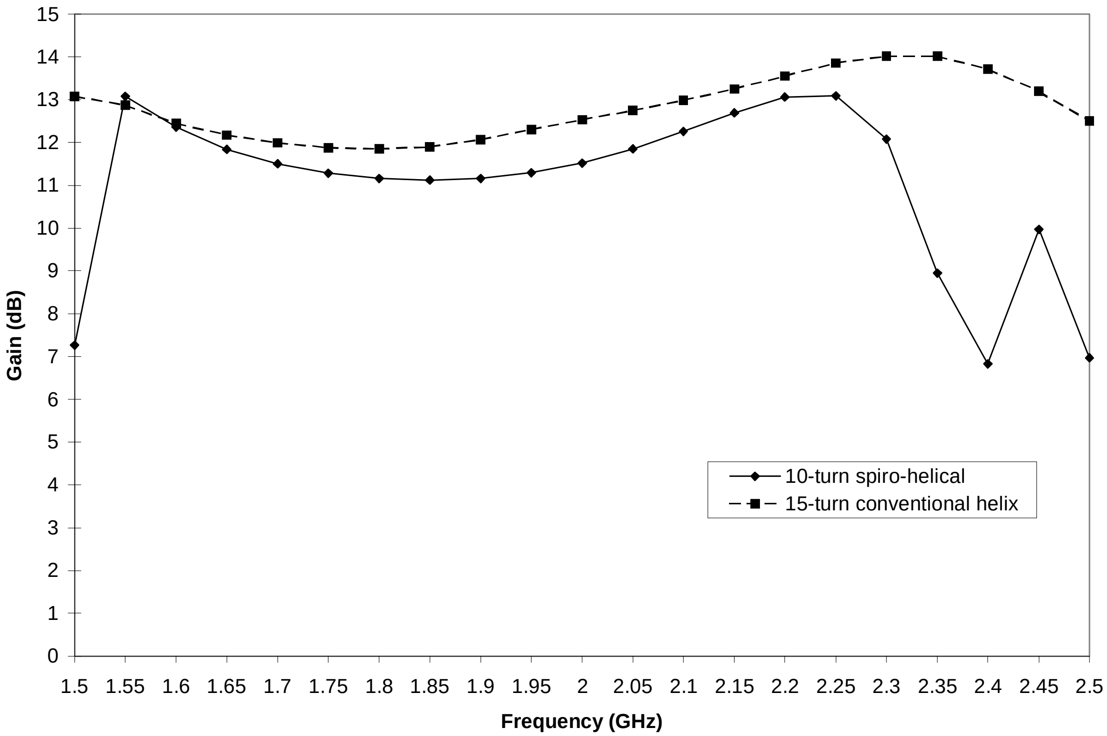

(a)

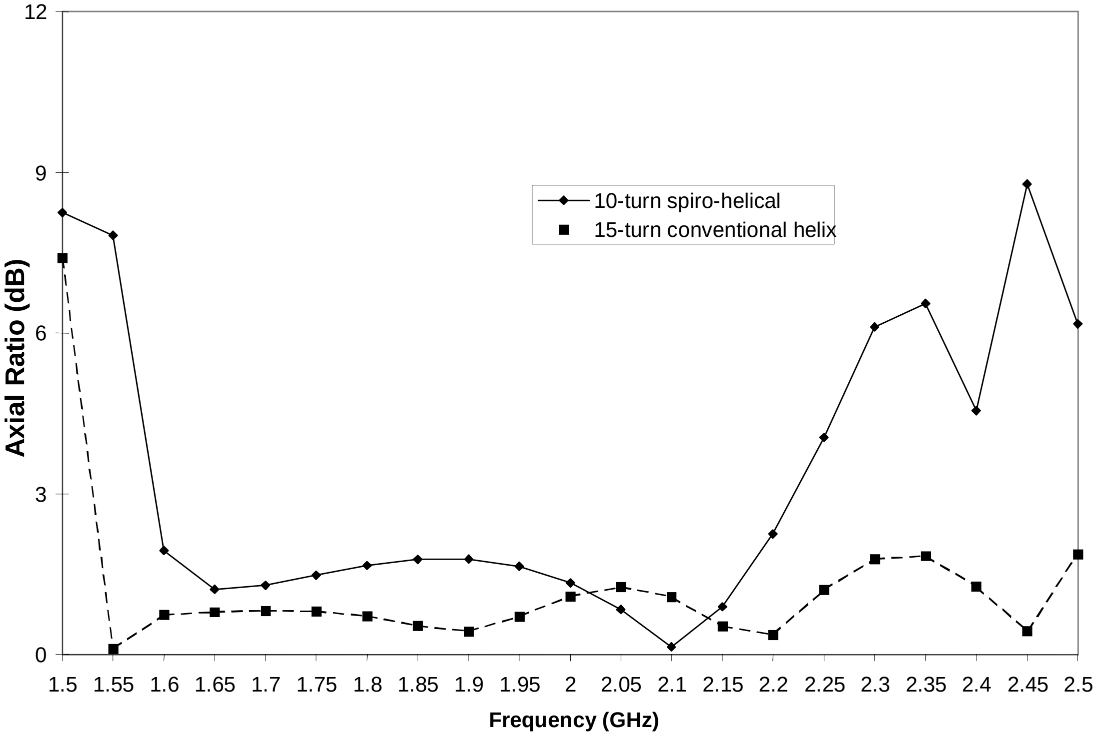

(b)

Figure 4.11 Comparison of (a) gain and (b) axial ratio characteristics for a 15-turn conventional helix with radius a = 22.857 mm and pitch angle α = 12° and a 10-turn spiro-helical antenna with α = 10°, α' = 30°, a = 16mm, and a' = 2mm.

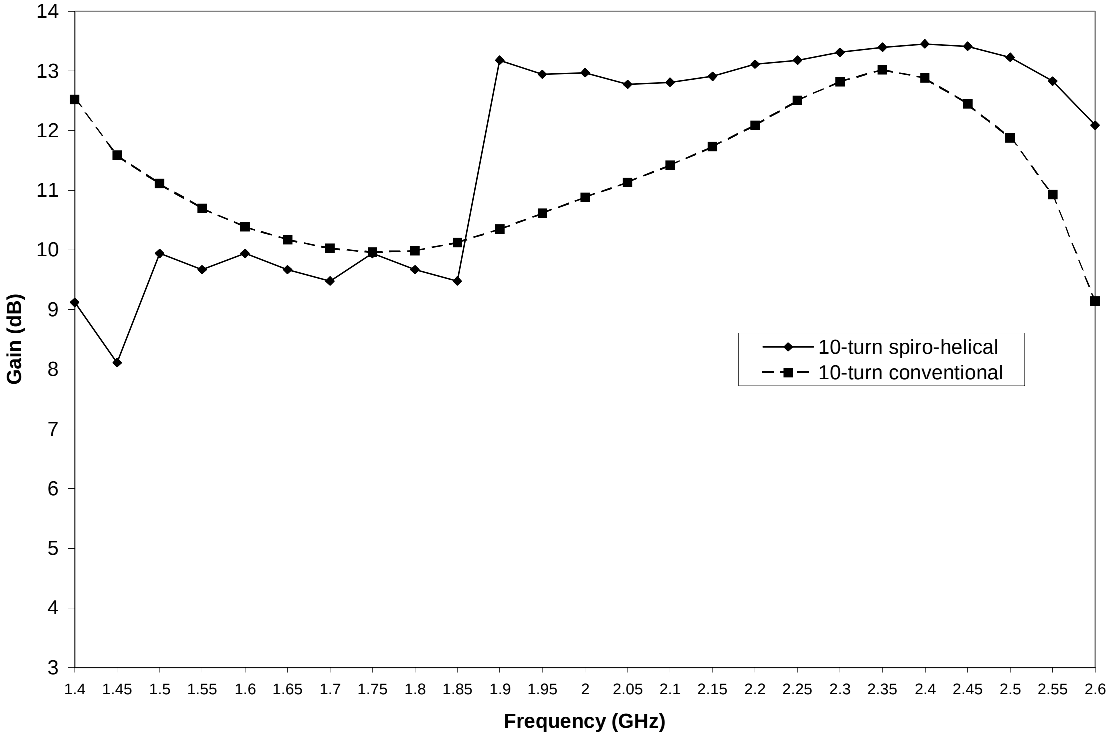

(a)

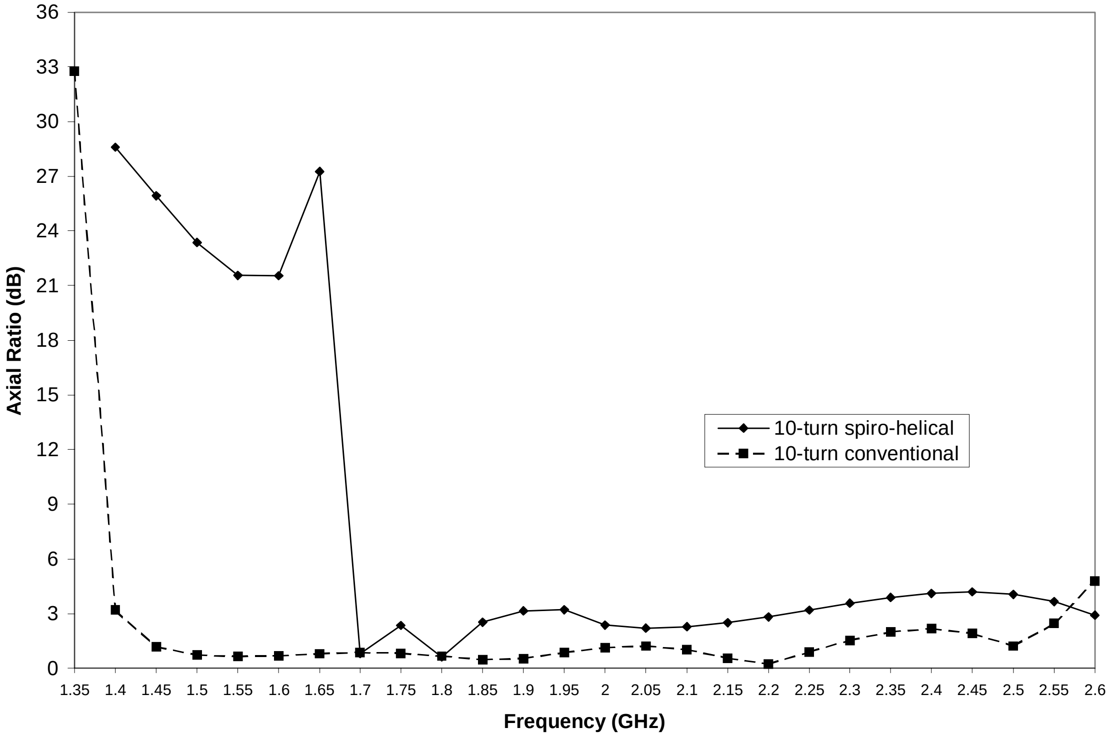

(b)

Figure 4.12 Comparison of (a) gain and (b) axial ratio characteristics for a 10-turn conventional helix with radius a = 24.37 mm and pitch angle $\alpha = 14°$ and a 10-turn spiro-helical antenna with $\alpha = 7°$, $\alpha' = 30°$, a = 16mm, and a' = 2mm.

5. Measurements of the Spiro-Helical Antenna

In order to ascertain the validity of predicted properties of spiro-helical antenna presented in Chapter 4, two models are chosen for construction and measurement. Far-field pattern measurements are taken over a wide range of frequencies for each of these antennas, using an outdoor range of the Virginia Tech Antenna Laboratory. Both antennas have the same number of turns, but differ in pitch angles and radii. From the collected data, far-field patterns, half-power beamwidth, sidelobe level, and back radiation level are obtained. In addition to the magnitudes of field components (E_θ and E_ϕ), their phases are also provided as part of the measured data. The phase data, however, were not found to be useful and thus will not be used.

5.1 Construction of Spiro-helical Antenna

Construction of the spiro-helical antenna is carried out in three steps. First, the conducting wire is prepared in a primary helical shape with pitch angle α' and radius a'. In the second step, the spiral wire is carefully wrapped on a cylindrical surface of radius a. The spiral on this cylinder assumes the shape of a helix with a pitch angle α. The antenna is then mounted on a ground plane.

The antennas were built using 0.4mm and 0.6mm diameter steel wire found at a local hardware store. This wire is flexible enough so that it can be easily bent to conform to a spiral shape, but also strong enough so that it can maintain the assumed shapes. In order to create the spiral-shaped wire (primary helix), several dowels with varying diameters were used. These dowels were marked for different pitch angles α' (30° and 40°), then the wire was wrapped around the dowel to create the spiral shape at those angles (essentially, a helix with a pitch angle α'). This process continued until there was enough length of the primary helix to create a 10-turn spiro-helical antenna.

Once the proper length of the spiral wire is prepared, the final stage of the construction can begin. Using a square ground plane for the representative case and a circular ground plane for a second prototype antenna with the diameter of the ground plane in each case being at least $\frac{\lambda}{2}$ at the lowest frequency, a cylindrical frame is connected to help hold the antenna in place. This frame is built using thin cardboard wound to the desired outer radius a. After the cylinder has been connected to the ground plane, the spiral wire is attached to the frame in the form of a larger helix with pitch angle α. To facilitate this stage of the construction, the cardboard frame is marked to indicate where the wire must be attached so that the pitch angle α is maintained. The spiral wire is then attached to the cardboard cylinder and super glue is used to hold the antenna in place. Once the antenna is securely in place, a wire is soldered to the beginning section of the antenna for the feed line. This wire must not make any contact with the ground plane in order to avoid a short circuit. The antennas were fed at the back of the ground plane by a coaxial cable with the center conductor attached to the wire and the outer conductor attached to the ground plane. The antennas were then tested using the outdoor range of the Antenna Laboratory. Table 5.1 summarizes the parameters of each of antennas. Antenna 1 corresponds to the representative case.

Table 5-1 Specifications of Antennas Constructed for Experimental Analysis

Antenna	Parameters					
	N	α	α'	a	a'	r_o
Antenna 1	10	10°	30°	16mm	2mm	0.2mm
Antenna 2	10	12°	40°	16mm	3mm	0.3mm

The results for antenna 1 are presented in this chapter, while the computed and measured results for antenna 2 are given in Appendices B and C, respectively.

5.2 Measurement Results

5.2.1 Radiation Patterns

All measured radiation patterns, including the ones presented in Appendix C, are normalized to unity. Figures 5.1(a) through 5.1(p) illustrate normalized power patterns for antenna 1 at several frequencies. Measurements at frequencies below 1.5 GHz were not performed due to the limitation of the horn antenna used as the transmitter. Comparison of these patterns with those in Figure 4.6 at the corresponding frequencies indicate an overall good agreement. However, the measured patterns at frequencies above 2.15 GHz seem to be associated with higher-order modes. This behavior is due to the fact that the radii (a and a') of the fabricated antenna are slightly larger than those of the representative case studied in Chapter 4. Also, fabrication inaccuracies in pitch angles and reflections from objects in the measurement environment contribute to the deviations from predicted patterns. For 1.5 GHz $\leq f \leq$ 2.05 GHz, sidelobe and backlobe levels remain below 10 dB. In the 2.1 GHz – 2.15 GHz range, sharp increases in sidelobe level are observed. There, the main beam develops and axial null, indicating the excitation of higher-order modes.

5.2.2 Half-Power Beamwidth

Figure 5.2 (a) illustrates half-power beamwidth versus frequency for antenna 1. A comparison with the predicted half-power beamwidth is also made in this figure. The measured HPBW shows a gradual decrease with frequency in the 1.5 GHz to 2.15 GHz. This behavior, also observed in the predicted HPBW, is consistent with the variations of gain with frequency as seen in Figure 4.3. In fact, the HPBW data can be used to obtain a rough estimate of gain using the relationship $G = \dfrac{41{,}253}{\left(HPBW^{\circ}\right)^2}$. Figure 5.2 (b) shows the gain characteristics obtained from measured HPBW and compares it with the predicted gain for antenna 1. It is noted that the agreement is between the ‘measured’ and computed gain characteristics is good.

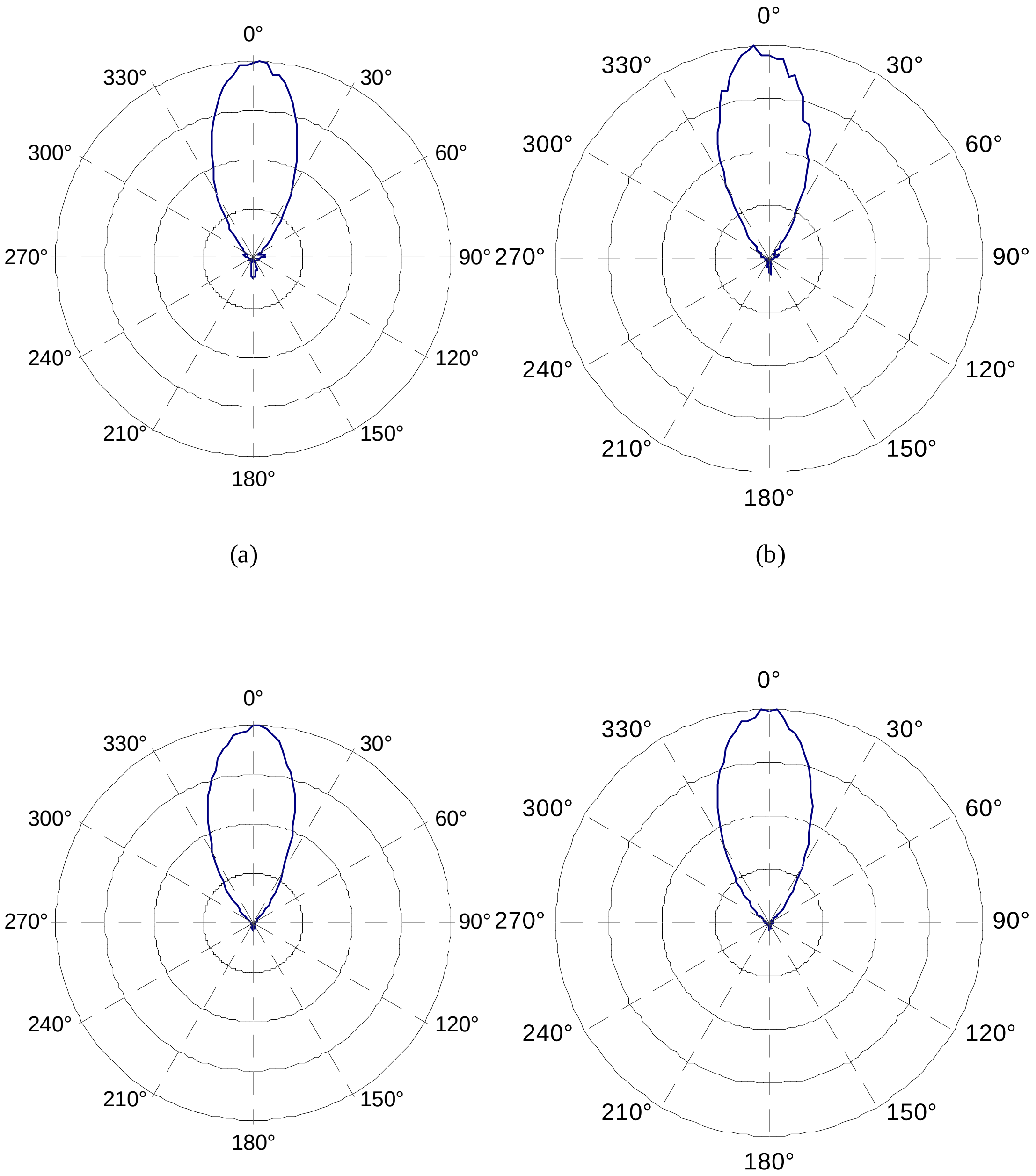

(a)

(b)

(c)

(d)

Figure 5.1 Measured power patterns for the representative case at (a) 1.5 GHz, (b) 1.55 GHz, (c) 1.6 GHz, and (d) 1.65 GHz.

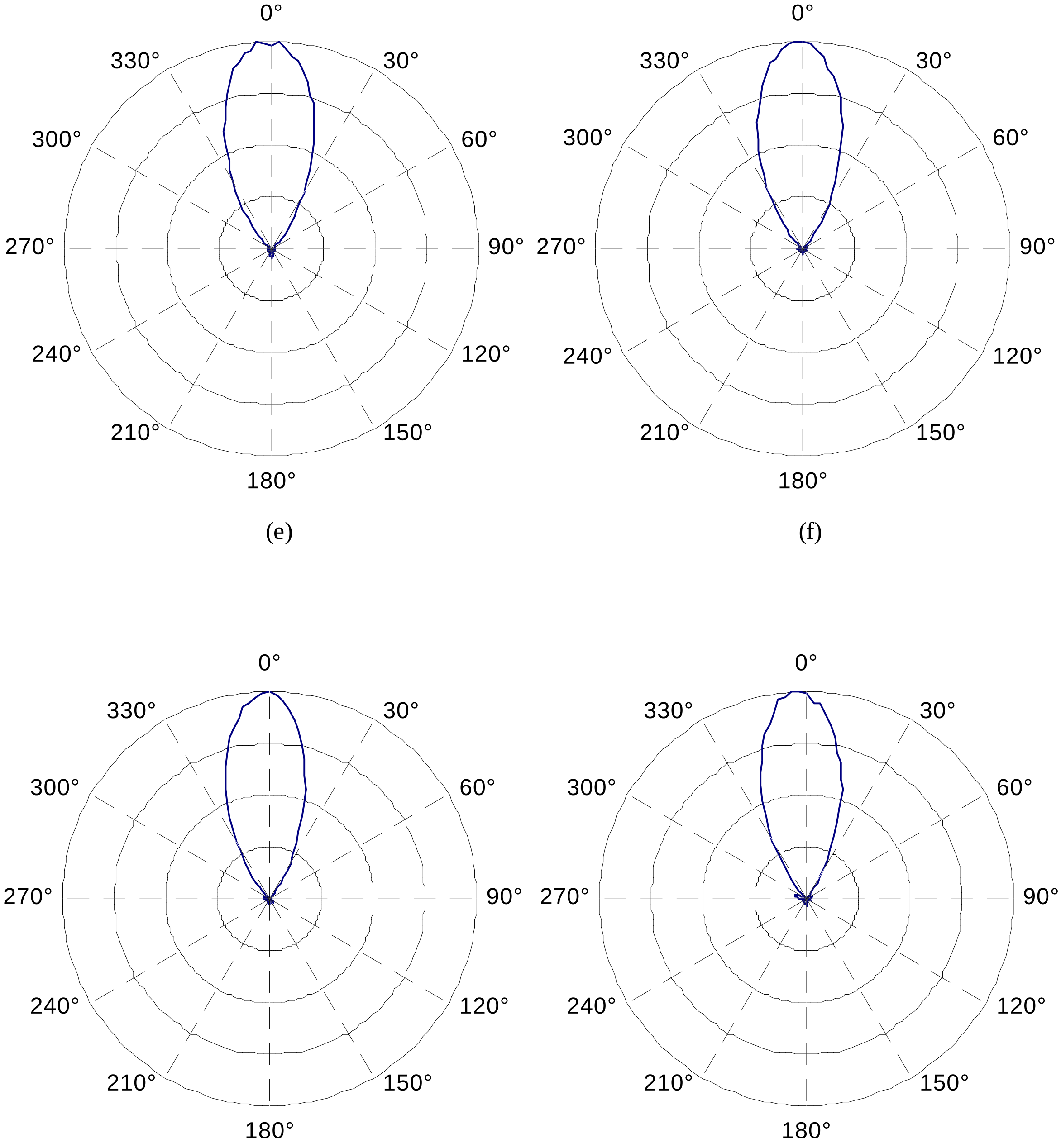

(e) (f) (g) (h)

Figure 5.1 Measured power patterns for the representative case at (e) 1.7 GHz, (f) 1.75 GHz, (g) 1.8 GHz, and (h) 1.85 GHz.

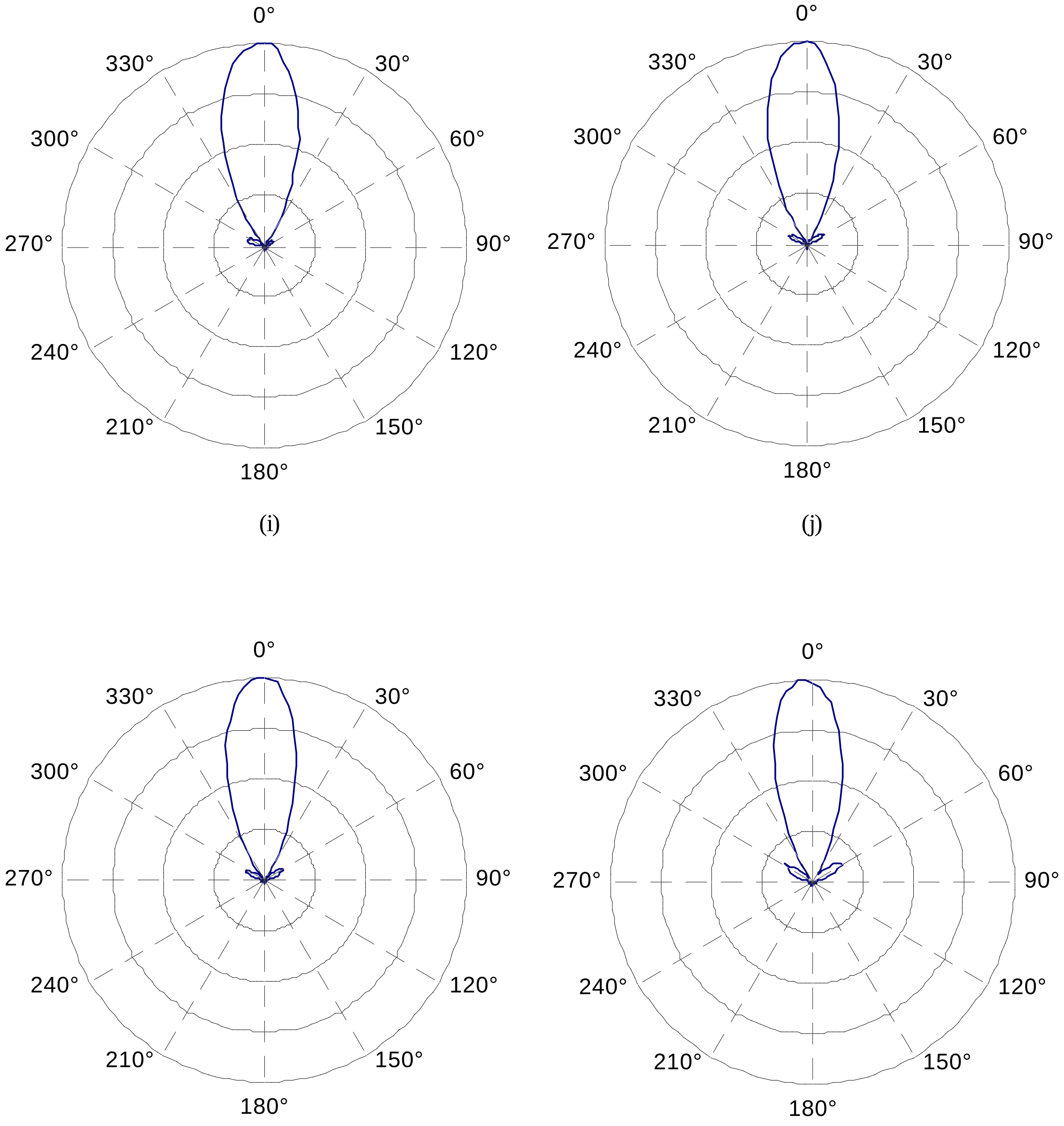

(i) (j)

(k) (l)

Figure 5.1 Measured power patterns for the representative case at (i) 1.9 GHz, (j) 1.95 GHz, (k) 2.0 GHz, and (l) 2.05 GHz.

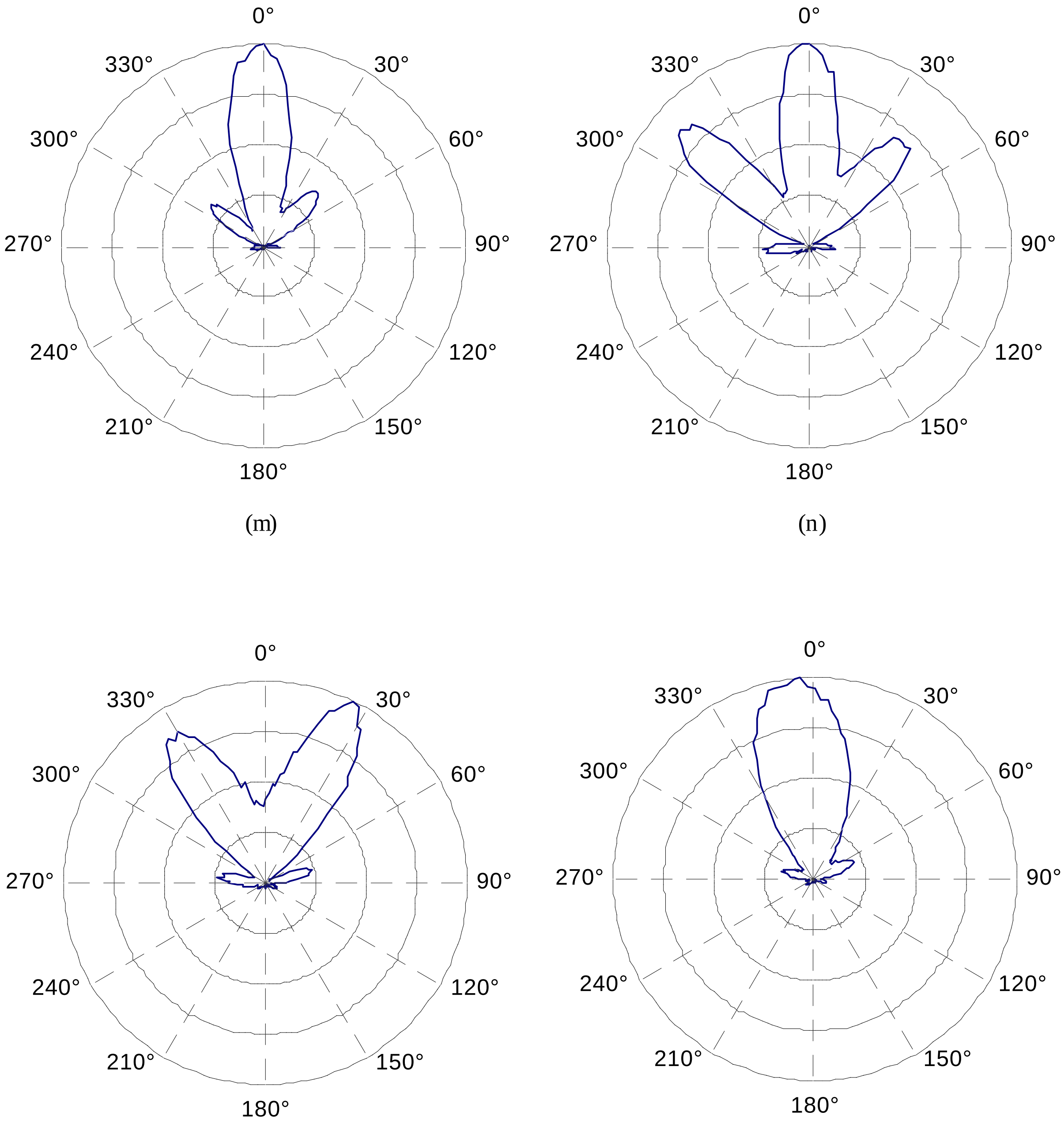

(m) (n)

(o) (p)

Figure 5.1 Measured power patterns for the representative case at (m) 2.1 GHz, (n) 2.15 GHz, (o) 2.2 GHz, and (p) 2.25 GHz.

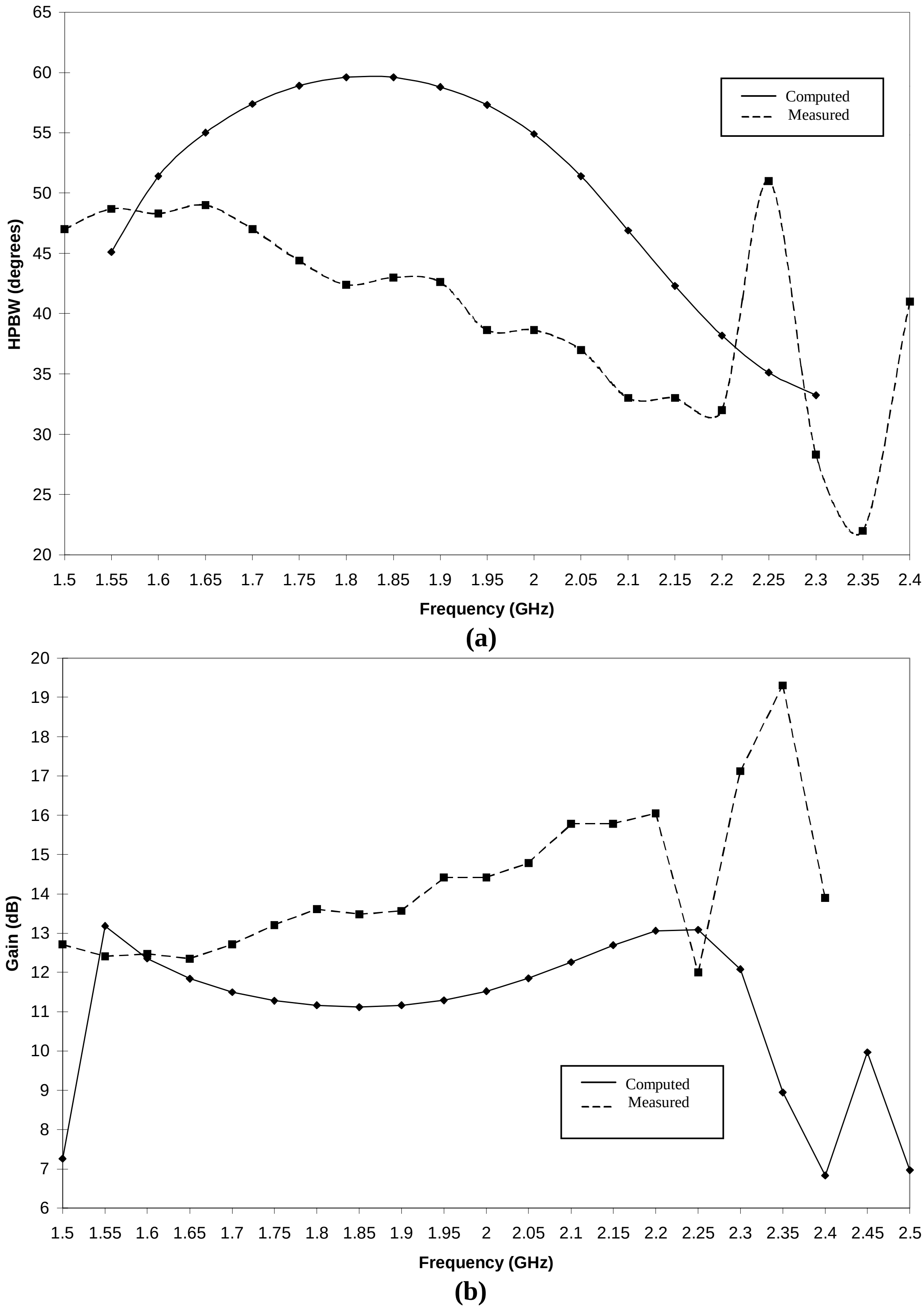

Figure 5.2 Variations of (a) half-power beamwidth and (b) gain versus frequency between measured and calculated data of a 10-turn spiro-helical antenna with $\alpha = 10°$, $\alpha' = 30°$, $a = 16$mm, and $a' = 2$mm.

6. Conclusions

A novel antenna that produces high gain and nearly circular polarization over a wide bandwidth and a broad beamwidth has been presented. This new antenna has radiation characteristics comparable to those of a conventional helix but occupies a much smaller volume. It is made of a primary helix shaped into a larger helix, thus a structure with two degrees of helicity. This antenna is named spiro-helical antenna. A comprehensive numerical analysis of spiro-helical antenna has been carried out using the method-of-moments software NEC-2. Far-field patterns, gain-frequency characteristics, and axial-ratio characteristics have been computed for numerous cases. The input impedance has also been examined, but the simulation results for the input impedance from NEC-2 require a more in-depth analysis. Several spiro-helical antennas were made and tested. Generally, the measured and computed far-field patterns are in good agreement. The reduced size of the proposed antenna by a factor of 2.5 to 3, compared to a conventional helix with about the same radiation properties, and its low fabrication cost, makes this antenna very attractive to mobile and satellite communications and aerospace applications.

6.1 Summary of Results

The important results of the investigation of spiro-helical antenna are summarized below:

- The spiro-helical antenna is capable of maintaining radiation characteristics of a conventional helical antenna while occupying a smaller volume. The volume of a spiro-helical antenna can be 2.5 to 3.21 times smaller than a conventional helix while preserving circular polarization and comparable gain and bandwidth.

- The peak gain occurs when the outer circumference $2\pi(a + 2a')$ is about 0.96λ. For a conventional helix of comparable gain, this peak occurs at a circumference of about 1.2λ.; Figures 4.8(a) and 4.9(a)

- High gains and wide axial-ratio based bandwidths are obtained when the pitch angle α is about 7 degrees or 10 to 12 degrees. The gain based bandwidth is generally larger than the axial-ratio based bandwidth. The maximum gain, however, occurs when $\alpha = 10°$; Figures 4.6(a) and 4.6(b).

- The gain and axial ratio do not vary significantly with the pitch angle α'. However, a maximum gain is achieved when $\alpha' = 30°$ and $\alpha = 10°$; Figures 4.7(a) and 4.7(b)

- The gain increases with the number of turns, but the overall bandwidth is reduced; Figure 4.5(a).

- Increasing the radius of the primary helix, a', lowers the frequency of peak gain, increases the value of peak gain, and reduces the bandwidth

6.2 Recommendations for Future Work

Due to the fact that this antenna has not been previously researched, there are still many opportunities to learn more about it. The following is a list of suggestions for future investigations of the spiro-helical antenna.

- **Different helical shape.** The conventional helical shape determines the shape of the spiro-helical investigated here, but the spiral wire can be used to create different overall geometries as well. The wire can be wound into a tapered helical antenna, a conical helical antenna, a spherical helical antenna, or any other number of designs. The tapered spiro-helical antenna is expected to offer wider bandwidths.

- **Cavity mount.** No variation in ground plane has been evaluated in this thesis. A cavity mounted spiro-helical antenna can be examined numerically and experimentally to further investigate the effect of this ground plane on radiation properties.

- **Gain and input impedance measurements.** The measurements conducted in this thesis were limited to far-field patterns only. Input impedance and gain measurements need to be performed to have a more realistic assessment of the performance of spiro-helical antenna and its practical applications.

References

1. J. D. Kraus, *Antennas*, 2nd ed., McGraw Hill: New York, 1988.

2. H. Nakano, J. Yamauchi, and Y. Samada, "Power Gain of Helical Antennas," *4th Internationl Conference on Antennas and Propagation*, April 1985, pp. 127-130.

3. U. R. Kraft and G. Monich, " Main-beam polarization properties of modified helical antennas," *IEEE Trans. Antennas Popagat*. Vol. AP-38, 1990, pp. 589-592.

4. T. E. Tice and J. D. Kraus, "The influence of conductor size on the properties of helical beam antennas," *Proc. Inst. Elec. Eng.*, November 1949, p. 1296.

5. H. E. King and J. L. Wong, "Characteristics of 1 to 8 wavelength uniform helical antennas," *IEEE Trans. Antennas Propagat.*, vol. AP-28, 1980, pp. 291-296.

6. J. L. Wong and H. E. King, "Empirical helix antenna design," *Proc. IEEE antenna Propagat. Int. Symp.*, 1982, pp. 366-368.

7. R. M. Barts , W. L. Stutzman, " A Reduced Size Helical Antenna," *Proc. IEEE Antennas and Propagat. Soc. Int. Symp.*, vol. 3, pp. 1588-1591.

8. C. A. Balanis, *Antenna Theory: Analysis and Design*, 2nd ed., John Wiley and Sons: New York, 1997.

9. W. L. Stutzman and G. A. Thiele, *Antenna Theory and Design*, John Wiley and Sons: New York, 1981.

10. A. W. Rudge, K. Milne, A. D. Olver, P. Knight, *The Handbook of Antenna Design: Volume I*, Peter Peregrinus Ltd.: London, 1982.

11. T. A. Milligan, *Modern Antenna Design*, McGraw Hill: New York, 1985.

12. N. D. Fox, "A detailed analysis of the helical array as a high performance portable ground station antenna," Master's Thesis, Virginia Tech, 1988.

13. O. J. Glasser and J. D. Kraus, "Measured Impedances of Helical Antennas," *J. App. Phys.*, vol. 19, February 1948, pp. 193-197.

14. L. V. Blake, *Antennas*, John Wiley and Sons: New York, 1966.

15. J. A. Marsh, "Measured Current Distributions on Helical Antennas," *IRE Proc.*, vol. 39, June 1951, pp.668-675.

16. J.C. Cardoso, "The Spherical Helical Antenna," Master's Thesis, Virginia Tech, 1992.

17. J. C. Cardoso, A. Safaai-Jazi, "Spherical Helical Antenna with Circular Polarization Over a Broad Beam," *Electronics Letters*, vol. 29, February 18, 1993, pp. 325-326.

18. A. Safaai-Jazi, J. C. Cardoso, "Radiation Characteristics of a Spherical Helical Antenna," *IEE Proc.-Microw. Antennas Propag.*, vol. 143, February 1996, pp. 7-11.

19. H. Nakano, *Helical and Spiral Antennas – A Numerical Approach*, Research Stufies Press: New York, 1987.

20. G. J. Burke, A. J. Poggio, *Numerical Electromagnetics Code (NEC) – Method of Moments, Part III: User's Guide*, UCID 18834, Lawrence Livermore Laboratory, January 1981. `http://www.ntis.gov`

21. G. J. Burke, A. J. Poggio, *Numerical Electromagnetics Code (NEC) – Method of Moments, Part II: Program Description – Code*, UCID 18834, Lawrence Livermore Laboratory, January 1981 `http://www.ntis.gov`

Appendix A. MATLAB Code for Helical and Spiro-Helical Models

The Matlab source code is presented which was used to create the input files for NEC-2. This appendix contains two listings. Listing A.1 was used to create the geometry for conventional helices. Listing A.2 was used to create the geometry for all the spiro-helical simulations. In each case, the pitch angles and radii along with the number of turns and frequency range could be changed by editing the listings provided.

In addition to the geometry, commands which would be used by NEC-2 had to be included. The NEC manual [21] gives a further explanation of how to use each of these commands as well as the specifics regarding the input files.

A.1 Listing for helical model

```
clear all;

a = .022857;            %% Radius a
alpha = 12*pi/180;      %% Pitch angle
sym = 't';
t = '15';
N = 15;
inc = .3;
begin = 1000;           %% beginning frequency
last = 2500;            %% ending frequency


l = 'k';
rad = .0005;
dist = 50;              %% increment for frequency range


for freq = begin:dist:last,

   c = 1;
   lam = .02*(3*10^8/(freq*10^6));
   f = num2str( freq/10 );

   rad1 = num2str ( a );
   pitch1 = num2str ( alpha*180/pi );
   radius = num2str ( rad );

   filename = strcat( t, sym , f, pitch1, '.dat' );
   fid = fopen(filename , 'w');

   text1 = strcat( 'CMa=',rad1,',alpha=',pitch1,',radius=',radius);
   text2 = strcat( 'CE',t,'h', sym , pitch1,'.csv');

   fprintf(fid, text1 );
   fprintf(fid, '\r');
   fprintf(fid, '\n');

   fprintf(fid, text2 );
   fprintf(fid, '\r');

   x1(1) = 0;
   y1(1) = 0;
   z1(1) = lam;

   fprintf(fid, '\nGW%3d 2
%10.4f%10.4f%10.4f%10.4f%10.4f%10.4f%9.4f\r',c,x1(c),y1(c),y1(c),x1(c),
y1(c),z1(c),rad);

   c= 1;

   for phi = 1:inc:2*pi*(N+1),

      x2 = x1(c);
```

```
      y2 = y1(c);
      z2 = z1(c);

      c= c+1;

      x1(c)=a*cos(phi);
      y1(c)=a*sin(phi);
      z1(c)=a*tan(alpha)*phi;

      fprintf(fid, '\nGW%3d 1
%10.4f%10.4f%10.4f%10.4f%10.4f%10.4f%9.4f\r',c,x2,y2,z2,x1(c),y1(c),z1(
c),rad);


   end

   fprintf(fid,'\nGE\r');

   fprintf(fid,'\nGN  1\r');
   fprintf(fid,'\nFR  0    1    0    0%10.1f     0.000\r', freq);
   fprintf(fid,'\nEX  0    1    1   10     5.000     0.000\r');
   fprintf(fid,'\nRP  0   37   37 1010     0.000     0.000     5.000
10.000\r');
   fprintf(fid,'\nEN');

   fclose(fid);

end
```

A.2 Listing for Spiro-helical model

```
clear all;
a = 16;                             %% Radius a
ap = 3;                             %% Radius a prime
alph = 10*pi/180;                   %% Set angle for alpha
alpha = 30*pi/180;                  %% Set angle for alpha prime
length = 220;                       %% Length for number of turns

sym = '_';                          %% Symbol to distinguish simulation
t = '10';                           %% Used in filename for number of turns
inc = .3;                           %% Increment for length
begin = 1500;                       %% Beginning frequency
last = 2500;                        %% Ending frequency

l = 'k';                            %% Color for Plot
rad = .0005;                        %% radius of conducting wire
intrvl = 50;                        %% Frequency interval


for freq = begin:intrvl:last,

   c = 1;
   lam = .02*(3*10^8/(freq*10^6));  %% .02 times lambda

   f = num2str( freq/10 );          %% Simulation information
   rad1 = num2str ( a );
   rad2 = num2str ( ap );
   pitch1 = num2str ( alph*180/pi );
   pitch2 = num2str ( alpha*180/pi );
   radius = num2str ( rad );

   filename = strcat( t, sym , f, pitch1, '.dat' );
   fid = fopen(filename , 'w');

   text1 = strcat(
'CMa=',rad1,',ap=',rad2,',alpha=',pitch1,',alphap=',pitch2,',radius=',r
adius);
   text2 = strcat( 'CE',t, sym , pitch1,'.csv');

   fprintf(fid, text1 );
   fprintf(fid, '\r');
   fprintf(fid, '\n');

   fprintf(fid, text2 );
   fprintf(fid, '\r');

   x1(1) = 0;                          %% Initial values for x,y, and z
   y1(1) = 0;
   z1(1) = lam;

   fprintf(fid, '\nGW%3d 2
%10.4f%10.4f%10.4f%10.4f%10.4f%10.4f%9.4f\r',c,x1(c),y1(c),y1(c),x1(c),
y1(c),z1(c),rad);

   for zo = 2.7:inc:length,
```

```
      tmp = zo;

      x2 = x1(c);
      y2 = y1(c);
      z2 = z1(c);

      c= c+1;                       %% Increase counter for array

      phi = tmp./((a+ap) * tan(alph));    %% Calculation of Phi
                                          %% Calculation of Phi prime
      phip = tmp./(ap * sin(alph) * tan(alpha));

      x1(c) = ((a+ap).*cos(phi) + ap.*cos(phi).*cos(phip) -
ap*sin(alph).*sin(phi).*sin(phip))/1000;
      y1(c) = ((a+ap).*sin(phi) + ap.*sin(phi).*cos(phip) +
ap*sin(alph).*cos(phi).*sin(phip))/1000;
      z1(c) = ((a+ap)*tan(alph).*phi - ap*cos(alph).*sin(phip))/1000;

                                   %% x, y, and z written in input file
      fprintf(fid, '\nGW%3d 1
%10.4f%10.4f%10.4f%10.4f%10.4f%10.4f%9.4f\r',c,x2,y2,z2,x1(c),y1(c),z1(
c),rad);

   end
                  %% End geometry and parameters for ground plane,
                  %% frequency, excitation, and radiation plots.
   fprintf(fid,'\nGE\r');
   fprintf(fid,'\nGN  1\r');
   fprintf(fid,'\nFR  0    1    0    0%10.1f     0.000\r', freq);
   fprintf(fid,'\nEX  0    1    1   10     5.000     0.000\r');
   fprintf(fid,'\nRP  0   37   37 1010     0.000     0.000     5.000
10.000\r');
   fprintf(fid,'\nEN');

   fclose(fid);

end

figure(1)         %% check graph of geometry to ensure number of turns
plot3(x1,y1,z1,l)
view(90,0)
```

Appendix B. Numerical Far-Field Patterns of Spiro-Helical Antenna

The far-field radiation patterns of spiro-helical antenna 2 from Chapter 5 are contained in this appendix. The antenna was simulated from 1.5 GHz to 2.5 GHz. Data for the gain, axial ratio and impedance are displayed for $\theta \leq 20°$. The radiation patterns are of the *x*-*z* plane, since the antenna is essentially symmetrical about the *z*-axis. The patterns have been normalized to unity.

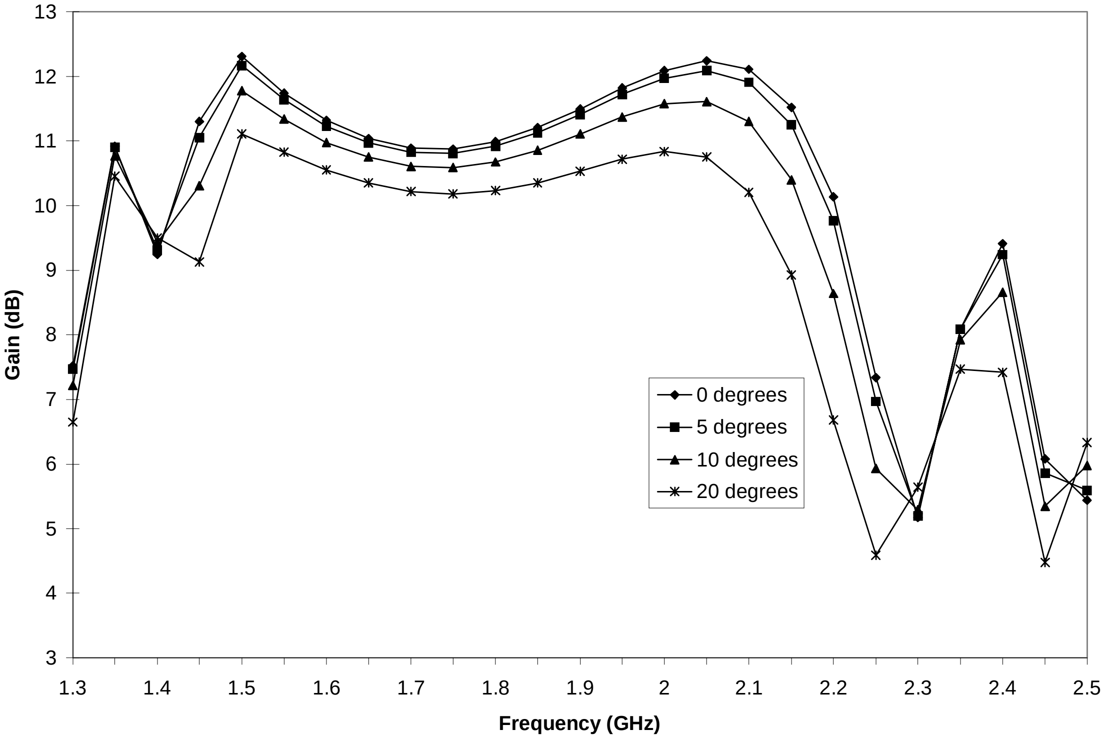

(a)

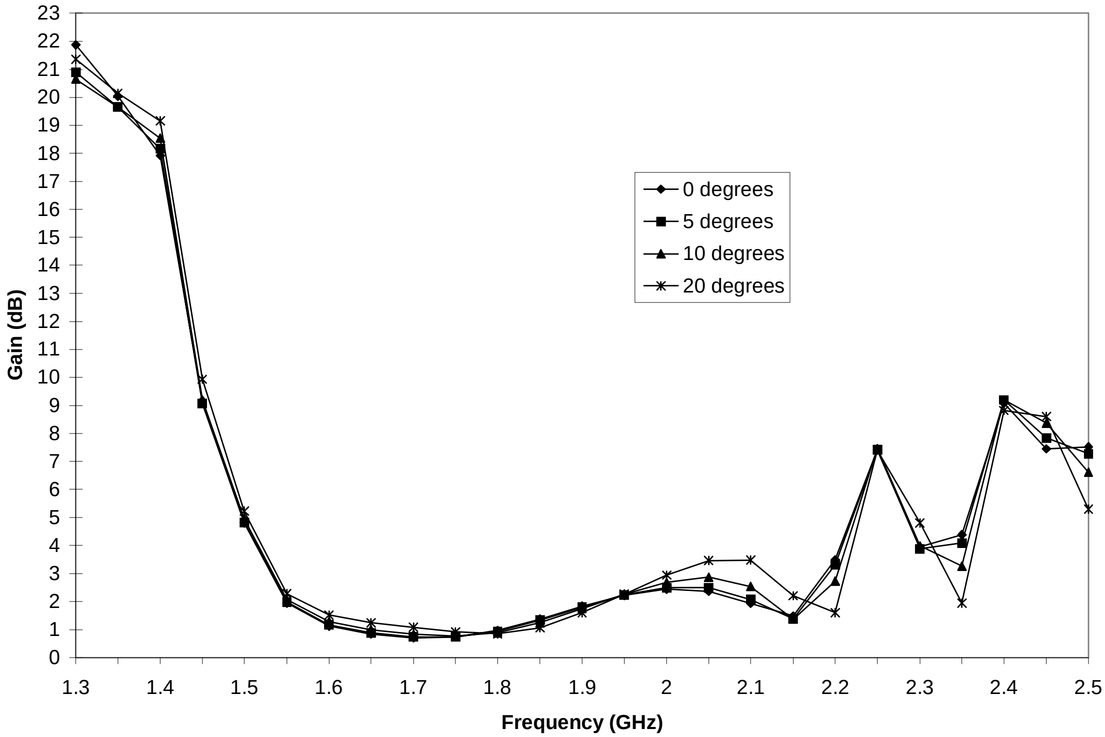

(b)

Figure B.1 Variations of (a)gain and (b)axial ratio versus frequency for several values of θ for a 10-turn spiro-helical antenna with $\alpha = 12°$, $\alpha' = 40°$, $a = 16$mm, $a' = 3$mm, and $r_o = 0.3$mm. (Antenna 2)

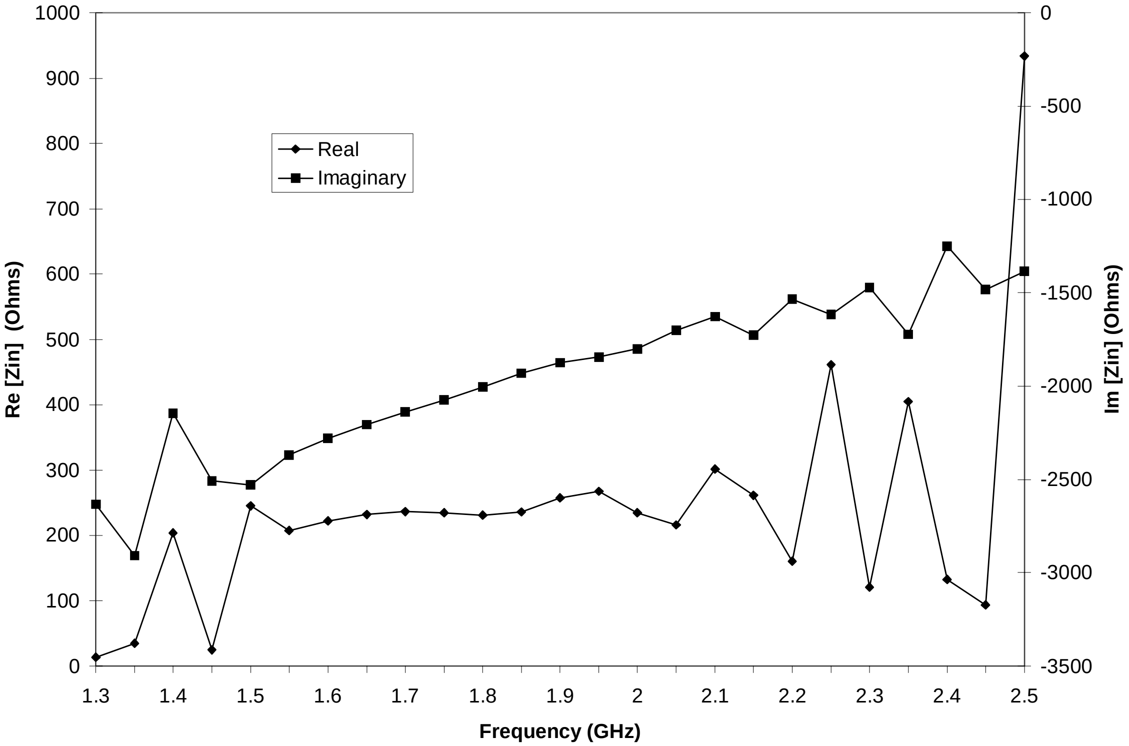

Figure B.2 Variations of impedance versus frequency for a 10-turn spiro-helical antenna with $\alpha = 12°$, $\alpha' = 40°$, $a = 16$mm, $a' = 3$mm, and $r_o = 0.3$mm. (Antenna 2)

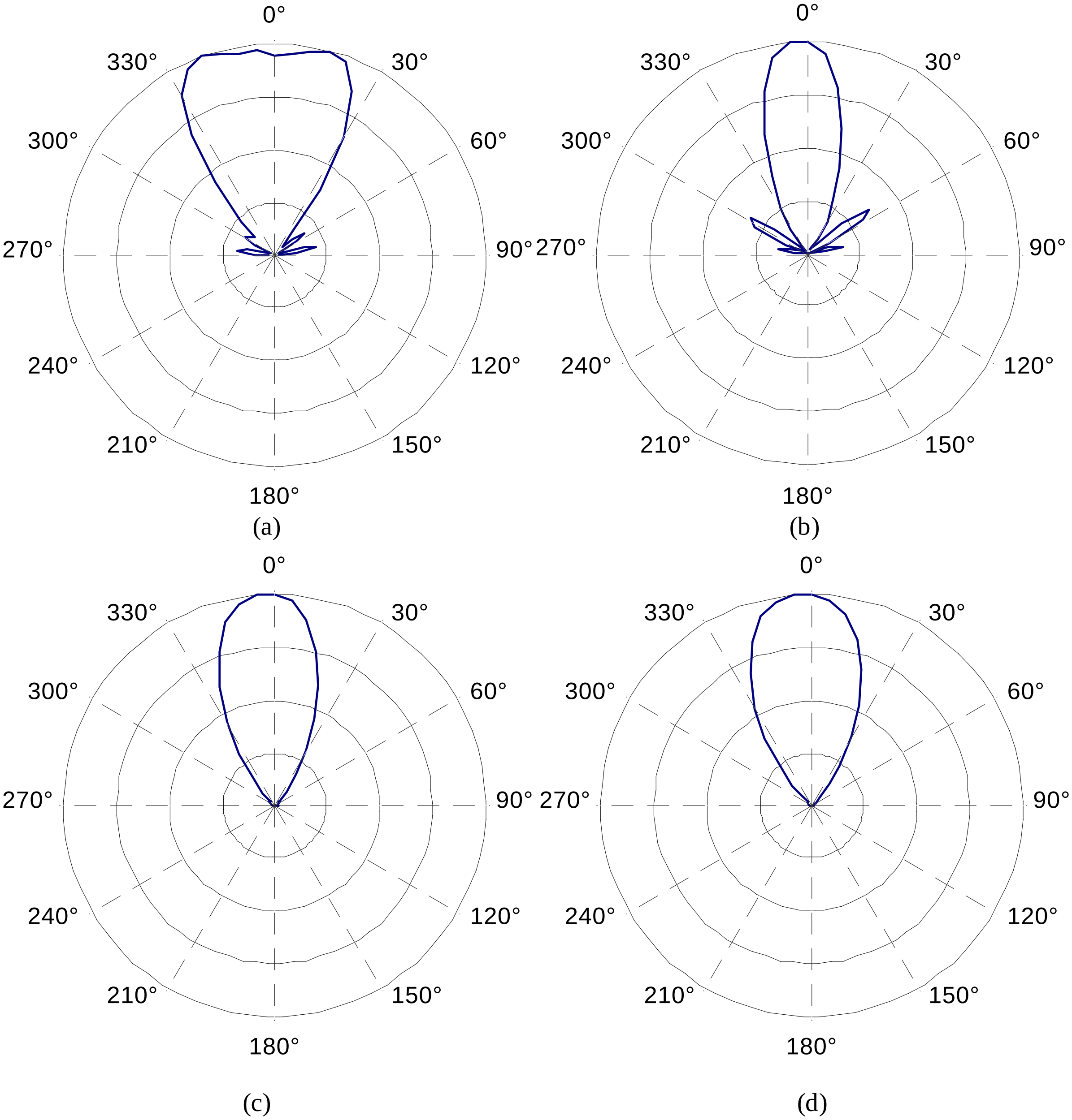

(a) (b)

(c) (d)

Figure B.3 Computed power patterns for Antenna 2 at (a) 1.4 GHz (b) 1.45 GHz, (c) 1.5 GHz, and (d) 1.55 GHz.

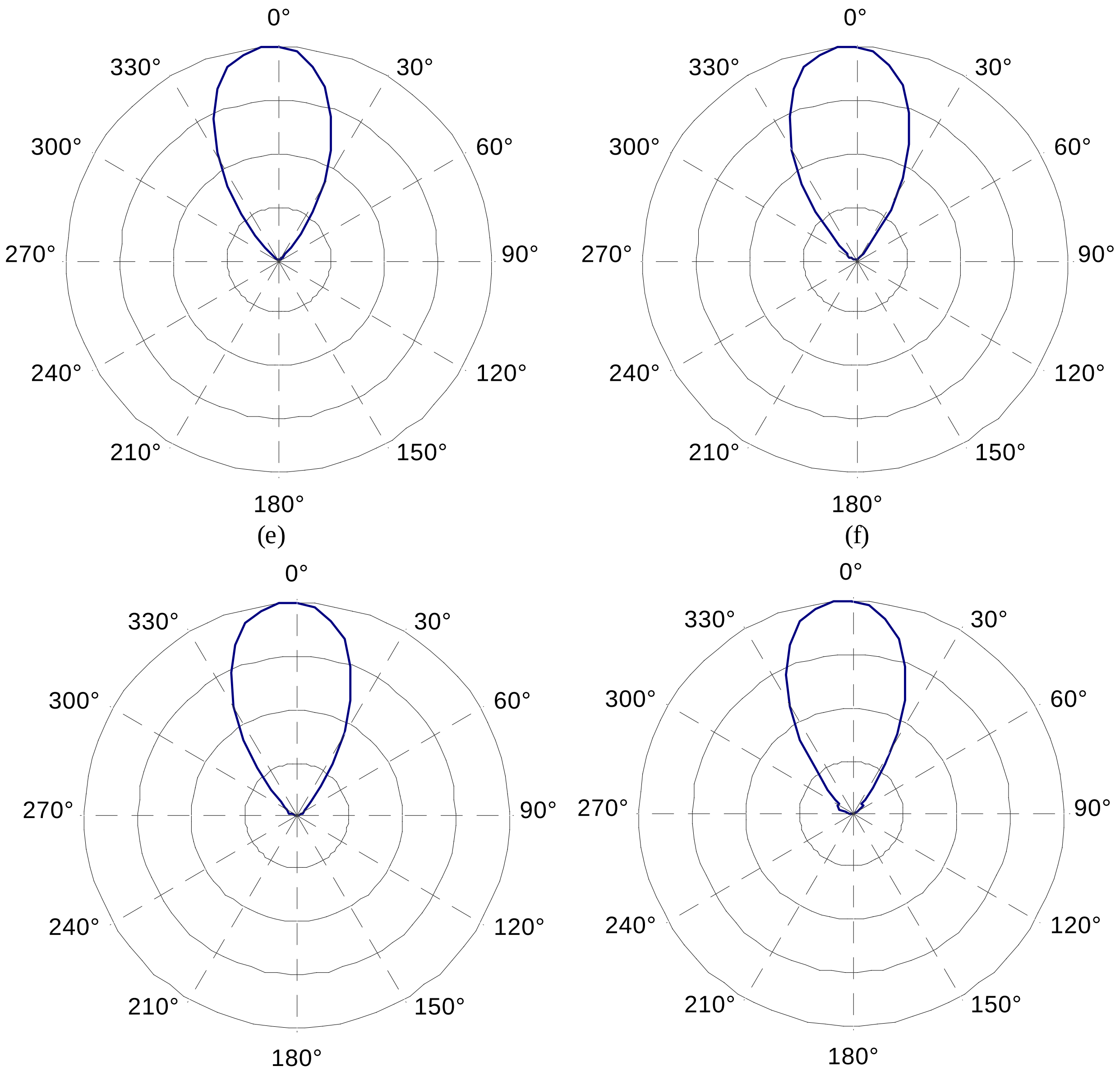

(e) (f)

(g) (h)

Figure B.3 Computed power patterns for Antenna 2 at
(e) 1.6 GHz (f) 1.65 GHz, (g) 1.7 GHz, and (h) 1.75 GHz.

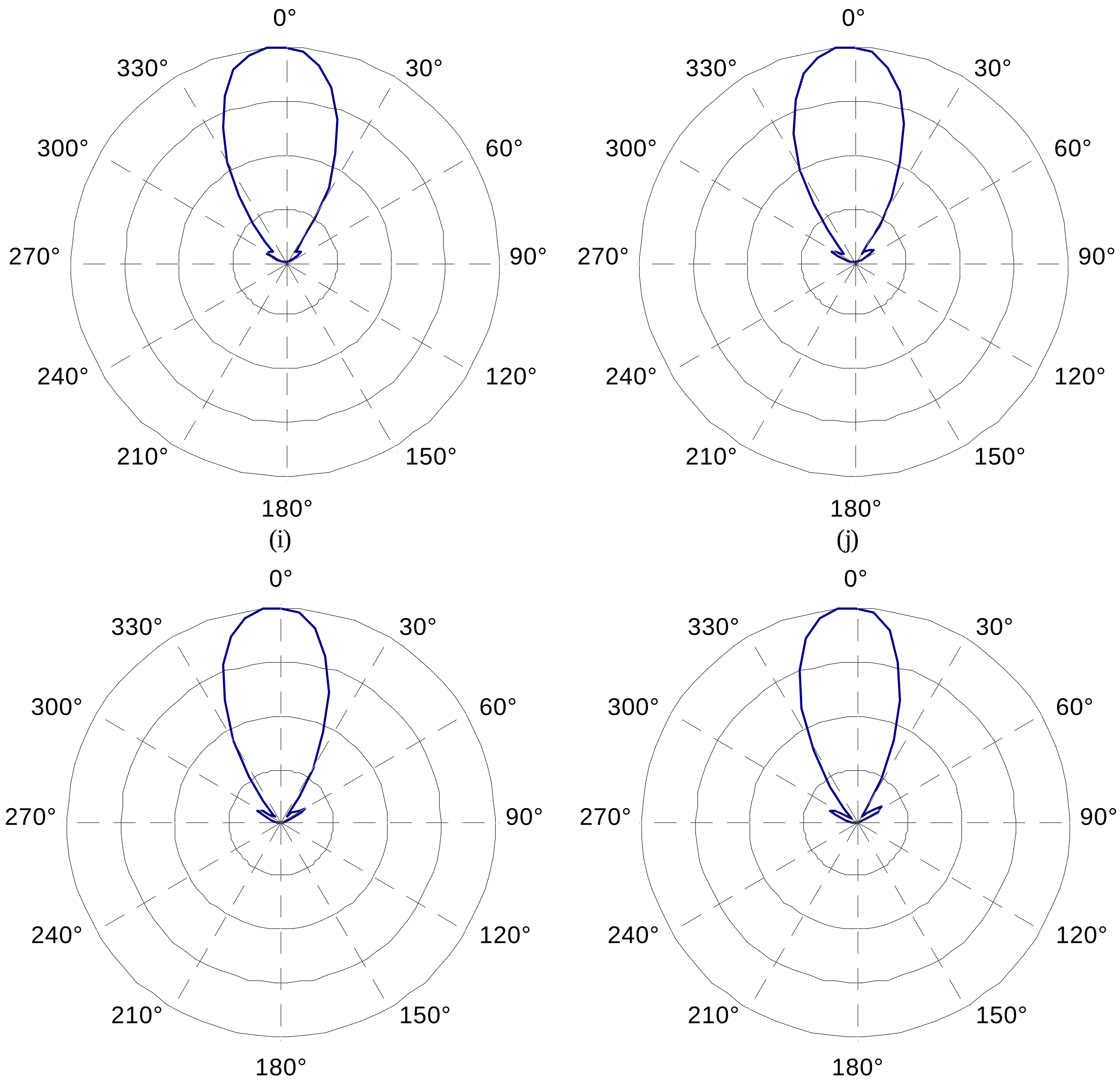

(k) (l)

Figure B.3 Computed power patterns for Antenna 2 at (i) 1.8 GHz (j) 1.85 GHz, (k) 1.9 GHz, and (l) 1.95 GHz.

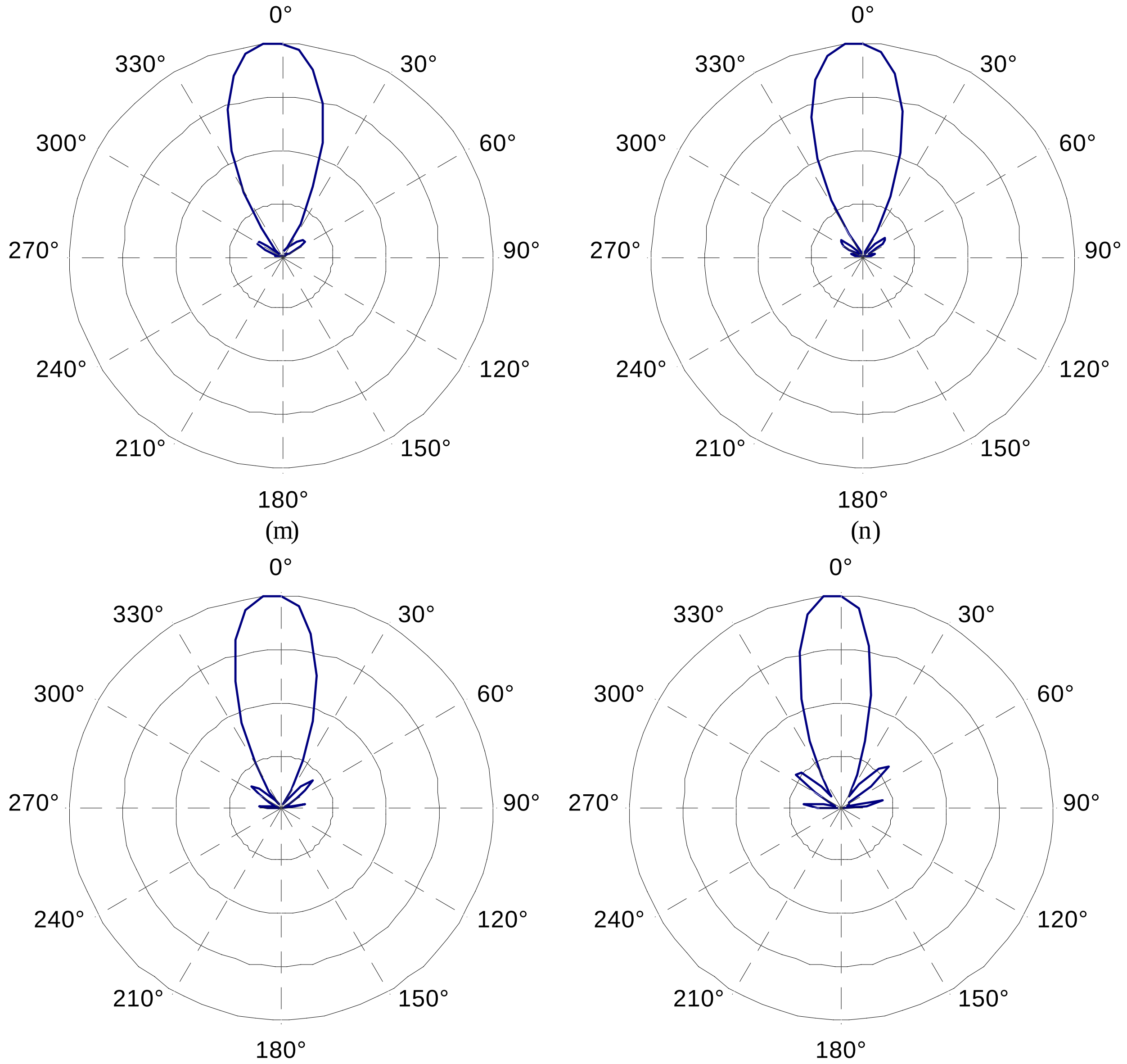

(m) (n) (o) (p)

Figure B.3 Computed power patterns for Antenna 2 at
(m) 2.0 GHz (n) 2.05 GHz, (o) 2.1 GHz, and (p) 2.15 GHz.

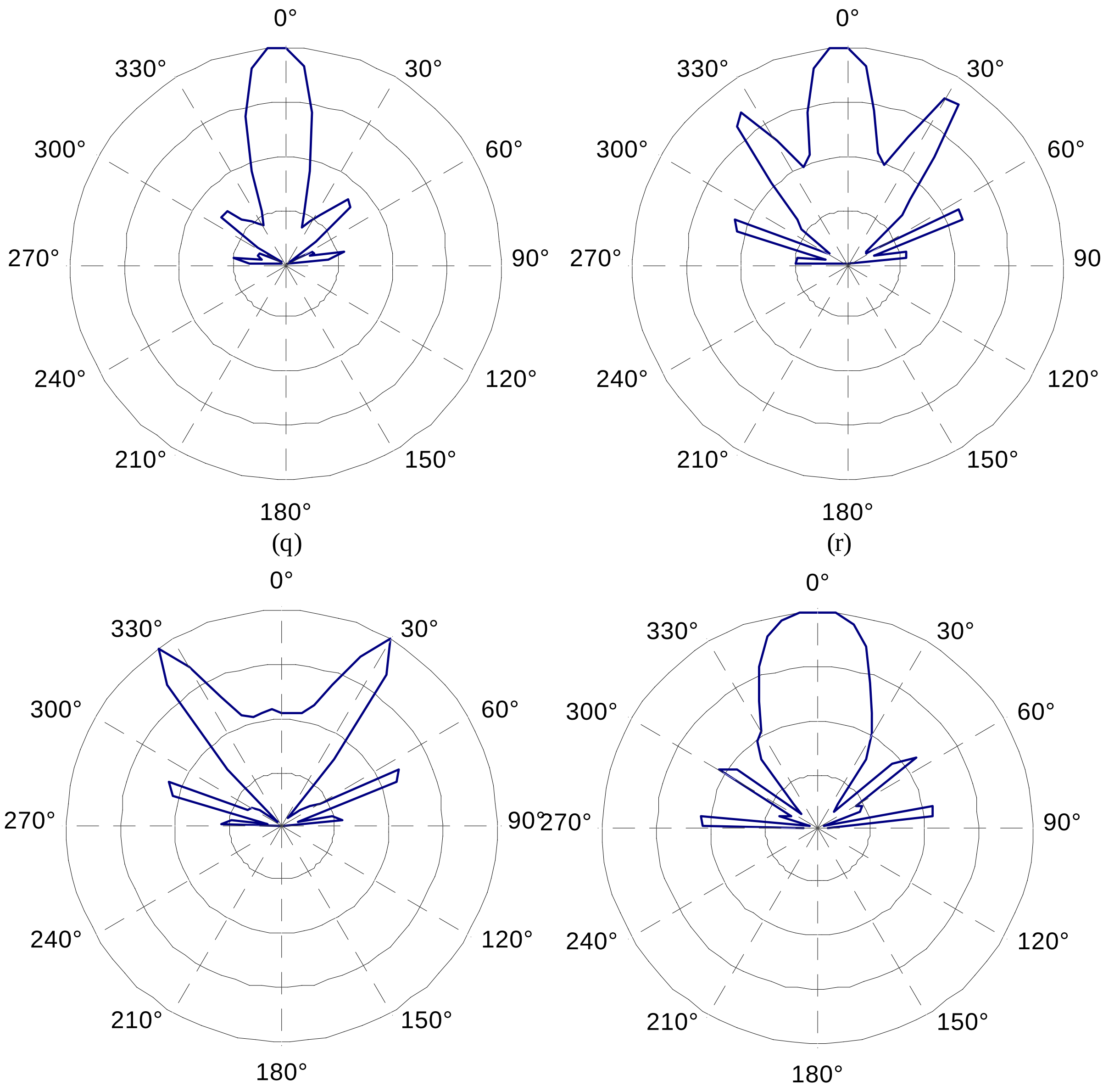

(q) (r)

(s) (t)

Figure B.3 Computed power patterns for Antenna 2 at
(q) 2.2 GHz (r) 2.25 GHz, (s) 2.3 GHz, and (t) 2.35 GHz.

Appendix C. Numerical Far-Field Patterns of Spiro-Helical Antenna

Far-field measurements are presented for spiro-helical antenna 2 from Chapter 5 corresponding to the numerical results from appendix B. The measurements were taken at 1.5 GHz to 2.25 GHz and plotted in the *x*-*z* plane. Results indicated agreement in the lower frequencies between the measured results and the numerical results from the previous appendix.

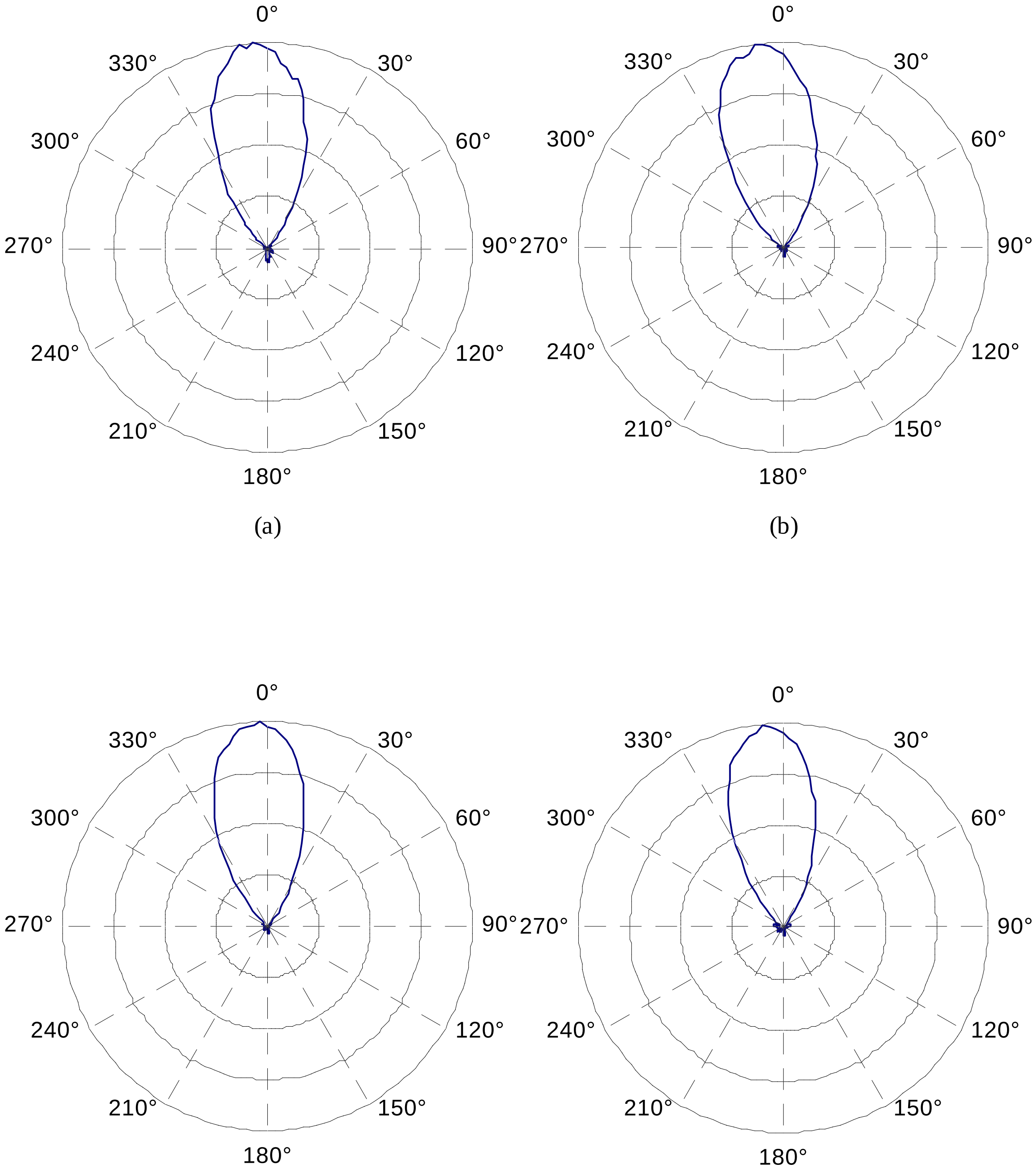

(a)

(b)

(c)

(d)

Figure C.1 Measured power patterns for Antenna 2 at (a) 1.5 GHz, (b) 1.55 GHz, (c) 1.6 GHz, and (d) 1.65 GHz.

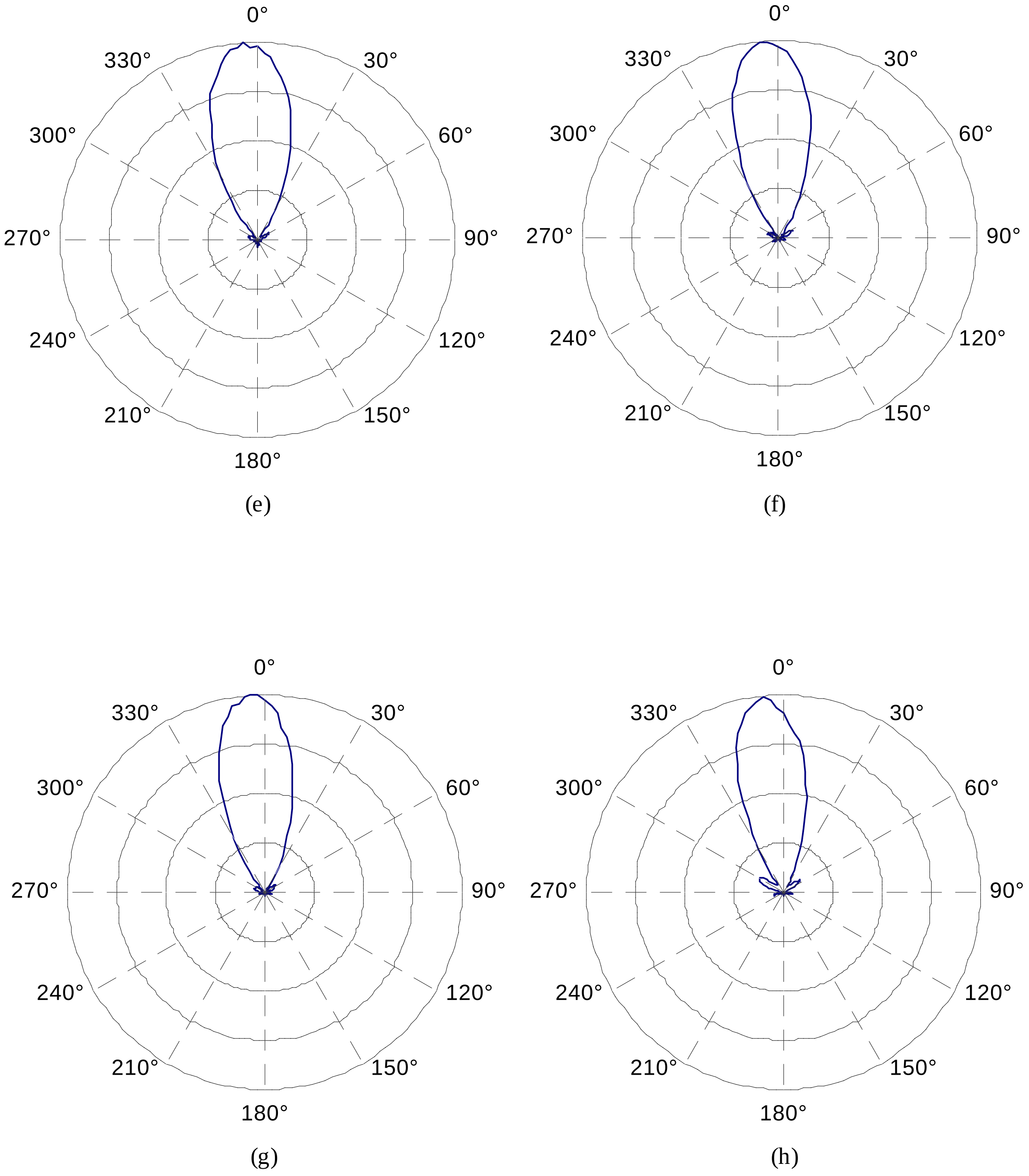

(e) (f) (g) (h)

Figure C.1 Measured power patterns for Antenna 2 at (e) 1.7 GHz, (f) 1.75 GHz, (g) 1.8 GHz, and (h) 1.85 GHz.

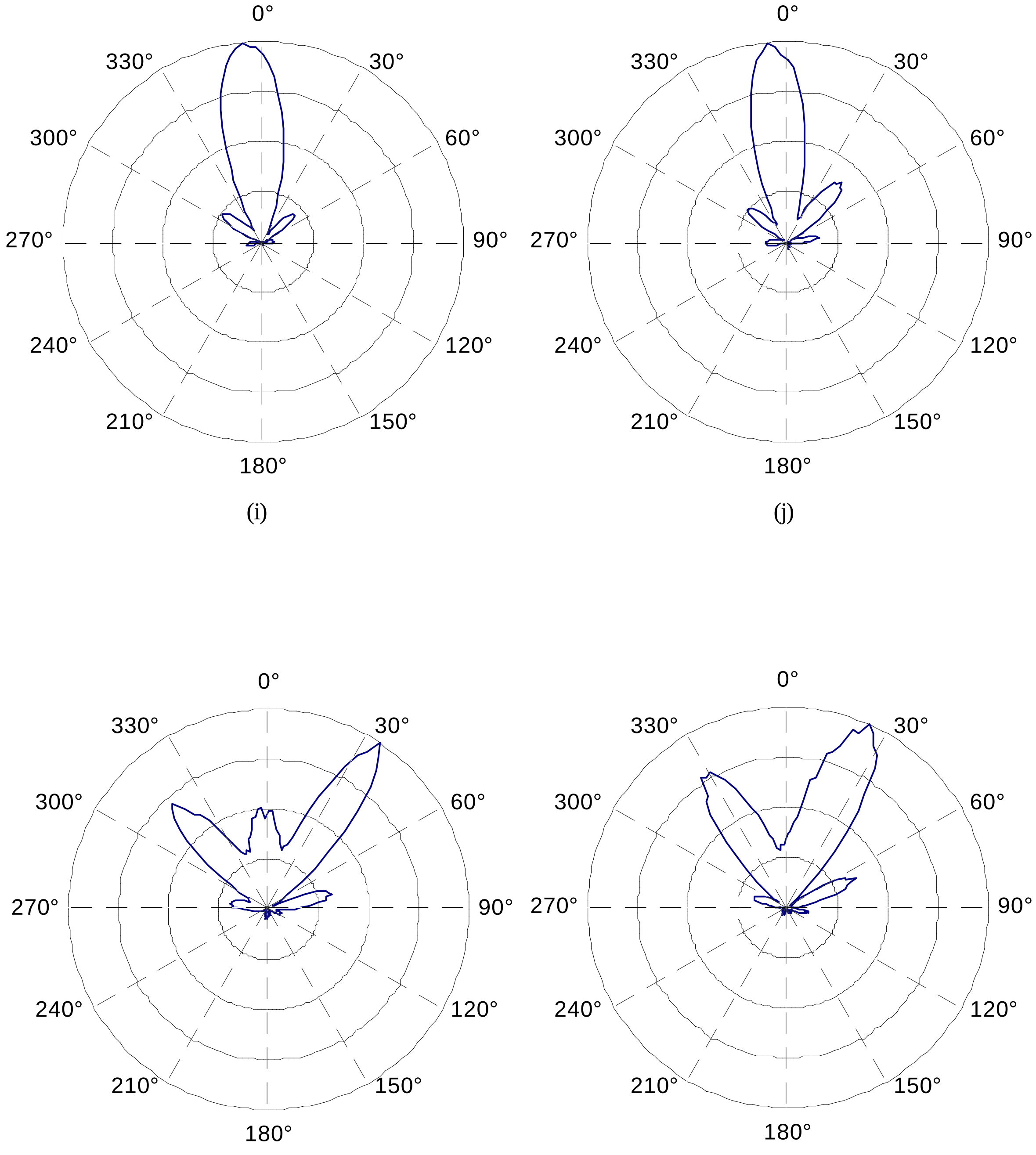

(i)

(j)

(k)

(l)

Figure C.1 Measured power patterns for Antenna 2 at
(i) 1.9 GHz, (j) 1.95 GHz, (k) 2.0 GHz, and (l) 2.05 GHz.

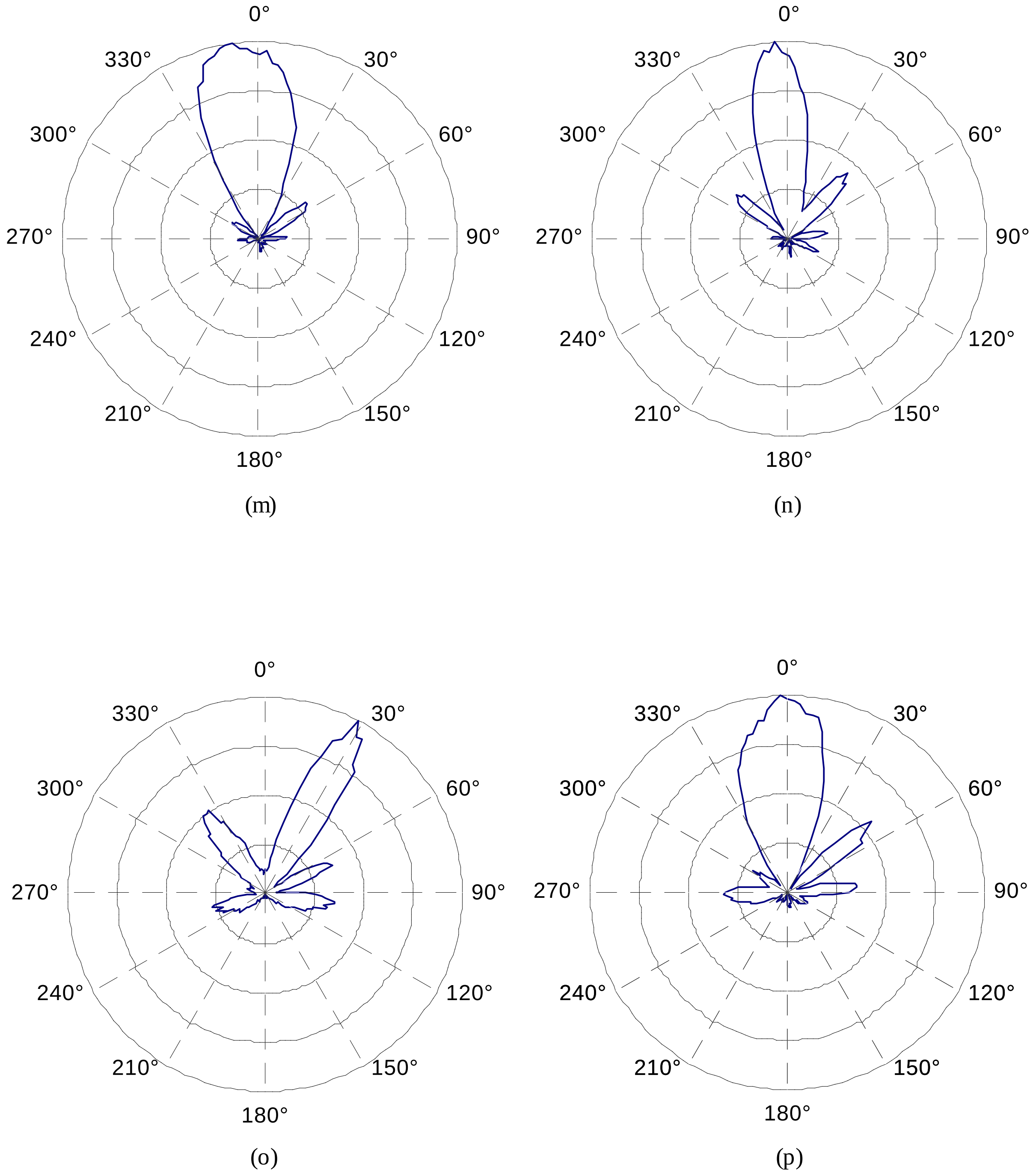

(m) (n)

(o) (p)

Figure C.1 Measured power patterns for Antenna 2 at (m) 2.1 GHz, (n) 2.15 GHz, (o) 2.2 GHz, and (p) 2.25 GHz.

Vita

Idine Ghoreishian was born to Ali and Parvin on April 28, 1975 in Tehran, Iran. He graduated from Frank W. Cox High School, Virginia Beach, Virginia in 1993 and attended Virginia Polytechnic Institute and State University, where he received his Bachelor of Science in electrical engineering in May 1997. In August of 1997, he began work on his Master of Science which he received in August of 1999.

射频和天线设计培训课程推荐

易迪拓培训(www.edatop.com)由数名来自于研发第一线的资深工程师发起成立，致力并专注于微波、射频、天线设计研发人才的培养；我们于 2006 年整合合并微波 EDA 网(www.mweda.com)，现已发展成为国内最大的微波射频和天线设计人才培养基地，成功推出多套微波射频以及天线设计经典培训课程和 ADS、HFSS 等专业软件使用培训课程，广受客户好评；并先后与人民邮电出版社、电子工业出版社合作出版了多本专业图书，帮助数万名工程师提升了专业技术能力。客户遍布中兴通讯、研通高频、埃威航电、国人通信等多家国内知名公司，以及台湾工业技术研究院、永业科技、全一电子等多家台湾地区企业。

易迪拓培训课程列表：http://www.edatop.com/peixun/rfe/129.html

射频工程师养成培训课程套装

该套装精选了射频专业基础培训课程、射频仿真设计培训课程和射频电路测量培训课程三个类别共 30 门视频培训课程和 3 本图书教材；旨在引领学员全面学习一个射频工程师需要熟悉、理解和掌握的专业知识和研发设计能力。通过套装的学习，能够让学员完全达到和胜任一个合格的射频工程师的要求…

课程网址：http://www.edatop.com/peixun/rfe/110.html

ADS 学习培训课程套装

该套装是迄今国内最全面、最权威的 ADS 培训教程，共包含 10 门 ADS 学习培训课程。课程是由具有多年 ADS 使用经验的微波射频与通信系统设计领域资深专家讲解，并多结合设计实例，由浅入深、详细而又全面地讲解了 ADS 在微波射频电路设计、通信系统设计和电磁仿真设计方面的内容。能让您在最短的时间内学会使用 ADS，迅速提升个人技术能力，把 ADS 真正应用到实际研发工作中去，成为 ADS 设计专家...

课程网址： http://www.edatop.com/peixun/ads/13.html

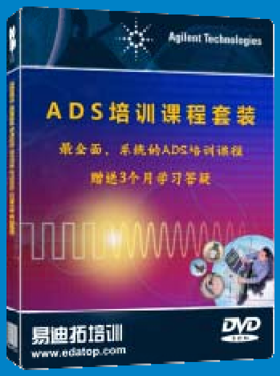

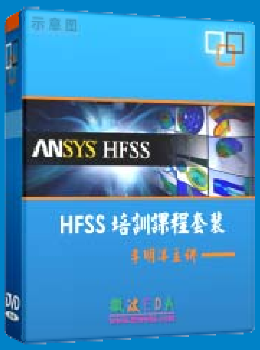

HFSS 学习培训课程套装

该套课程套装包含了本站全部 HFSS 培训课程，是迄今国内最全面、最专业的 HFSS 培训教程套装，可以帮助您从零开始，全面深入学习 HFSS 的各项功能和在多个方面的工程应用。购买套装，更可超值赠送 3 个月免费学习答疑，随时解答您学习过程中遇到的棘手问题，让您的 HFSS 学习更加轻松顺畅…

课程网址：http://www.edatop.com/peixun/hfss/11.html